IMPACT OF AS-SYNTHESIZED AND RADIATION-INDUCED DEFECTS IN TWO-DIMENSIONAL VERTICAL HETEROSTRUCTURES

A Dissertation
Presented to
The Academic Faculty

by

Christopher J. Perini

In Partial Fulfillment
of the Requirements for the Degree
Doctorate of Materials Science and Engineering in the
School of Materials Science and Engineering

Georgia Institute of Technology
May 2019

IMPACT OF AS-SYNTHESIZED AND RADIATION-INDUCED DEFECTS IN TWO-DIMENSIONAL VERTICAL HETEROSTRUCTURES

Approved by:

Dr. Eric M. Vogel, Advisor
School of Materials Science and Engineering
Georgia Institute of Technology

Dr. Faisal Alamgir
School of Materials Science and Engineering
Georgia Institute of Technology

Dr. Ilan Stern
School of [Whatever & Whatever Engineering]
Georgia Tech Research Institute

Dr. William Alan Doolittle
School of Electrical and Computer Engineering
Georgia Institute of Technology

Dr. Mark Losego
School of Materials Science and Engineering
Georgia Institute of Technology

Date Approved: March 20, 2019

To my wife and family

ACKNOWLEDGEMENTS

First and foremost, I would like to express my sincere appreciation to Dr. Eric Vogel for his guidance and advising during the last five years I have spent at Georgia Tech pursuing my education. I must also thank Dr. Brent Wagner for his instruction and guidance, both with respect to experimental procedures and equipment maintenance. I am also grateful to past and present members of the Vogel group. Specifically, I recognize Philip Campbell and Corey Joiner for their direction and training my first few years in the group. I am also thankful for the collaboration with Michael Muller, Pradip Basnet, Spyridon Pavlidis, Katie Young, Matthew West, and Cooper Voigt.

I also would like to thank the groups of Dr. Daniel Fleetwood and Dr. Sokrates Pantelides at Vanderbilt University for their collaboration in our radiation experiments. In particular, I am grateful to Pan Wang and Dr. Andrew O'Hara for their collaborative efforts. I also wish to thank En Xia Zhang, Huiqi Gong, Pengfei Wang, and Dr. Ronald D. Schrimpf for their contributions to our work.

Lastly, I must recognize my family, as none of this would be possible without their steadfast support. I would like to thank my parents for raising me with the drive and perspective that have allowed me to pursue my dreams. Additionally, I am eternally grateful to my wife Vanessa, who has provided countless hours of support and stood by my side throughout the challenges of my education.

TABLE OF CONTENTS

LIST OF TABLES

LIST OF FIGURES

LIST OF SYMBOLS AND ABBREVIATIONS

2D	Two dimensional
AFM	Atomic force microscopy
ALD	Atomic layer deposition
BEOL	Back-end-of-line
CMOS	Complementary Metal Oxide Semiconductor
CNP	Charge neutrality point
CVD	Chemical vapor deposition
DFT	Density functional theory
FET	Field effect transistor
FWHM	Full width at half maximum
FN	Fowler Nordheim
hBN	Hexagonal boron nitride
LED	Light emitting diode
MBE	Molecular beam epitaxy
MIGS	Metal induced gap states
MOSFET	Metal-oxide semiconductor field effect transistor
NDR	Negative differential resistance
PL	Photoluminescence
PMMA	Poly(methyl methacrylate)
SAM	Self-assembled monolayer
SBH	Schottky barrier height
SEE	Secondary electron edge

STEM	Scanning transmission electron microscopy
TE	Thermionic emission
TEM	Transmission electron microscopy
TFET	Tunneling field effect transistor
TMD	Transition metal dichalcogenide
UPS	Ultraviolet photoelectron spectroscopy
XPS	X-ray photoelectron spectroscopy

SUMMARY

In recent years, transition metal dichalcogenides (TMDs) have shown promise as a next generation class of semiconducting two-dimensional materials for use in electronic devices. Due to their low dimensionality, TMDs are appealing materials for a variety of applications, including flexible electronics, digital and analogue electronics, optoelectronic uses, and sensors. The absence of out-of-plane dangling bonds in 2D materials enables the potential for arbitrary stacks of 2D layers, yielding a 2D vertical heterostructure. The stacking arrangement of 2D layers in these heterostructures can be tailored to yield a number of different device characteristics, from steep slope tunnel transistors to resonant tunnel junctions. However, the majority of studies that explore TMDs for various applications obtain films using methods that are not scalable, such as mechanical exfoliation or synthesis at high temperatures ($T > 450\ ^{o}C$). In order for TMDs to be integrated into industrial back-end-of-line (BEOL) processes, films must be able to be synthesized using conditions that are compatible with complementary metal oxide semiconductor (CMOS) BEOL process limitations, namely low synthesis temperature.

To achieve compatibility with BEOL limitations, this work demonstrates low temperature synthesis of TMDs utilizing plasma-assisted synthesis techniques. Physical characterization yields information on the stoichiometry, crystallinity, thickness, and electronic structure of the films, while electrical measurements are used to correlate the electronic transport through the films to material quality and defect structure. In particular, the temperature dependence of in and out-of-plane conductivities provide information on

conduction mechanisms through the material, as well as injection at the metal/semiconductor interface.

TMD films are synthesized on different substrates in order to enable direct layer-by-layer construction of heterostructures, removing the need for transfer processes that introduce contamination at the interfaces between layers. MoS_2/high-k dielectric/MoS_2 and MoS_2/WS_2 heterostructures are constructed from low temperature synthesized films, and metal/MoS_2/metal heterostructures are constructed from both low and high temperature synthesized films; all of which are used to investigate tunneling and injection mechanisms, rectification, pinning effects, and switching behavior. Certain heterostructures are exposed to ionizing radiation to induce various defects into the different heterostructure layers, so that individual defect types can be correlated to changes in resulting device behavior. Hydrogen impurities and oxygen complexes at the 2D/oxide interface are found to dope and degrade device performance, and passivated oxygen vacancies in the high-k dielectric interlayer can contribute to trap-assisted tunneling across the tunnel junction.

The work presented in this thesis establishes a basis for low-temperature synthesis of TMDs and demonstrates methods for how restrictions on synthesis conditions can be overcome. An understanding of how defects and material quality influence resulting device performance was performed through a combination of physical characterization and device characteristics. In addition, the interaction between the TMD and metal contacts is explored in the context of Fermi level pinning. In summary, this work demonstrates low temperature synthesis of TMDs, providing a path for 2D heterostructure implementation into BEOL processes, and explores the implications of resulting material quality and defect structure on heterostructure device performance.

CHAPTER 1. INTRODUCTION

Due to their unique thickness-dependent properties, two-dimensional (2D) materials have recently generated interest for a variety of device applications, including flexible electronics[1-6], optoelectronics[7-14], and sensors[15-18]. One particularly attractive property of 2D materials is the absence of out-of-plane bonds; all atomic bonding occurs in plane, yielding a layered van der Waals structure as opposed to a 3D bulk crystal. Because interaction between layers is predominantly van der Waals, heterostructures of differing 2D layers can be fabricated without concerns of epitaxial lattice registry[19-20]. Therefore, 2D materials show promise for realizing device architectures and application that are difficult to achieve using bulk 3D crystals, such as memory select[21], steep-slope[22-24], or resonant tunneling structures[25-28]. This chapter includes an overview on the history of 2D materials, a background on the origin of useful properties 2D materials exhibit, a summary of various synthesis methods used to grow these materials, and a survey of various applications of 2D materials in electronics devices.

1.1 History of 2D Materials

Despite their recent attention for electronic device applications, the unique properties of 2D materials have been explored for over 50 years, most notably as solid lubricants[29]. 2D materials exhibit strong in-plane bonding, but because the out-of-plane interaction between layers is predominantly van der Waals, the out-of-plane strength of these materials

is weak, enabling individual layers to slip with respect to one another. Therefore, these materials lend themselves effectively to lubricant applications.

Although 2D materials were historically used for their physical and mechanical properties, a significant amount of work explored their electronic structure and properties[30-33]. The single layer allotrope of graphite, termed graphene in 1986[34], was first postulated to exist in 1947 by P. R. Wallace[35]. However, it was not until 2004 that single layer graphene was experimentally realized using the "Scotch tape method" of mechanical exfoliation[36], winning K. S. Novoselov and A. K. Geim the Nobel prize in 2010. Novoselov and Geim's realization of a single layer 2D crystal spurred a renewed interest in 2D materials, leading to similar demonstrations of exfoliated single layers of semiconducting TMDs and insulating dielectrics like hexagonal boron nitride (hBN). The Scotch tape method represented a relatively easy method to produce single layered 2D materials, allowing anyone with access to bulk 2D crystals to perform 2D material experiments. However, a significant limitation of the Scotch tape method is that the resulting 2D flakes on the order of micrometers, preventing this method from being used as a scalable process. Despite this limitation, the increased access of single layer 2D crystals enabled a rapid step forward in 2D material research. These advances have come in various forms, ranging from heterostructures exhibiting negative differential resistance (NDR)[26, 37] to FETs with an 8 order of magnitude ON/OFF ratio[38].

1.2 Structure and Properties of 2D materials

1.2.1 Structure and Properties of TMDs

TMDs have the characteristic chemical formula MX_2, where M is a transition metal (typically Mo or W) and X is a chalcogen (S, Se, Te, etc.). In a single layer, the atomic arrangement of the TMD consists of a single sheet of transition metal sandwiched between two sheets of chalcogen atoms. Additional layers interact through van der Waals interaction, yielding a bulk crystal. Although the bulk crystal consists of multiple TMD layers, each individual layer consists of only in-plane bonding, meaning that there are no out-of-plane dangling bonds at the interface between two layers. Therefore, assuming perfect quality TMD films, perfect interfaces can be achieved; this is in contrast to analogous 3D crystal interfaces, where the interface between two different materials typically involves dangling bonds that prevent a perfect interface. Additionally, because the atomic bonding in TMDs is primarily in-plane, TMDs exhibit anisotropic electronic transport properties. More specifically, the in-plane conductivity is relatively high, whereas out-of-plane conductivity is low and requires tunneling for carrier to jump from layer to layer[39].

When layers are added onto the monolayer TMD, a few different stacking configurations are possible, which influence resulting film properties. The stacking arrangement depends on the coordination of the metal and chalcogen atoms across multiple layers of the TMD[8]. For most of the common TMDs (namely the transition metal sulfides and selenides), the thermodynamically stable configuration at room temperature is the 2H phase, a characteristic AB stacking arrangement where the metal atoms in one layer align

with the chalcogen atoms in the opposite layer, and the chalcogen atoms in a single layer align with each other on either side of the transition metal atoms, yielding hexagonal symmetry[40].

Another stacking configuration for TMDs is termed the 1T configuration. In this case, the atomic arrangement involves the metal and chalcogen atoms in one layer aligning with the metal and chalcogen atoms in the opposite layer, respectively[40]. This configuration yields an orthorhombic unit cell, as opposed to the trigonal prismatic cell exhibited by the 2H phase. A parallel case is the 1T' phase, where the metal atoms between layer align, but the 2 layers are rotated 180°. Although many common TMDs favorably exhibit the 2H phase at room temperature, there are cases, such as WTe_2, that favor the 1T' phase[41]. Although different TMDs thermodynamically prefer to arrange in a particular stacking arrangement, changes to the film's environment (such as temperature or pressure) can be used to induce a shift from one stacking phase to the other[42]. This shift has also been predicted to be possible to induce electrically[43].

The electronic properties of a TMD film depends on the phase of the multi-layer film. In the 2H phase, the p_z orbitals of the chalcogen atoms in opposite layers are interspersed from each other, resulting in no orbital overlap. Conversely, in the 1T phase, the chalcogen p_z orbitals of the different layers directly overlap. These p_z orbitals strongly influence the valence structure of the material, and as such the different phases exhibit contrasting electronic properties. For example, MoS_2 and WSe_2 are semiconducting in the 2H phase, but shift to semi-metallic behavior in the 1T phase[44-45].

Because the layer-layer interaction strongly influences the electrical characteristics of TMDs, TMD films exhibit interesting thickness dependent properties. In the case of MoS_2, the valence structure of the material arises due to sulfur atom p_z orbitals and the molybdenum atom *d* orbitals[8]. Because the sheets of sulfur atoms sandwich the molybdenum sheet, any environmental influence is strongly felt by the out-of-plane p_z sulfur atom orbitals. As such, any interlayer interactions are strongly felt by the sulfur atom's p_z orbitals, and significantly affect the valence band structure of the material. Conversely, the molybdenum atom's *d* orbitals influence the conduction band structure of the material. Because these molybdenum atoms are shielded from the environment by the surrounding sulfur atoms, the conduction band structure is more resilient to environmental or layer dependent interactions[8].

Continuing with the example of MoS_2, a monolayer is semiconducting with a direct bandgap of approximately 1.9 eV[46]. When a single layer is added to a monolayer, the band structure is altered. Specifically, the bandgap decreases, and transitions from a direct gap at the K-point to an indirect gap with the valence band maximum at Γ-point[8, 47]. This change occurs with the addition of only a single layer; this implies that for most optoelectronic applications, monolayer MoS_2 is required in order to exploit the direct bandgap of the material. As more layers are added, the bandgap continues to decrease to a value of 1.2 eV at around 8 layers; above 8 layers, the film can be considered "bulk". Although the conduction band structure is modified with the addition of layers, it changes to a much lesser extent, where the conduction band minimum shifts from the K-point at the monolayer to a point between the K and Γ-points in bulk. The transition in MoS_2's electronic band structure with respect to film thickness is plotted in Figure 1.1[46]. Other

TMDs also exhibit similar behavior, where monolayer films typically exhibit direct bandgaps that transition to indirect gaps as layers are added[8].

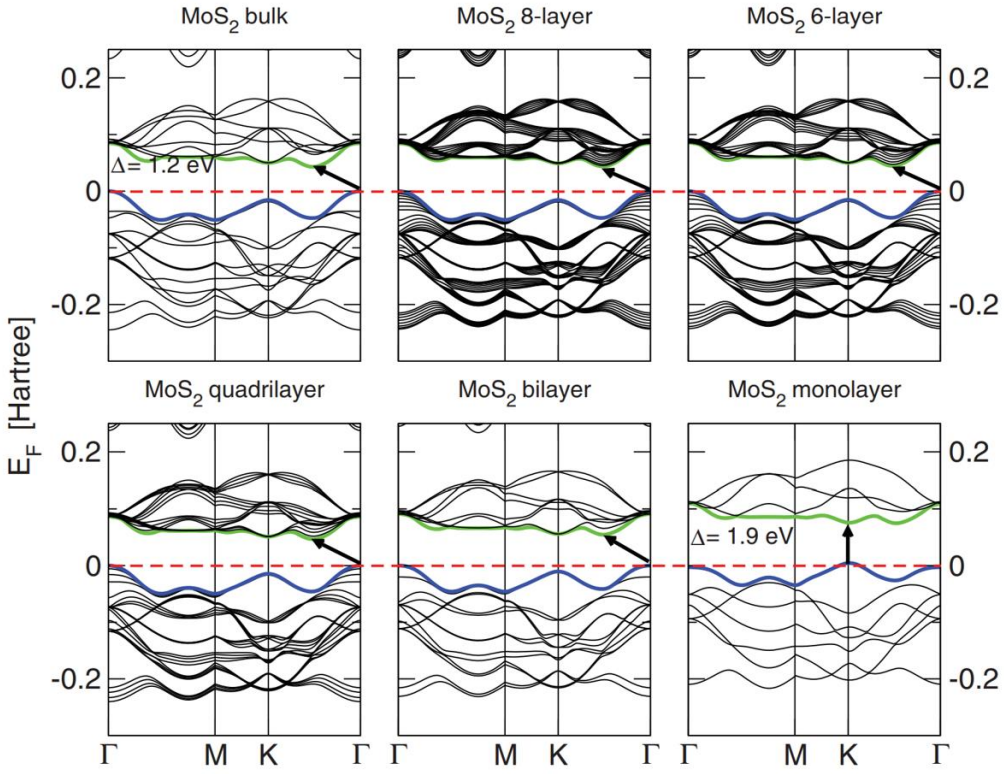

Figure 1.1. The relationship between MoS_2 band structure and film thickness, showing the transition from a 1.2 eV indirect bandgap in bulk MoS_2 to a 1.9 eV direct bandgap for monolayer MoS_2. Reprinted with permission from A. Kuc, A.; Zibouche, N.; Heine, T., Influence of quantum confinement on the electronic structure of the transition metal sulfide TS2. *Phys. Rev. B* 2011, *83* (24). Copyright 2011 by the American Physical Society[46].

This thickness dependence of TMDs on the band structure is commonly observed in photoluminescence (PL) measurements. Mono to few-layer TMDs exhibit a PL response, with monolayer samples exhibiting the strongest signal[48-49]. Because the optical bandgap increases with increasing film thickness in conjunction with the electrical bandgap decreasing, the PL signal intensity drops off relatively quickly with each additional TMD

layer. Additionally, the PL peak position shifts in energy as more layers are added to the film, as the optical bandgap changes in value.

1.2.2 Structure and Properties of Graphene

In contrast to TMDs, graphene only requires a single element, carbon, to form a two-dimensional sheet of material. In a single sheet of graphene, carbon atoms are arranged in a honeycomb lattice with a lattice constant of 2.46 [50]. In the monolayer, graphene exhibits a unique band structure where the conduction band and valence band meet at the K-point in momentum space, resulting in a semimetal electronic structure[51]. Close to the K-point, the E-K dispersion relation is linear, yielding conduction and valence band cones. These cones are termed Dirac cones, and the single energy where they meet at the K-point is termed the Dirac point.

When a second layer is added, the modification of the band structure depends on the stacking arrangement. One common stacking configuration is ABA, termed Bernal stacking, which is the stacking found in geological graphite crystals. Conversely, multi-layer graphene can also stack in an ABC manner, yielding a rhombohedral structure. The stacking configuration influences the band structure at the K-point, where additional layers add concentric Dirac cones that either converge on the Dirac point or broaden to form parabolic conduction and valence band edges[52]. Therefore, by adding additional layers and controlling the stacking configuration, it is possible to open a small bandgap into graphene.

Due to its linear dispersion relation, carriers in graphene are Fermions and obey Fermi-Dirac statistics[53]. From this unique band structure, electrons in graphene theoretically have an effective mass of 0, implying superconductivity, with thermal

velocities of 10^6 m/s [54]. Because of this low electron mass near the K-point, monolayer graphene offers high electronic performance characteristics, including mobilities as high as 200,000 cm^2/Vs when suspended[55]. The mobilities of monolayer graphene are significantly reduced when in contact with any substrate or encapsulating medium, having best case values of near 10,000 cm^2/Vs on SiO_2 [53]. In both of these cases, the graphene was obtained through mechanical exfoliation of geological crystals; the mobility values are further reduced when synthesized graphene crystals are used[56].

1.3 Synthesis Techniques for 2D materials

Although mechanical exfoliation of bulk 2D crystals produces high quality 2D flakes, the resulting films are typically on the order of microns. Additionally, controlling the thickness of the exfoliated flakes is difficult. Moreover, mechanical exfoliation is not suitable for large scale industrial processes. Therefore, synthesis techniques must be developed in order to obtain high quality, large area, thickness controlled 2D films.

1.3.1 Synthesis of TMDs

A common synthesis technique for TMDs is chemical vapor deposition (CVD)[57-60]. In a CVD synthesis process, different precursors containing the transition metal and chalcogen are concurrently delivered to a substrate in a high temperature environment. These precursors react in the vapor phase and subsequently deposits onto the substrate to nucleate an individual TMD grain. Additional reacted precursor either attaches to the edge of the existing grain to facilitate grain growth, or nucleates a new grain. Common

chalcogen precursors typically include elemental powders[58, 61] and hydrogen chalcogenides[59-60]. The transition metal is commonly delivered using one of a few different sources including transition metal oxides[60, 62], metal hexacarbonyls[63-64], or transition metal chlorides[65]. By tuning synthesis parameters including temperature, precursor flow rates, pressure, and synthesis time, film characteristics such as thickness, uniformity, and grain size can be controlled. However, a drawback of the CVD technique is that the extended synthesis durations required to coalesce a complete film typically result in additional layers nucleating on top of existing grains. These additional nucleation events result in nonuniform film thicknesses, inducing significant electronic inhomogeneity across the film due to TMDs strong thickness dependence on electronic properties. However, the fact that additional layers can nucleate atop existing grains has allowed for direct synthesis of both vertical and lateral heterostructures[61, 66-67].

One way to circumvent the inhomogeneity issues CVD presents is the thin film reaction synthesis technique[68]. In this method, a thin layer of transition metal is pre-deposited onto the synthesis substrate, typically on the order of a single nanometer. The thin metallic film is then exposed to a high temperature chalcogen rich environment, driving the chalcogen to react with the transition metal film. A benefit of the thin film reaction technique is that the thickness and uniformity of the resulting TMD film predominantly depends on thickness and uniformity of the initial transition metal layer. Therefore, large area, uniform TMD films can be synthesized by controlling the uniformity of the initial layer[68]. However, a limitation of this technique is that the resulting grain size of the TMD films are typically on the order of 10 nm [69]. Additionally, the synthesis process is diffusion limited, implying there are limitations on the film thicknesses that can be

synthesized. When the initial transition metal films are relatively thick (on the order of a few nanometers), the resulting TMD will grow out-of-plane in a vertical lamellar structure as opposed to planar layers stacked on top of one another[70-71]. That said, heterostructure synthesis has been demonstrated using the thin film reaction method; by pre-depositing different transition metals, an abrupt heterojunction can be directly synthesized[72-73].

A third synthesis technique for TMDs is molecular beam epitaxy (MBE) of transition metal and chalcogen precursors[74-79]. The ultra-high vacuum environment of an MBE system also enables synthesis of TMDs that cannot be synthesized in traditional furnaces due to thermodynamic effects, such as transition metal tellurides[78-79]. While MBE synthesis commonly utilizes a hexagonal substrate such as graphite or hBN to provide epitaxy for the TMD's nucleation, MBE synthesis directly on SiO_2 wafers has been demonstrated[75]. The precursors are typically delivered at low fluxes, where the chalcogen is usually thermally evaporated and the transition metal is e-beam evaporated. In particular, a chalcogen-rich environment is necessary in order to suppress nucleation and facilitate grain growth. Figure 1.2 shows atomic force microscopy (AFM) images of WSe_2 flakes synthesized on highly oriented pyrolytic graphite (HOPG) using different selenium fluxes[77]. A notable benefit of MBE synthesis is that a variety of heterostructures can be synthesized directly in a single system without breaking vacuum, enabling heterostructure fabrication with pristine interfaces. However, the common limitations of MBE systems cannot be ignored, where high cost and vacuum requirements make scalable production difficult.

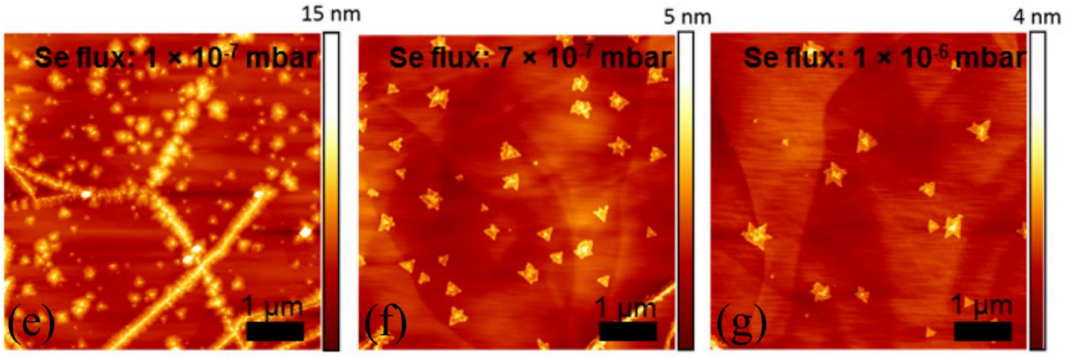

Figure 1.2. AFM images showing the impact of Se flux on the synthesis of WSe_2 on HOPG. High Se flux results in suppressed nucleation and more uniform flakes. Reprinted with permission from R. Yue et al., *2D Materials*, vol. 4, p. 05419-7. Copyright 2017 by IOP Publishing Ltd[77].

For all of these synthesis methods, a common requirement is the relatively high required synthesis temperature. Although these different techniques have different specific temperature requirements, all methods require temperatures greater than 400 ^{o}C, making them incompatible with BEOL fabrication processes. Attempts to decrease the synthesis temperature have begun yielding encouraging results, but still require significant optimization. Atomic layer deposition (ALD) techniques have successfully synthesized MoS_2 at temperatures as low as 150 ^{o}C, although film quality has been poor and not suitable for electronic applications[80-81]. An alternative approach to decreasing synthesis temperature has been through plasma-assisted synthesis techniques[82]. By exposing a molybdenum thin film to an H_2S plasma, MoS_2 was successfully synthesized at temperatures of 150 and 300 ^{o}C. Because the plasma cracks the H_2S gas into H-S and S radicals, the activation energy for the sulfur-molybdenum reaction is significantly reduced. Although grain size and electron mobilities were both inferior to similar CVD synthesized

MoS_2 films, plasma assisted synthesis appears to be a promising avenue for integrating TMD synthesis into scalable BEOL processes.

1.3.2 Synthesis of Graphene

The synthesis of graphene has been studied at length for over 10 years. Techniques such as CVD on metallic foils[56, 83], epitaxial growth from SiC[84], and reducing graphene oxide[85] all have unique benefits and drawbacks. Of these three techniques, epitaxial synthesis from SiC substrates yields the highest quality graphene, but is also the most expensive technique and not viable at an industrial scale. Conversely, reducing graphene oxide is inexpensive and can be done at a relatively high throughput, but yields low quality films that are not suitable for high performance electronic applications. CVD synthesis on metallic foils offers a compromise of cost and quality, where relatively high-quality material can be synthesized at industrial scales.

The most common substrate used to synthesize graphene via CVD is copper foil, due to its catalytic nature. A carbon source, typically methane, is delivered to a high temperature (~1,000 ^{o}C) environment, where the copper then catalytically cracks the precursor[86-87]. The resulting carbon adsorbs to and diffuses across the copper surface to high energy sites, such as copper grain boundaries and defects[88]. Any remaining hydrogen desorbs from the carbon, and when sufficient carbon agglomerates at the site, it nucleates into a graphene island. Additional carbon precursor either diffuses to the edge of the existing grain to facilitate grain growth, or nucleates a new grain at a different high energy site on the copper foil[89]. Given sufficient time and precursor, the individual graphene islands coalesce into a single graphene film; this film typically is polycrystalline, as the

individual nucleated grains do not align with one another[90]. Because the carbon precursor is catalytically cracked by the exposed copper surface, once a monolayer of graphene coalesces, nucleation and growth are suppressed. Therefore, graphene CVD synthesis on copper is a self-limiting process and results in a predominantly monolayer graphene film on the copper surface.

The grain size of the graphene films can be controlled by changing the purity and grain structure of the underlying copper substrate, as well as the synthesis temperature and pressure[56, 91]. At higher synthesis temperatures, the resulting grain size significantly increases, whereas nucleation density decreases with increasing temperature. As such, higher synthesis temperatures result in graphene films with fewer, larger grains. Similar trends are observed for synthesis pressure, where the carbon partial pressure affects nucleation by influencing carbon adsorption, dehydrogenization, diffusion, and formation rates[91].

1.4 Defects in 2D Materials

Understanding the type and density of defects within a two-dimensional material is important in determining its electronic properties and characteristics. In two-dimensional materials, the dimensionality of different defects is one fewer than in traditional bulk materials. For example, a grain boundary in a three-dimensional crystal would be considered a two-dimensional defect, whereas in a two-dimensional material a grain boundary can be thought of as a line defect having one dimension. The two common types of defects that influence physical and electronic structure in two-dimensional materials are

point defects consisting of vacancies or charged impurities and grain boundaries resulting from grains impinging during growth. These different defects influence electronic structure and performance of the film in a number of ways, for example by introducing new energy states that act as traps for carriers or scattering carriers and lowering the mobility of the material.

Density functional theory (DFT) calculations on monolayer MoS_2 were performed to explore the thermodynamic energies of formation for different point defects[92]. One of the most common defects in MoS_2 are interstitial sulfur adatoms, which create a shallow gap state near the valence band edge. This near-valence state narrows the bandgap, effectively reducing the bandgap by 0.23 eV. A common complementary defect in MoS_2 is the sulfur vacancy. Sulfur vacancies, present in nearly all MoS_2 films obtained either from exfoliation or synthesis, introduce two different states into the bandgap. The first state is a shallow valence state, similar to the case of sulfur adatoms. The second state appears as a deep level trap state located in the middle of the bandgap, due to dangling bonds associated with the Mo *4d* orbitals[92].

In order to confirm the thermodynamic stability of these defects, atomic resolution scanning transmission electron microscopy (STEM) has been used to characterize intrinsic defects in synthesized MoS_2 [93]. The most commonly observed defect was the sulfur vacancy, consistent with the theoretical prediction of sulfur vacancies having one of the lowest defect formation energies. In addition, defect complexes including sulfur and molybdenum di- and tri-vacancies were observed, along with substitutional defects where molybdenum occupies a sulfur site, and vice versa; however, few molybdenum mono-vacancies were observed. This can be explained due to the formation energies of the

different vacancy states: because sulfur vacancies have the lowest energy of formation, defective areas in MoS_2 prefer to be molybdenum terminated. As such, should a molybdenum vacancy occur, the surrounding sulfur preferentially breaks their respective bonds and desorbs from the film. From these desorption events, molybdenum and sulfur adatoms were also observed on the MoS_2 surface.

Because MoS_2 defects preferentially terminate with sulfur vacancies, grain boundaries also tend to be molybdenum terminated; this phenomenon is also observed in other common TMDs [94-95]. In fact, the gap states generated from sulfur vacancies, along with the electrons donated by nearby dangling bonds, have been reported to induce semi-metallic behavior in the grain boundaries of TMDs[95-96]. In the case of films with small grain size, the consequences of this effect are rather significant. Although the semi-metal behavior of TMD grain boundaries is detrimental in semiconducting applications, this phenomenon has been exploited for different catalytic applications, such as hydrogen evolution[97]. For electronic applications, however, large grains are desirable.

The atomic resolution STEM imaging used to monitor defects also yields information on dislocations in MoS_2. From the top down, pristine MoS_2 is viewed as six-member rings of sulfur atoms surrounding a molybdenum atom. Dislocations commonly initiate with a 5/7-member ring pair, although 4/4, 4/6, 4/8, and 6/8 member rings were also observed[93].

These 5/7-member ring pairs commonly are present in graphene films as well, manifesting as a dislocation that yields a grain boundary. Grain boundaries also arise due to synthesis conditions that influence nucleation and grain growth, and act as scattering

sites for carriers within the plane of the film[98-99]. As is the case for TMDs, graphene films with large grain sizes are of substantial interest for electronic applications, and significant work has been done to optimize synthesis to yield large grain films[100-101].

Various vacancy clusters in graphene have also been observed, where complex ring combinations such as the 5/9 monovacancy, the 5/8/5 divacancy, and the 5555/6/7777 divacancy[102]. Although some of these complex point defects exist naturally in exfoliated and synthetic films, they commonly arise under exposure to high energy electron exposure. The radiation effects of 2D materials will be discussed in more detail later.

While transmission electron microscopy (TEM) and STEM techniques offer valuable information of the defect structure and concentration in 2D films, both techniques are time and cost intensive. In contrast, Raman spectroscopy has proven to be a valuable tool for characterizing the quality of both TMD and graphene films due to its low cost and high throughput. In TMDs, the full width at half maximum (FWHM) of the A_{1g} and E^1_{2g} peaks yields qualitative information on grain size and defect density[68, 103]. Figure 1.3 (a) shows Raman spectra for MoS_2 synthesized at different temperatures, with the corresponding FWHMs of both the A_{1g} and E^1_{2g} peaks shown in (b)[68]. Films synthesized at higher temperatures exhibit sharper Raman peaks, indicating higher quality films; the peak FHWMs for the 1,050 ^oC synthesized film are nearly identical to values found in geological bulk crystals. Although the information obtained is qualitative, benchmarking can be done to obtain a general understanding of the quality of the TMD.

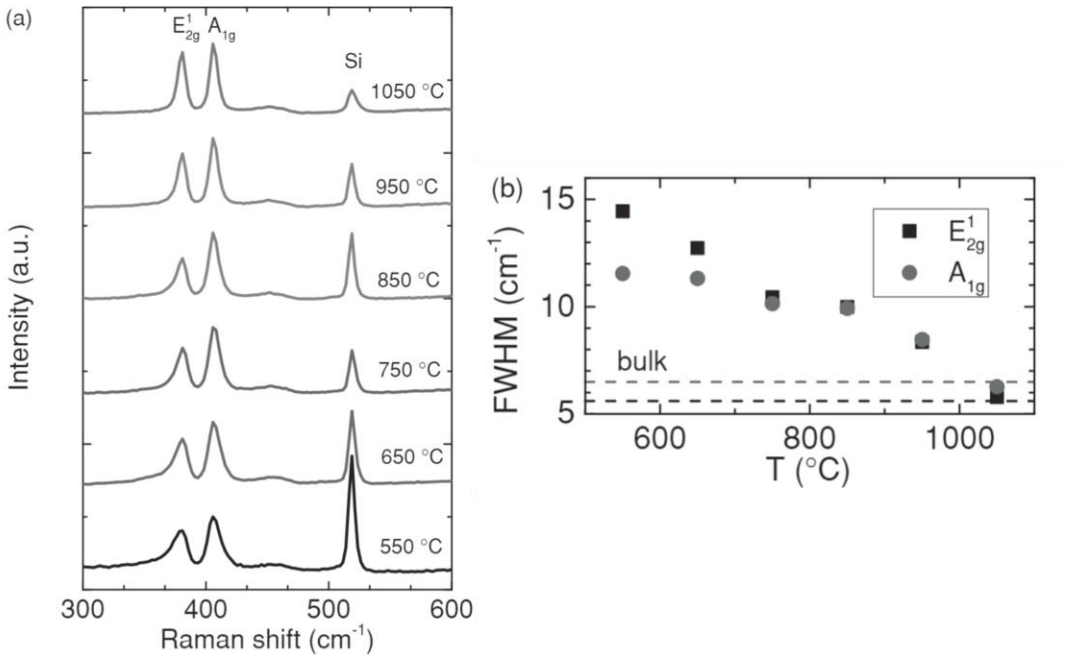

Figure 1.3 (a) Raman spectra for MoS2 synthesized at various temperatures. (b) FWHM values for the A1g and E12g peaks for each synthesis temperature. Reprinted with permission from Tarasov, A.; Campbell, P. M.; Tsai, M.-Y.; Hesabi, Z. R.; Feirer, J.; Graham, S.; Ready, W. J.; Vogel, E. M., Highly Uniform Trilayer Molybdenum Disulfide for Wafer-Scale Device Fabrication. *Adv. Funct. Mater.* 2014, *24* (40), 6389-6400. Copyright 2014 by John Wiley & Sons[68].

For graphene, Raman spectroscopy provides a more quantitative understanding of defect density. Characteristics including doping, number of layers, and strain can also be determined using Raman spectroscopy by investigating peak positions, relative peak intensities, and peak FWHMs[104-106]. A particular peak termed the D peak, located at approximately 1,360 cm^{-1}, can be used to determine defect density. The D peak corresponds to a symmetric phonon node that normally destructively interferes with itself in a pristine film; when a defect is present, the symmetry is broken, and the resulting asymmetric phonon node gives off a measurable signal[107]. Therefore, the D peak can be used to monitor whether defects are present in the graphene film. Additionally, the relative

intensity of the D peak can be used to extract the density of defects in the film, which has been shown to be correlated to a decrease in carrier mobility[107].

1.5 Electronic Applications of 2D Heterostructures

As stated earlier, the significant interest in 2D materials arises from their unique properties that can be exploited for a variety of applications. These properties, which include a lack of out-of-plane dangling bonds, a step-like density of states, and inherent flexibility, lend themselves well to applications such as flexible electronics, sensors, optoelectronics, and most recently memory select devices. Although the majority of the content in this thesis revolves around 2D heterostructure device architectures, this section will also include a brief review of other common 2D material electronic applications.

1.5.1 Flexible Electronics

As their name suggests, 2D materials are atomically thin, where atomic bonding is limited within the x-y plane. The absence of a third dimension uniquely suits 2D materials for flexible applications. Current flexible technologies revolve around either thinning bulk 3D crystals or utilizing polymeric organic electronic materials. In the case of thinning bulk 3D crystals, the electronic structure of the material commonly changes when the material is thinned[108-110]. Therefore, the resulting thinned 3D materials must be engineered to yield the desired physical and electronic structure. Organic transistor materials also come with their associated challenges. Although these materials are inherently some of the most flexible electronic materials, they commonly exhibit poor mobilities on the order of 0.01

cm^2/Vs [111]. The low mobilities exhibited in these materials significantly reduce the applicability of these materials to lower performance and low frequency applications.

In contrast to bulk 3D crystals and organic materials, 2D materials are inherently atomically thin and offer characteristic flexibility while maintaining electronic properties closer to current electronic technology. Similar to how 2D materials exhibit van der Waals interaction to other 2D layers, they also demonstrate a van der Waals interaction with the substrate they reside on. Therefore, 2D materials can be transferred onto arbitrary flexible substrates for flexible electronic applications[2-3, 5, 72]. Transferred properly, the films do not exhibit any physical changes or degradation after the transfer process, and the mobilities of the films transferred onto flexible substrates are nearly identical to the mobilities calculated prior to the transfer process[112]. Additionally, the films did not exhibit any decrease in performance after a large number of cycles, highlighting that their flexibility is robust[15, 112]. These results indicate that 2D materials are well suited for flexible, high performance applications.

1.5.2 Sensors

The principle of operation in sensing applications revolves around the properties of a material changing with its surrounding environment. Because 2D materials are atomically thin, they are extremely sensitive to changes in their surroundings. This effect can be observed in simple cases of threshold voltage shifts in atmospheric transistor measurements[113-115]. One such example involves MoS_2 gas sensors, which exhibit good sensitivity and fast recovery times[116]. Additionally, MoS_2 has been used to demonstrate selective gas sensing[117]. Similarly, TMDs can be doped simply by adsorbing charged

molecules to the surface[118]. These charged molecules donate or accept electrons, changing the electronic structure of the material and inducing a threshold voltage shift. By tailoring the interface between a 2D material and its ambient environment, chemical sensitivity can be achieved in the case of both graphene and TMDs.

In addition to chemical sensing, the strain response of TMDs can be exploited for strain sensing applications. Specifically, the electronic structure of TMDs changes with strain, which can induce changes in device characteristics[119-121]. These changes in device characteristics can be correlated to the strain on the material, yielding a strain sensing device[15, 122]. Similar behavior is also observed in graphene devices, where fluctuations in resistivity can be correlated to changes in applied strain[123-124]. Because 2D materials are inherently flexible, they demonstrate minimal degradation under many cycles of strain, indicating they are appropriate for strain sensing applications.

1.5.3 Optoelectronics

While graphene is semi-metallic and does not exhibit a bandgap, the optoelectronic structure of TMDs are well suited for optoelectronic applications. As monolayers, TMDs have a direct bandgap with energies in the visible portion of the electromagnetic spectrum[125-126]. This direct bandgap makes TMDs attractive as materials for solar cells, light emitting diodes (LEDs), and photodetectors.

Both graphene and TMDs have recently shown encouraging results as solar cell materials[127-129]. The quantum efficiency of these structures varies from ~1% to over 50%, depending on the device architecture and incoming wavelength used. However, a limitation of 2D materials in this application space is that the atomically thin nature of these materials

limits light absorption efficiency. To mitigate this effect, various techniques have been employed to improve absorption and improve device efficiency[130-132].

Numerous studies have exploited the direct bandgap of monolayer TMDs to fabricated LED devices[133-134]. Because monolayer TMDs are inherently flexible, they offer promise for atomically thin, flexible LED devices. Additionally, more complex heterostructures have demonstrated LED behavior via quantum well tunneling[135-136]. However, the efficiency in these cases is rather low, where best-case values are around 0.2% [137].

Heterojunctions of TMDs have been demonstrated to exhibit the photovoltaic effect[66-67, 138]. When exposed to light, excitons are generated in the TMD layers, which then dissociate into electrons and holes and migrate to the layer with the lowest respective energy. This induces a change in carrier concentration, which can be observed in the device characteristics as a photo-rectifier. Similar graphene-based heterostructures have been shown to also exhibit photodetection behavior[9, 139]. Single layer photoresponse has also been demonstrated in TMDs[140]. In this case, a photocurrent can be measured across a single layer FET that is sensitive to incoming light intensity.

1.5.4 2D Heterostructure Operational Modes

Although a number of studies have demonstrated standard channel FET operation of 2D materials, device architectures based on heterostructures utilize the unique properties of 2D materials more effectively. Because there exist two dimensional conductors (graphene), semiconductors (TMDs), and insulators (hBN), any combination of stacked

layers can be realized, due to the lack of out-of-plane bonding characteristic of 2D materials.

A common vertical heterostructure stack used for electronic devices consists of two electrodes separated by an insulating layer. The electrodes are commonly graphene or TMDs, while the insulating layer can be hBN, a non-2D high-κ dielectric, or even the van der Waals gap. This structure typically operates via tunneling, where under certain bias conditions, carriers are driven across the interlayer from one electrode to the opposite electrode. For tunneling to occur, there must be alignment of the bands in the two electrode layers, which is commonly done through a combination of drain-source (V_{ds}) and gate (V_g) biases.

The construction of this tunneling FET (TFET) architecture is typically designed to facilitate one of two types of tunneling: opposite band-to-band tunneling, where carriers tunneling from the conduction (valence) band of one electrode to the valence (conduction) band of the other electrode; and like-band tunneling, where carriers from the conduction (valence) band of one electrode tunnel to the conduction (valence) band of the other electrode. These two tunneling regimes are shown schematically in Figure 1.4 (a,b) for band-to-band and like-band injection, respectively[141].

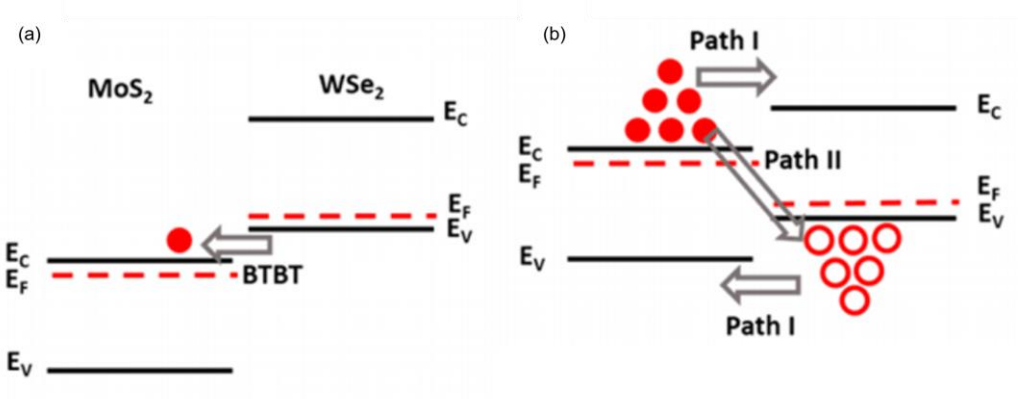

Figure 1.4. Band diagram of a MoS_2/WSe_2 operating in the (a) band-to-band and (b) like-band tunneling regimes. In (b), path I corresponds to the like-band injection.. Reprinted with permission from Roy, T.; Tosun, M.; Cao, X.; Fang, H.; Lien, D.-H.; Zhao, P.; Chen, Y.-Z.; Chueh, Y.-L.; Guo, J.; Javey, A., Dual-Gated MoS2/WSe2 van der Waals Tunnel Diodes and Transistors. *ACS Nano* 2015, *9* (2), 2071-2079. Copyright 2015 by the American Chemical Society[141].

1.5.4.1 Opposite-Band Injection

In an opposite-band tunneling architecture, two types of device behavior are commonly observed: steep-slope operation and Esaki diode operation. Because 2D materials have a step-like density of states, the band edges are perfectly square in the case of pristine materials. This unique property of 2D materials enables 2D heterostructures to potentially surpass the 60 mV/decade limit in traditional metal-oxide semiconductor FETs (MOSFETs).

The steep-slope mode of operation requires a set of materials with a small offset between the conduction band in one electrode and the valence band in the opposite electrode. At small biases, the offset prevents tunneling carriers from crossing the interlayer, because no overlap between the conduction and valence bands exists. As the

bias across the structure increases, the conduction band edge in one electrode aligns with the valence band edge in the opposite electrode, whereupon a sharp increase in tunnel current occurs. Further increases in applied bias further increase the overlap between the conduction and valence bands, although no increase in current is observed due to the momentum conservation requirement for tunneling. With pristine TMDs, the band edges are step like, which theoretically yield an infinite subthreshold swing. However, defects or grain boundaries broaden the band edges, resulting in a finite subthreshold swing[142].

Although various theoretical studies have explored and demonstrated the viability of steep slope device operation using TMDs, no experimental evidence of steep slope behavior has yet been realized. However, steep slope behavior has been realized through a combination of 2D MoS_2 and 3D p-type germanium[23]. Below the threshold voltage of the device, the Fermi energy of the germanium and conduction band of the MoS_2 are misaligned, preventing sufficient injection into the MoS_2 resulting in low current. Above the threshold voltage, the MoS_2 conduction band edges decrease in energy and lie below the germanium's Fermi energy, enabling tunneling across the van der Waals gap. The device resulted in a subthreshold swing below 60 mV/decade over four orders of magnitude, with an average value of 31 mV/decade.

The second characteristic behavior of opposite-band tunneling is the Esaki diode, first demonstrated in 1974 [143]. Similar to steep-slope operation, Esaki behavior requires an offset in the band alignment of the two 2D layers, although in this case there must be a small overlap between the conduction band of one layer with the valence band of the opposite layer at no applied bias. As the bias across the structure increases, the Fermi energies in the two layers offset, enabling tunneling from the conduction band of one layer

to the valence band of the opposite layer. With increasing bias, the tunneling window decreases, resulting in a decrease in tunnel current. This results in an NDR peak in the current-voltage characteristics. After the NDR region, further increases in bias result in increased current across the device. This Esaki behavior has been realized experimentally using both exfoliated TMDs[141, 144] and black phosphorous flakes[145].

1.5.4.2 Like-Band Injection

In the case of like-band tunneling, carriers tunnel from the conduction (valence) band of one electrode to the conduction (valence) band of the opposite electrode. Heterostructures fabricated for like-band tunneling commonly use identical layers for both electrodes, although like-band tunneling can be achieved using an asymmetric structure. When high quality materials are used with limiting scattering, tunnel current across the structure is dictated by momentum conservation. By applying a bias across the structure, the bands of each electrode align in both energy and momentum space, yielding a large increase in tunnel current that arises due to the momentum conservative tunneling that is enabled. Further increasing the bias misaligns the bands, eliminating momentum conservative tunnel pathways, reducing the current and resulting in a NDR peak[146]. It is important to note that the NDR observed in a like-band tunneling structure is solely due to momentum conservative tunneling, as opposed to the Esaki NDR behavior that arises due to a density of states effect.

NDR behavior has been demonstrated numerous times, commonly using graphene electrodes with hBN interlayers[26-27, 147]. In these studies, exfoliated flakes of graphene and hBN were assembled into a heterostructure on a thick hBN substrate in order to mitigate

any influence of the underlying SiO_2. NDR peak-to-valley ratios of up to 4 were observed at room temperature, although the authors note significant variation device to device. Similar experiments using CVD synthesized graphene did not exhibit NDR, indicating that material, interface, and substrate quality strongly impact device behavior[148].

Theoretical calculations have indicated that TMDs are better suited for symmetric TFET structures that exhibit NDR[25]. Specifically, the peak-to-valley ratios are predicted to be larger while also exhibiting sharper peaks with smaller FWHMs when compared to similar graphene-based TFETs. However, despite this prediction, the experimental realization of momentum conservative NDR has not yet reached the predicted performance. Although room temperature NDR has been demonstrated, the peak-to-valley ratios and peak FWHMs are comparable to similar graphene-based structures[149]. The discrepancy between calculation and experimentation further emphasizes that material quality and interfacial cleanliness plays an extremely important role in resulting device performance.

Heterostructures predicated on like-band carrier injection can also be designed to operate without tunneling restraints. The inherent band offset in asymmetric TMD heterostructures (for example MoS_2/WSe_2) has been exploited to demonstrate rectifying behavior[66, 72-73]. An important consideration in designing these heterostructures is whether lateral transport through the TMD layer is desired. When the heterostructure is contacted such that the metal contacts are laterally offset from the active area of the device (where the TMDs overlap), the device performance is influenced (and potentially limited) by the in-plane conductivity of the TMD film, resulting in poor rectification behavior[73].

Conversely, devices that are purely vertical exhibit stronger rectification and are not as limited by TMD quality and in-plane resistivities[72].

1.5.5 Metal-TMD-Metal Heterostructures

Recently, interest in metal/TMD/metal heterostructures has arisen due to the structure's promise for memory select devices[21]. A rendering of the device architecture is shown in Figure 1.5 (a). This structure is inherently simple and is described only by vertical transport across the TMD in the out-of-plane direction; in this architecture, no lateral transport occurs through the TMD interlayer. The lack of in-plane conduction through the device potentially mitigates material quality effects that normally degrade device performance[150]. As such, the lateral conductivity of the TMD is inconsequential.

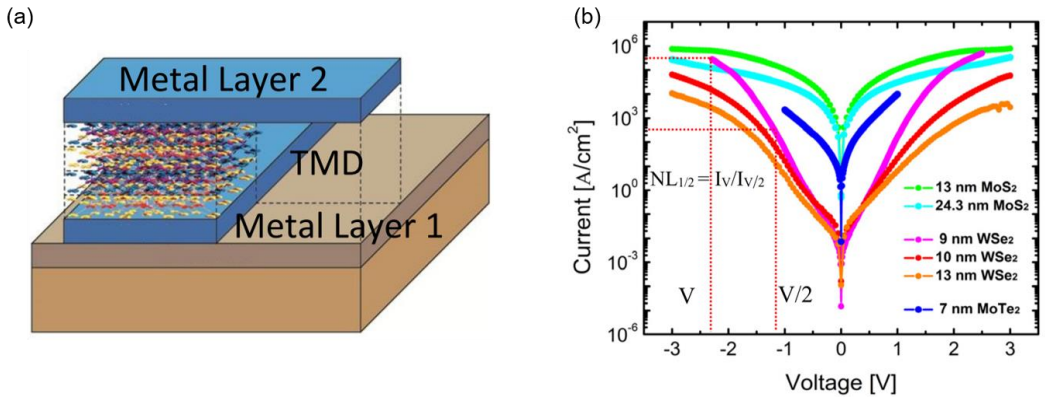

Figure 1.5. (a) A schematic of the metal/TMD/metal vertical heterostructure. (b) I_d - V_{ds} characteristics for a variety of different TMDs and TMD thicknesses. The nonlinearity (NL) is shown as a function of the current at V and V/2. Reprinted with permission from Zhang, F.; Zhu, Y. Q.; Appenzeller, J., Novel Two-Terminal Vertical Transition Metal Dichalcogenide Based Memory Selectors. *IEEE Device Res Conf* 2017. Copyright 2017 by IEEE[21].

The operation of the metal/TMD/metal heterostructure is predicated on the injection from the metal into the semiconductor. When a bias is applied across the structure, three injection mechanisms dictate the total current across the device: direct tunneling, Fowler Nordheim (FN) tunneling, and thermionic emission (TE). When the TMD interlayer is greater than ~3 nm, direct tunneling is mitigated[148, 151], and therefore current flows across the device via electron (hole) injection in the conduction (valence) band of the TMD, either via TE or FN injection.

Because the operation of this device structure depends on the injection of carriers at the metal/TMD interface, the Schottky barrier at this interface dictates device behavior. At low voltages, the Schottky barrier remains large enough that minimal carriers are thermally injected into the semiconductor, and the resulting current density is low. When larger voltages are applied, the Schottky barrier thins due to band bending, and FN tunneling is enabled giving rise to a large on-state current[152]. Of note, only one of the two metal/TMD interfaces dictates device behavior, because due to band bending the interface where carriers eject from the TMD has much smaller ejection barriers than the injection barriers at the injection interfaces. Consequently, the current density across the structure is dominated by the injection interface and minimally influenced by the ejection interface. Theoretically, by selectively choosing TMD and metal pairings, the Schottky barrier at the metal/TMD interface can be tuned to yield low off-state currents with sufficient on-state currents to maximize the on/off ratio of the device.

The ability to tune the device performance by selecting different metal/TMD combinations is illustrated by the current-voltage characteristics of metal/TMD/metal heterostructure devices shown in Figure 1.5 (b). In this case, the gold contacts yield

different injection behaviors for different TMDs and TMD thicknesses. In particular, WSe_2 appears to exhibit the strongest nonlinearity, determined by the ratio of the current density at a voltage V and V/2.

With the recent work on low-temperature synthesis of TMDs (which will be discussed in more detail later), memory select devices have risen as a promising application for metal/TMD/metal heterostructures. In a cross-point memory architecture, each memory element requires a select device in series that regulates current for read and write commands[153]. This select device must exhibit strong non-linearity, operate in both polarities, require low switching power, and have high write endurance. Additionally, to fully maximize the potential of the cross-point architecture, these select devices must be able to integrate into a vertical 3-dimensional array.

One such solution to this design constraint is the use of TMD heterostructures in a steep slope architecture[22]. The nearly infinite theoretical subthreshold swing of a TMD tunneling FET suggests that the device architecture would be well suited for select applications. However, with the current state of TMDs that can be synthesized, the steep slope operation of these devices has not yet been realized.

Recently, select behavior has been demonstrated using a simple metal/TMD/metal heterostructure using exfoliated TMD flakes[21]. In these structures, the Schottky barrier between the metal and semiconductor is theorized to regulate carrier injection, yielding non-linear behavior. This study found WSe_2 to exhibit the best select behavior, which is hypothesized to be due to the difference in barrier heights at the interface between the various contact metals and TMD layers[154]. The performance of the selectors is comparable

with other select architectures including oxides, silicon, and metal-insulator-transition materials[155]. The combination of the potential for BEOL integration and likelihood of TMD selector performance indicates that select devices are a promising entrance point for TMD materials into industrial processes.

1.6 Fermi Level Pinning at Metal/TMD interfaces

One important factor of any electronic device is the contact metal/2D material interface. A number of studies have investigated the characteristics of the metal/2D interface as a function of various properties such as metal work function and defect structure in the 2D film. For example, when a metal is deposited onto a layer of graphene, the work function of the graphene mirrors the metal[156]. In turn, the contact resistance of graphene FETs changes with differing contact metal selection. In the case of TMDs, careful selection of contact metals can yield both n- and p-type behavior in the film[129]. As low contact resistances are typically desired, understanding what metals yield ohmic contact behavior for different materials is a significant portion of the 2D materials field.

This interface has been investigated in detail for a variety of metal/TMD combinations. Smyth et al. demonstrated the chemical relationship between MoS_2 and various contact metals using X-ray photoelectron spectroscopy (XPS)[157]. In this study, scandium and chromium metals interact with MoS_2 with significant covalency, resulting in metal sulfide species at the interface. In contrast, gold yields a predominantly van der Waals interface, as minimal chemical interaction between the gold and MoS_2 was observed. Additionally, the ambient environment during metal deposition influences the

resulting interfacial chemistry. At relatively high deposition pressures, partial oxidation of some metals occurs at the interface, which also influences the interaction of the interface. These differences in chemical interaction at the metal/MoS_2 interface suggest that different metals and metal qualities result in different carrier injection behavior, subsequently modifying device performance.

A critical phenomenon that results from the metal/TMD interface is Fermi level pinning. Gong et al. have performed DFT calculations to investigate the electronic behavior at the metal/MoS_2 interface[158]. Their calculations suggest that even in the case of pristine materials, interactions between the *d* orbitals of the metal and molybdenum result in an interfacial density of states and a reduction of the metal's work function at the interface. The interaction also partially pins the Fermi energy of the MoS_2, resulting in a spread of MoS_2 Fermi energies ranging over 1 eV for the different metals. The change in the TMD's Fermi level and the metal's work function influences the effective barrier height at a metal/TMD interface, which in turn alters injection behavior[159]. Contact geometries can also be used to improve electron injection, where edge contacts result in improved injection efficiencies, especially so for multi-layer TMD devices.

This predicted pinning behavior has recently been corroborated experimentally. Although the Mott model predicts that the effective barrier height at a metal/semiconductor interface solely depends on the metal's work function and the semiconductor's electron affinity, Fermi level pinning adds interface states that induce a deviation from the Mott model[160]. When the Fermi level is strongly pinned, the resulting effective barrier height is minimally dependent on the metal's work function and is dominated by the charge neutrality level of defect states in the bandgap. By probing the effective barrier height of

different metals contacted to MoS_2, a pinning factor can be extracted that describes the strength of the Fermi level pinning. This effect has been demonstrated in a variety of TMDs, where different TMDs exhibit stronger pinning behavior when coupled to a given metal[160].

When defects are introduced into the film, additional gap states are be introduced into the MoS_2, resulting in stronger pinning effects. Chalcogen vacancies have been demonstrated experimentally to significantly increase the pinning strength at the metal/TMD interface[161-162]. As discussed previously, chalcogen vacancies introduce gap states into the TMD. These gap states are susceptible to interaction with the adjacent metal's *d* orbitals, which can pin the Fermi energy at the gap state energy. Local current-voltage measurements performed using conductive AFM can be used to locate individual sulfur vacancies, as shown in Figure 1.6 (a)[162]. By sweeping a bias across the AFM tip, the resulting current-voltage characteristics yield effective barrier heights; by measuring the current at both pristine and sulfur vacancy sites of the MoS_2, a comparison of the pinning factor at defective and pristine sites can be achieved, which show a lower pinning factor (indicating stronger pinning) at defect sites[162]. In addition, the effective barrier height at the defect site reduces by almost 0.2 eV as shown in Figure 1.6 (b), suggesting the Fermi level is pinned to near-conduction band gap states that result from sulfur vacancies[162]. This pinning effect has also been observed using ultraviolet photoelectron spectroscopy (UPS), where the work function of the MoS_2 at the metal/MoS_2 interface is dependent on the work function of the metal used[163].

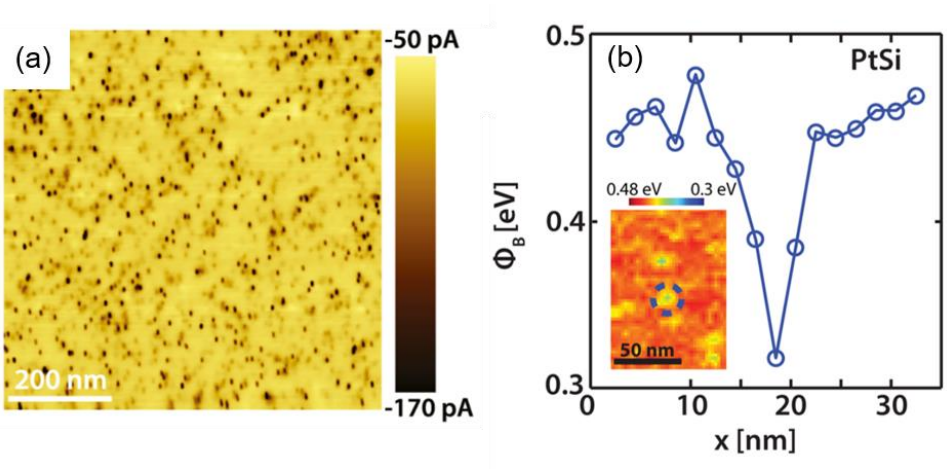

Figure 1.6. (a) cAFM image of a MoS_2 surface. The black dots correspond to sulfur vacancies. (b) The effective barrier height between the MoS_2 and a metallic PtSi cAFM tip as a function of position, corresponding to the inset cAFM map. Reprinted with permission from Bampoulis, P.; van Bremen, R.; Yao, Q.; Poelsema, B.; Zandvliet, H. J. W.; Sotthewes, K., Defect Dominated Charge Transport and Fermi Level Pinning in MoS2/Metal Contacts. *ACS Appl. Mater. Interfaces* 2017, *9* (22), 19278-19286. Copyright 2017 by the American Chemical Society[162].

The pinning strength and resulting metal work function, which dictate the effective barrier height at the interface, are also influenced by a variety of other properties[164-166]. A number of studies have demonstrated both theoretically (via ab initio methods) and experimentally, for an array of metals and TMD, that the extent of adsorption between the metal and semiconductor, the metal's crystal structure, and many electron effects due to charge transfer all significantly influence the injection characteristics at the interface. In addition, these studies show that the number of TMD layers also impact injection efficiency at the interface, which becomes particularly relevant when exploring vertical heterostructures of few- to many-layered TMDs.

A large number of electronic applications require precise control of the electronic structure at the TMD/metal interface. Although decreasing contact resistance by improving

carrier injection efficiency is one of the most common concerns of the TMD/metal interface, certain device architectures exploit the injection interface as the regulating mechanism for device operation[21]. While Fermi level pinning is not necessarily a negative effect, understanding the mechanisms that give rise to pinning and learning how to control pinning behavior is critical for implementing TMDs in electronic device applications.

1.7 Radiation Effects in 2D Materials

Radiation behavior and its negative effects on solid state devices have been a focus of research for over 40 years[167-169]. When exposed to ionizing radiation, unwanted defects and charge carriers can be introduced, decreasing device performance and even causing device failure. These effects are particularly relevant in space and nuclear environments. With the recent interest in 2D materials for electronics applications, various studies have explored the effect of ionizing radiation on 2D materials in order to understand the radiation response of 2D-based devices. Due to the characteristic low dimensionality of 2D materials, their inherent atomic scale implies significant potential for extremely radiation-resistant electronics.

1.7.1 Irradiation of TMDs

A number of studies have explored the effect of electron, ion, and X-ray irradiation on TMD films[170-178]. Exposure to high energy electrons induces significant degradation in TMDs, as observed by TEM[173-174]. Some studies explored using graphene sheets as protective layers to mitigate the radiation damage done to the MoS_2. Interestingly,

graphene films placed below the MoS_2 layer resulted in better protection than graphene placed above; this goes against general intuition, where it would be assumed that a protective barrier above the MoS_2 would reduce the knock-on cross section of the MoS_2 [179-180]. This result suggests that the underlying graphene prevents sulfur atoms from ejection, preserving the MoS_2 quality. As stated previously, these sulfur vacancies introduce defect states into the bandgap, so preserving the physical structure of the film is crucial for electronic applications in radiative environments.

Reports in the literature have used Raman spectroscopy to investigate the degradation of MoS_2 films exposed to ionizing radiation. When exposed to high energy electrons, the peak separation between the A_{1g} and E^1_{2g} peaks increases, with the E^1_{2g} peak experiencing a red shift, indicative of strain within the film[170]. With increasing sulfur vacancies, the restoring force of the in-plane E^1_{2g} phonon node decreases, whereas the A_{1g} out-of-plane phonon node experiences a combination of sulfur vacancies reducing the vibrational restoring force along with an overall decrease of the film's mass, increasing the vibrational restoring force. DFT calculations of the phonon energies as a function of sulfur vacancy concentration agree well with experimentally observed Raman spectra. These results indicate that Raman spectroscopy can be used as an effective yet simple tool to monitor defect response of MoS_2 exposed to electron irradiation.

Similarly, a number of reports demonstrate that proton irradiation of TMDs decrease resulting device performance[171, 175, 181-182]. This irradiation also appears to effect electron and hole conduction differently, where He^+ irradiation suppressed hole transport significantly compared to electron transport in WSe_2 films[175]. Additionally, trapped charge can accumulate at the MoS_2/SiO_2 interface, which act as scattering sites that decrease

electron conductivity. Raman measurements do not show significant changes in the spectra of the MoS_2 itself, suggesting the majority of the device degradation comes from the generation of oxide and interface trap states[171].

Conversely, TMDs appear to be relatively resilient to X-ray irradiation, where device performance does not degrade significantly with X-ray exposure[172]. After exposure to irradiation doses of 1,500 krads, the on/off ratio and subthreshold slope of MoS_2 devices remain unchanged. However, with each X-ray exposure, a small positive threshold voltage shift was observed due to negative charge trapping in the underlying oxide. The physical structure of the MoS_2 was not modified, evidenced by no significant changes to the Raman spectra.

1.7.2 Irradiation of Graphene

In contrast to TMDs, graphene has been demonstrated to be susceptible to degradation when exposed to X-Rays. This can be observed by an increase in the D peak intensity in the Raman spectrum, indicative of an increase in defect density[183-185]. The charge neutrality point (CNP) in graphene FETs shifts, and the resistivity of the film increases[186]. This effect is somewhat reversible by annealing the film in vacuum at 350 ^{o}C, likely due to desorption of oxygen atoms from the graphene surface.

It is important to note that the low energy of the X-Rays used eliminates the case of direct displacement damage of carbon atoms. This implies that there is a secondary effect that degrades the film, which is corroborated by no degradation observed when exposed to X-Rays in vacuum. These results indicate that the surrounding environment strongly influences the radiation effects of graphene films.

Pantelides et al. performed DFT calculations on the oxygen/graphene interaction, and demonstrate different pathways that oxygen can desorb from the graphene surface either destructively or non-destructively[184, 187]. These pathways consist of oxygen forming either O_2 or an OH^- radical when desorbing non-destructively, or pulling carbon from the graphene film to form CO or CO_2 in a destructive manner. Hydrogen can mitigate the degradation of graphene by increasing the amount of oxygen desorbing as a hydroxyl.

Because the surrounding environment significantly influences the radiation response of graphene films, insulating the graphene from the environment should reduce the radiation response when exposed to X-Rays. When encapsulated with hBN, graphene FETs exhibit minor response to ionizing X-Rays, although electron and hole trapping mechanisms are still present at different ionization doses[188].

A similar degradation of a graphene channel, both physically and electrically, is observed when exposed to high energy electrons[189-190]. When exposed, the D peak intensity in the Raman spectrum increases, indicating an increased disorder within the film. Further exposure leads to a decrease in D peak, at which point the film loses its graphitic nature and transitions to amorphous carbon. Current-voltage characteristics support this result, where sheet resistance increases with increasing exposure, where eventually the sheet loses all conductivity and becomes an insulator.

Similar effects are observed in graphene that is exposed to ion irradiation[191-193]. Raman measurements show an increase in D peak intensity, and FETs exhibit a CNP shift. Additionally, the graphene transitions to a more insulating state, leading to a decrease in conductivity.

CHAPTER 2. GOALS AND ORGANIZATION OF THIS THESIS

2.1 Goals

While significant work has been performed to demonstrate the viability of numerous applications of TMD heterostructures, the majority of these studies utilized TMD materials obtained using non-scalable methods. Although efforts to develop low temperature synthesized TMD films demonstrate feasibility, the impact of the resulting lower quality on electronic device performance has not yet been explored in detail. Therefore, the goals of the work presented in this dissertation are (i) develop a low-temperature synthesis process for TMDs on arbitrary substrates and understand the fundamental reaction mechanisms driving the synthesis (ii) realize an understanding for how material quality (defects, grain boundaries, etc.) influence electronic performance (iii) understand how various forms of radiation generate defects and influence device performance of 2D heterostructures (iv) elucidate how wafer-scale quality of TMDs impacts Fermi level pinning strength at the TMD/metal interface. These goals will be achieved through synthesis process optimization for TMDs and TMD heterostructures in order to generate a variety of device architectures, which will subsequently be characterized and exposed to various post-processing conditions.

2.2 Organization

CHAPTER 3 introduces a wet transfer process that is commonly used in 2D materials research and discusses common issues involved with the transfer process. In addition, the limitations in what cleaning methods can be used to remove polymeric contaminants is discussed. Graphene is used as an example, where AFM and XPS are used to show the difficulty of removing both photoresist and Poly(methyl methacrylate) (PMMA) residues from various process steps. Efficiently cleaning the graphene film requires cleaning processes that induce damage into the film, indicating the importance to minimizing the number of process steps involving polymeric layers. Electrical measurements demonstrate the effect of these polymeric residues, where significant doping and hysteresis are observed in contaminated graphene devices.

Error! Reference source not found. revolves around developing and optimizing a low temperature synthesis process for MoS_2 on SiO_2 substrates using a plasma assisted technique. The influence of the molybdenum initial film composition on resulting MoS_2 film quality is explored using a fully *in situ* synthesis process, where molybdenum deposition and subsequent sulfurization are performed without breaking vacuum. Although oxidized initial films thermodynamically react more favorably with H_2S, metallic initial films are found to yield higher quality MoS_2. In addition, layer-by-layer cyclic synthesis is found to result in higher quality films exhibiting good uniformity while enabling precise thickness control. Two-terminal device structures are measured, which indicate that variable range hopping dominates lateral conduction. High temperature post-synthesis anneals were performed to induce structural and chemical changes into the films, which

were then correlated to changes in in-plane conductivity. Specifically, grain size was found to be the biggest limiter of in-plane conduction.

CHAPTER 5 takes the synthesis process discussed in CHAPTER 4 and optimizes it for synthesis on gold substrates. Performing the synthesis with metallic initial molybdenum films results in minimal MoS_2 synthesis, in contrast to results for films synthesized on SiO_2. Conversely, oxidizing each molybdenum layer prior to sulfurization yields strong MoS_2 Raman and XPS signals. The substrate's effect on synthesis is discussed from the perspective of the thermodynamics of the sulfur interactions with both the substrate and molybdenum layers, where substrates that interact more strongly with sulfur require oxidizing each molybdenum layer to favor the molybdenum/sulfur interaction. Purely vertical heterostructures are fabricated in order to mitigate the limitations of in-plane hopping conduction. Architectures with and without tunnel barriers are investigated, which demonstrate switching and tunneling behaviors, respectively.

CHAPTER 6 discusses the radiation response of two heterostructure device architectures to understand various defect effects on device performance, both of which utilize MoS_2 synthesized at low temperature directly on gold substrates. The first study investigates the radiation response of passivated graphene FETs. Hydrogen and oxygen complexes at the graphene/dielectric interface are found to induce device degradation, as determined from low frequency $1/f$ noise measurements. The degradation is found to be reversible by high temperature annealing, indicating that no permanent physical damage is done to the devices. The second radiation study utilizes the tunneling structures discussed in CHAPTER 5. Two different interlayer dielectrics are used, Al_2O_3 and HfO_2, which provide differing work functions and oxidation states. When exposed to increasing proton

fluences, the Al_2O_3 interlayer devices exhibit and shift in the FN threshold voltage, whereas the HfO_2 interlayer devices do not. DFT calculations are performed, which reveal the defect energy states introduced from passivated an unpassivated oxygen vacancies. The defect states introduced by passivated oxygen vacancies in Al_2O_3 align closely in energy with the MoS_2 conduction band, suggesting that trap assisted tunneling is enabled when these defects are induced via proton irradiation. Both of these experiments highlight the importance of intelligently selecting complementary materials in these heterostructure devices.

CHAPTER 7 expands upon CHAPTER 4 using the low temperature synthesis process to grow WS_2 films. WS_2 is successfully synthesized at 400 ^oC onto SiO_2 substrates, which is confirmed through Raman and XPS. As both MoS_2 and WS_2 films can be synthesized, MoS_2/WS_2 heterostructures are directly synthesized. Raman and XPS confirm the presence of both materials in the structures, and PL suggests a typical type II band alignment at the heterojunction. Purely vertical devices are fabricated from the heterostructures, which do not exhibit rectifying behavior. The temperature dependence of the FN threshold voltage is observed, which indicates that the Fermi level and associated gold contact work functions are strongly pinned to defect states in the TMD band gaps, enabling direct electron injection into the MoS_2 conduction band.

CHAPTER 8 reports on the effect of wafer scale MoS_2 material quality on Fermi level pinning at the MoS_2/metal interface. MoS_2 films synthesized at differing temperatures are used to create metal/MoS_2/metal heterostructures, in order to explore the temperature dependence of the electron injection mechanisms from metal into MoS_2. Different contact metals are used to yield interfaces with different effective barrier heights. Device models

are used to extract the effective barrier height at different metal/MoS_2 interfaces. UPS measurements are used to obtain the work function of each metal/MoS_2 interface, and XPS is used to understand the extent of covalency at each interface. In particular, gold was found to exhibit a significant covalency with low quality MoS_2, resulting in significant pinning behavior at the gold/MoS_2 interface. Conversely, platinum exhibited inert behavior when coupled to MoS_2, resulting in defect-independent Fermi level pinning behavior.

CHAPTER 9 contains a summary of the work presented in this thesis, as well as suggestions for further work to continue these experiments. This future work includes further optimization of low temperature synthesis on additional substrates, achieving device behavior that is not limited by in-plane conduction effects, expanding synthesis to selenide TMD systems, further exploring the radiation resistance of additional heterostructures, and investigating Fermi level pinning effects at interfaces of different metals with lower work functions coupled to differing TMDs.

APPENDIX A includes details and specifications on the synthesis and characterization tools used in this thesis work. In addition, details on the device modelling performed in CHAPTER 3 and CHAPTER 8 is provided.

The project or effort depicted in this work was sponsored by the Department of the Defense, Defense Threat Reduction Agency, contract #HDTRA1-16-1-0032. The content of the information does not necessarily reflect the position or the policy of the federal government, and no official endorsement should be inferred.

CHAPTER 3. EFFECTS OF POLYMERIC RESIDUES ON 2D MATERIALS

One key issue that limits 2D materials from being fully integrated into industrial CMOS processes is the requirement and effects of polymer-based processes. Standard 2D fabrication processes utilize various polymeric films, whether as photolithographic resists or structural support layers for transfer steps. These polymer layers are difficult to completely remove and commonly leave residues and contaminants behind[194]. In traditional CMOS processes, these residues are easily removed using plasma or ashing steps. However, due to 2D material's atomic nature, they are extremely sensitive to these cleaning steps, as they often result in defect generation in the 2D film[195-196]. Other cleaning methods such as electric current annealing[197] or chloroform treatments[198] have been explored with limited success. A such, this chapter will overview the influence of polymeric residues on graphene films to demonstrate the sensitivity of 2D films to foreign contaminants.

An essential component of microfabrication techniques is photoresist, used to pattern features on a microfabricated chip. Fabricating a graphene FET commonly involves a two-level mask process, where the channel and contacts are patterned separately[199]. When defining the channel, photoresist is patterned to cover only the channel area, leaving all unwanted graphene exposed. The sample is then exposed to an oxygen plasma to etch away the exposed graphene, whereupon the remaining resist is stripped using a solvent, leaving

patterned graphene channels. However, the oxygen etch process heats the sample, curing a small layer of photoresist on top of the graphene.

Figure 3.1 (a) shows an AFM image of a monolayer graphene channel covered with cured Microposit s1813 photoresist residue, where the dark edges on the left and right correspond to the SiO_2 substrate and the central rectangle corresponds to the channel. Three traces are shown, which correspond to the topography profiles shown in Figure 3.1 (b). Inspection of the topography profiles in Figure 3.1 (b) reveals a step height of approximately 10 nm between the substrate and channel. In the monolayer, graphene has a thickness of 0.4 nm[200], 50 times thinner than the measured step height. This residue can significantly influence device performance, especially in the case of heterostructure architectures, where ultraclean interfaces are required for optimal device performance[149].

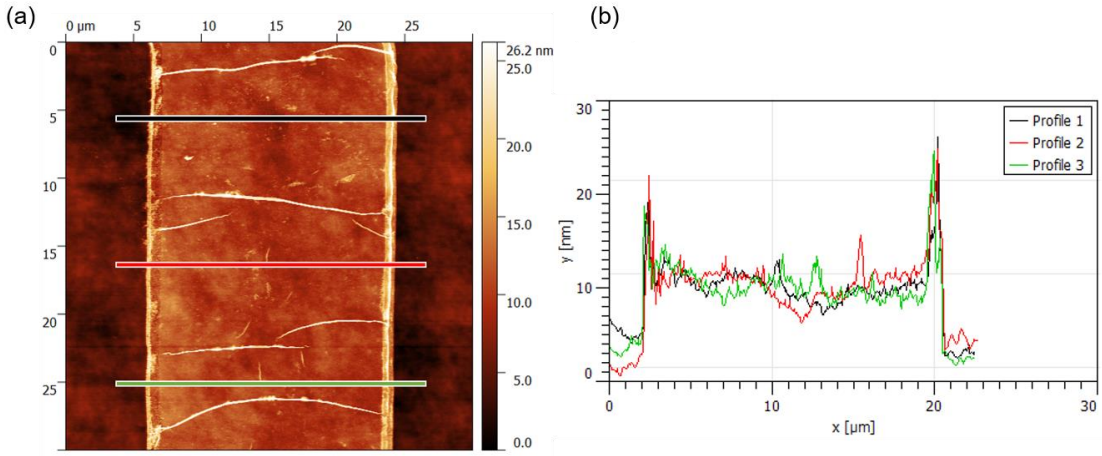

Figure 3.1. (a) AFM image of a patterned graphene channel with photoresist residue. The black, red, and green traces correspond to the topography profiles shown in (b). The height profiles shown in (b) indicate a total thickness of approximately 10 nm.

In order to prevent the photoresist from curing onto the graphene during plasma etching, HMDS was spun onto the graphene prior to s1813 photoresist. HMDS is commonly used as an adhesion layer, and in this case acts as an interlayer between the photoresist and graphene film to mitigate curing effects caused by heating during plasma etching. Figure 3.2 shows an AFM image of the edge of a graphene channel that was pre-treated with HDMS prior to s1813 photoresist deposition. The left region of the image corresponds to the graphene channel, and the right side corresponding to the underlying SiO_2. The step height between the graphene and substrate appears to be significantly reduced, resulting in an average height difference of only 1.2 nm in the lower portion of the image. However, inspection clearly shows a large number of remaining particulates and contamination, notably at the channel's edge in the upper half of the image.

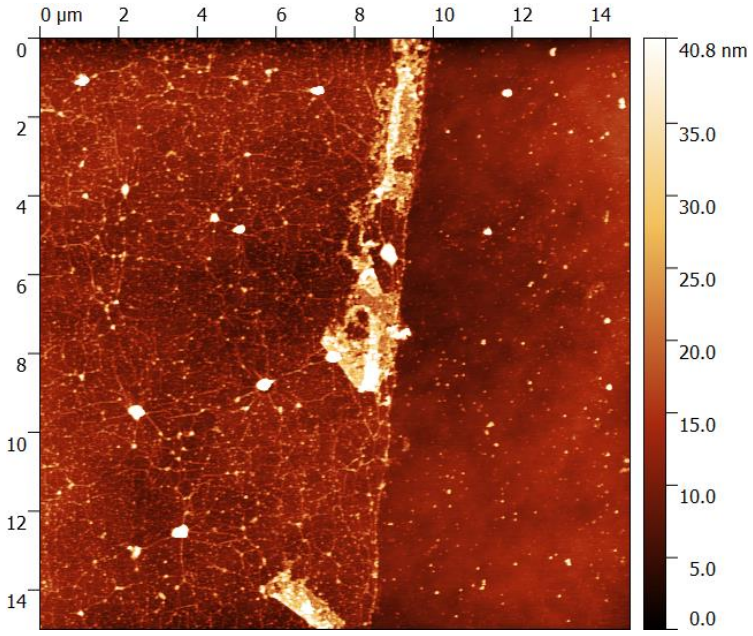

Figure 3.2. AFM scan of a graphene FET pre-treated with HMDS. The left side of the image corresponds to the edge of the graphene channel, and the right side of the image corresponds to the SiO_2 substrate.

Prior to patterning the graphene channel, the graphene must be moved from its synthesis substrate (in this case copper foil) to the target SiO_2 substrate. This is commonly achieved by using a standard wet transfer process, in which PMMA is spin-coated onto the graphene to provide structural support during the transfer step and is removed at the end of the transfer process using acetone[15]. However, fully removing the PMMA is difficult, as some amount of residue is commonly left behind. It is likely then that the particulates seen in Figure 3.2 are remnants of the PMMA film that was used to transfer the graphene onto the SiO_2.

To verify the source of the particulates in Figure 3.2, XPS was performed on the graphene film. A strong satellite peak is present at 289 eV, corresponding to the carbon-oxygen double bond that is characteristic in PMMA[201-202]. The PMMA residue present on the graphene film has been shown to negatively influence device performance by doping the film and decreasing mobility[202]. Additionally, any residue will prevent the formation of ultra-clean interfaces in heterostructure architectures. As such, its removal is imperative for high quality device operation.

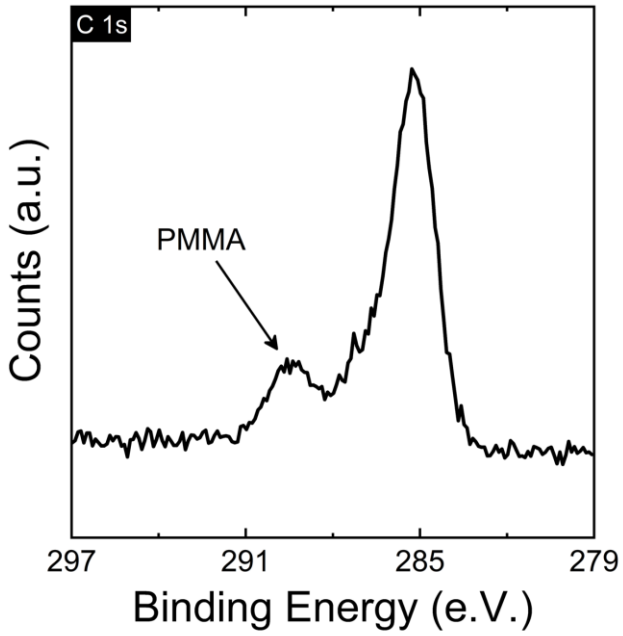

Figure 3.3. C 1s XPS spectrum of the HDMS pre-treated graphene film shown in Figure 3.2. The peak at 289 eV is highlighted as the PMMA peak.

To remove the remaining PMMA residue, the patterned graphene film was submerged in Microposit 1165 resist remover for 20 seconds. Figure 3.4 (a) shows an AFM image of the graphene channel exposed to 1165 resist remover, with the left half of the image corresponding to the graphene channel and the right half corresponding to the underlying SiO_2. The number of particulates is drastically reduced, and the edge of the channel exhibits a step height of only 0.59 nm, further approaching the theoretical 0.4 nm predicted step height. However, there are still a significant number of large particulates remaining. Additionally, the channel is visibly torn near the top (and to a lesser extent the bottom) of Figure 3.4 (a), suggesting that the 1165 resist remover aggressively attacks the residue to the point that it begins lifting the graphene off of the substrate. Due to the fragility of the graphene channel, further exposure to 1165 resist remover was avoided.

Figure 3.4 (b) shows the C 1s XPS spectra of the graphene channel exposed to 1165 resist remover. The characteristic PMMA peak present at 289 eV has significantly reduced in intensity, corroborating the results shown in Figure 3.4 (a) that the amount of PMMA residue has in fact decreased.

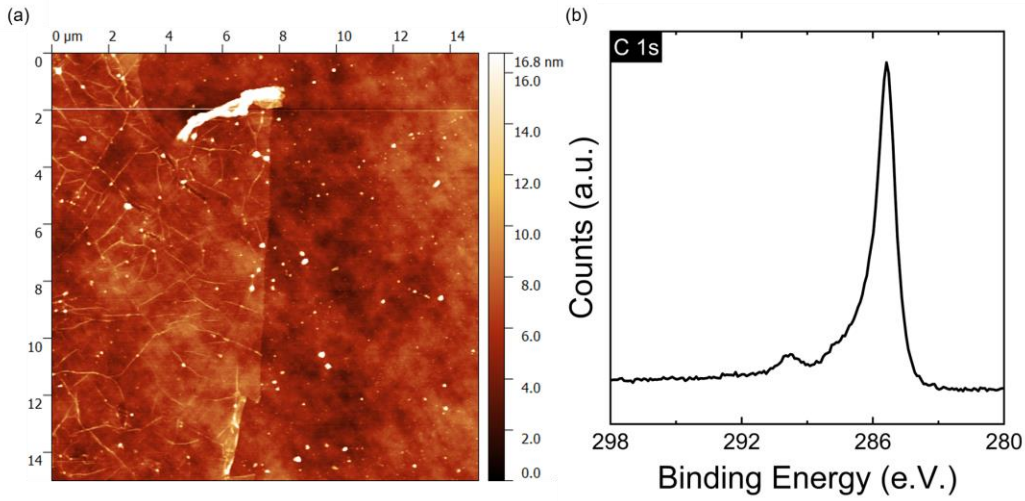

Figure 3.4. (a) AFM image of a graphene channel exposed to 1165 resist remover. The left half of the image corresponds to the graphene channel, and the right half corresponds to the underlying substrate. (b) C 1s XPS spectra for the graphene film exposed to 1165 resist remover, which exhibits a noticeably weaker PMMA satellite peak.

To determine the effect of the PMMA residue on the electrical performance of the films, the graphene FETs were electrically characterized. Two different samples were measured, one that was exposed to 1165 resist remover and one that was held as a control. The transfer curves for two representative devices, one from each sample, are shown in Figure 3.5. Three different effects can be observed from the two different sample's electrical characteristics. First, a large hysteresis is present in the control sample, whereas the sample with less contamination exhibits minimal hysteresis. Second, the position of the CNP (or Dirac point) of the contaminated sample is significantly further from 0 V,

indicating that the graphene is significantly doped[202]. Third, the mobility of the clean graphene FET, extracted using the slope of the transfer curve[203-204], is significantly higher than the contaminated sample (1,623 cm^2/Vs versus 644 cm^2/Vs, respectively). In all cases, it is evident that the PMMA residue significantly reduces the electronic quality of the graphene devices.

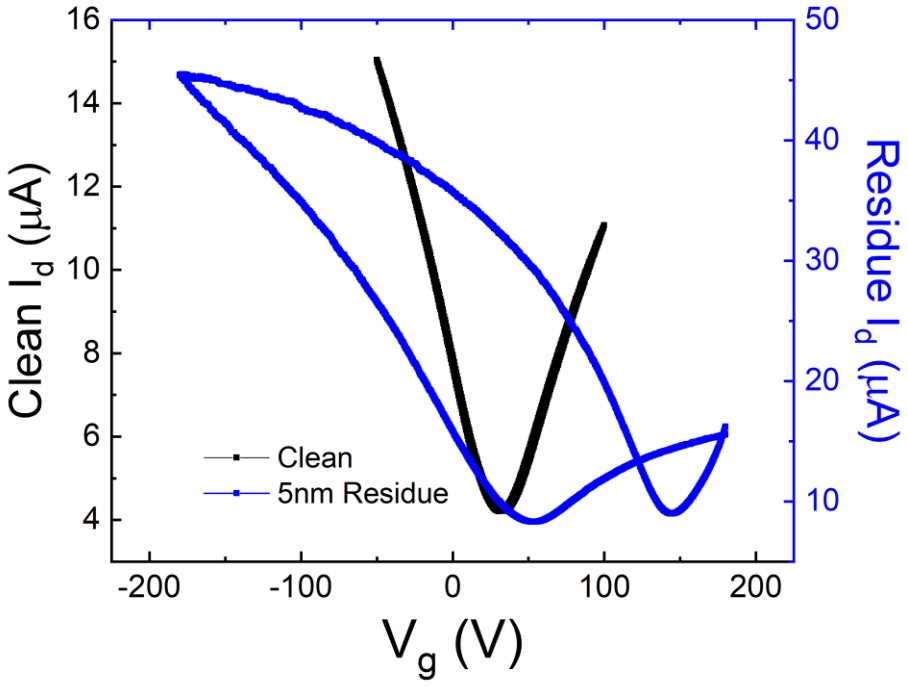

Figure 3.5. Transfer curves for two graphene FETs, one device exposed to 1165 resist remover (black curve/axis) and one control device (blue curve/axis). Significant hysteresis and doping are observed in the contaminated device.

The negative impact that transfer residues induce onto graphene films are analogous to effects of polymeric residue on TMD films[205-206]. While a number of studies have explored various cleaning and transfer techniques to mitigate the amount of residual polymer on 2D films, these techniques may damage the 2D film itself and inherently

include inconsistencies from experiment to experiment. Therefore, developing processes that remove the need for a dedicated transfer step would more effectively preserve the cleanliness of the as-synthesized film, preventing contamination effects from degrading device performance and enabling pristine interfaces in heterostructure architectures.

CHAPTER 4. OPTIMIZING LOW TEMPERATURE SYNTHESIS OF MOS_2

Because the transfer process of 2D materials typically leaves residues that influence device performance and prohibit perfectly clean interfaces, direct synthesis of 2D materials onto the desired end-use substrate is crucial. Although CVD[67, 207-208], MBE[76, 79], and thin film reaction[68, 209] synthesis methods have demonstrated controllable synthesis of high quality MoS_2 films, the majority of the techniques used in these studies require high temperatures. The high temperature requirement precludes these techniques from being used in BEOL processes. Plasma-assisted techniques have been investigated in order to reduce the required temperature for successful synthesis[82], although little work has been done to explore the reaction mechanisms of low temperature synthesis techniques in detail.

Therefore, this work explores the effects of various process parameters on the low temperature thin film reaction synthesis of MoS_2. Performing the entire synthesis in a single vacuum environment enables strong control over different process variables, most importantly the initial Mo film composition. Previous thin film reaction experiments in literature involve depositing and sulfurizing Mo in separate environments, meaning the deposited Mo will oxidize when removed from the initial film's deposition chamber. In contrast, this work explores the effect of initial film composition (metallic or oxidized Mo) on subsequent MoS_2 quality. Varying initial film composition, sulfur delivery, and temperature provides a variety of conditions that can be used to determine reaction trends and mechanisms. Using a plasma-assisted thin film reaction synthesis method, nearly

stoichiometric MoS_2 is synthesized at low temperatures from both metallic and oxidized Mo initials film, enabling a fundamental investigation of the initial film's effect on low temperature synthesis. In order to determine the fundamental causes limiting electronic performance of the low-temperature synthesized materials, high-temperature anneals under different atmospheric conditions are performed to induce changes in film structure and composition.

4.1 Overview of Synthesis Technique

SiO_2 (300 nm)/Si wafers were used as the substrate for low-temperature MoS_2 synthesis. Standard acetone/isopropyl alcohol solvent cleans were performed on the substrates prior to loading into the synthesis chamber. MoS_2 synthesis was performed entirely in an ultrahigh vacuum (10^{-9} Torr) system. The sample is heated by a Veeco VA-2-SSH substrate heater to a synthesis temperature of either 400 or 800 ^{o}C, and a liquid nitrogen cryoshroud is used as a cold trap to freeze out unwanted contamination in the growth atmosphere. The cryoshroud also thermally isolates the surrounding growth environment from the hot substrate, so that only the stage reaches the synthesis temperature. Additionally, the shroud freezes out unwanted gaseous contamination, ensuring a "clean" environment. Prior to deposition, the substrates were cleaned and pretreated at the synthesis temperature in a H_2S flux or a H_2S plasma.

Initial Mo containing films were deposited onto the substrate via sputtering. The MBE chamber is backfilled with argon to 20 mTorr, and Mo is sputtered at 20 W from a metallic Mo source. The sputter duration determines the resulting metallic Mo film

thickness. To convert the Mo monolayers to MoO_x films, the sample is cooled and moved out of the growth chamber into the load lock, which is then vented and exposed to atmosphere for 10 min, whereupon the Mo oxidizes. The sample is then moved back into the chamber and brought back to synthesis temperature. Sulfur is delivered via H_2S, either as a gas or as a plasma. In the case of H_2S plasma, the H_2S is injected through an electron cyclotron resonance plasma operating at 300 W and 2.45 GHz. The flowrate of the H_2S is 8 sccm in both cases, resulting in a background pressure of approximately 10^{-5} Torr.

This two-step synthesis process was repeated for cyclic synthesis. Mo films are sputtered for 12 s, and for the case of the MoO_x, the samples are oxidized in the load lock after each sputter step. The initial Mo containing films are soaked in either H_2S or H_2S plasma for 15 min per cycle. This cycle is repeated to achieve the desired number of MoS_2 layers. For the cyclic synthesized samples discussed below, four cycles were performed. In all cases, H_2S or H_2S plasma is supplied while the sample is at synthesis temperature.

4.2 Investigation and Optimization of Reaction Variables

Thin film synthesis of MoS_2 occurs when a Mo containing thin film is exposed to a sulfur containing atmosphere. When H_2S is used as the sulfur source, two possible reactions occur based on the initial Mo film's composition

$$Mo_{(s)} + 2H_2S_{(g)} \rightarrow MoS_{2(s)} + 2H_{2(g)} \qquad \textbf{4.1}$$

$$MoO_{3(g)} + 3H_2S_{(g)} \rightarrow MoS_{2(s)} + 3H_2O_{(g)} + S_{(s)} \quad \textbf{4.2}$$

Heyne et al. calculated that the Gibbs free energy of eq. 4.2 is the lower of the two at temperatures above 200 ^{o}C and is therefore the more favorable reaction[69]. Previous work experimentally suggested this favorability between the two reactions, but to our knowledge, no study has been performed to distinctly compare the sulfurization mechanisms of metallic Mo and MoO_x initial films[69].

In order to investigate the sulfurization mechanism of Mo containing thin films, a matrix of three variables was formed to generate eight samples as shown in the sample key of Figure 4.1. Mo was sputtered for 20 s (and oxidized, if applicable), and was exposed to S for 15 min in order to investigate the effects of these variables.

Figure 4.1 (a) shows Raman spectra for the eight samples. Notably, no MoS_2 Raman signal was observed for all samples that were exposed to sulfur via H_2S. We do note that this is in contrast with many MoS_2 synthesis results in literature[60, 79, 210-212]. However, the thin film reactions reported in literature were performed with the synthesis atmosphere at high temperature and pressure. In this case, the cryoshroud keeps the synthesis atmosphere at approximately 77 K, with only the growth substrate reaching the synthesis temperature. Because the synthesis atmosphere is at low temperature, the S precursor may not have the requisite energy for reaction until it comes into contact with the sample surface. When the S species reaches the surface, two competing effects take place: the reaction with the underlying initial Mo film, and a desorption based on the sticking coefficient of the H_2S molecule. If the rate of desorption is higher than rate of

reaction, only a small amount of S will react with the film. These results indicate that minimal reaction occurs in this case, and additional energy is required to facilitate the reaction. The lack of reaction is therefore most likely due to the low environmental temperature.

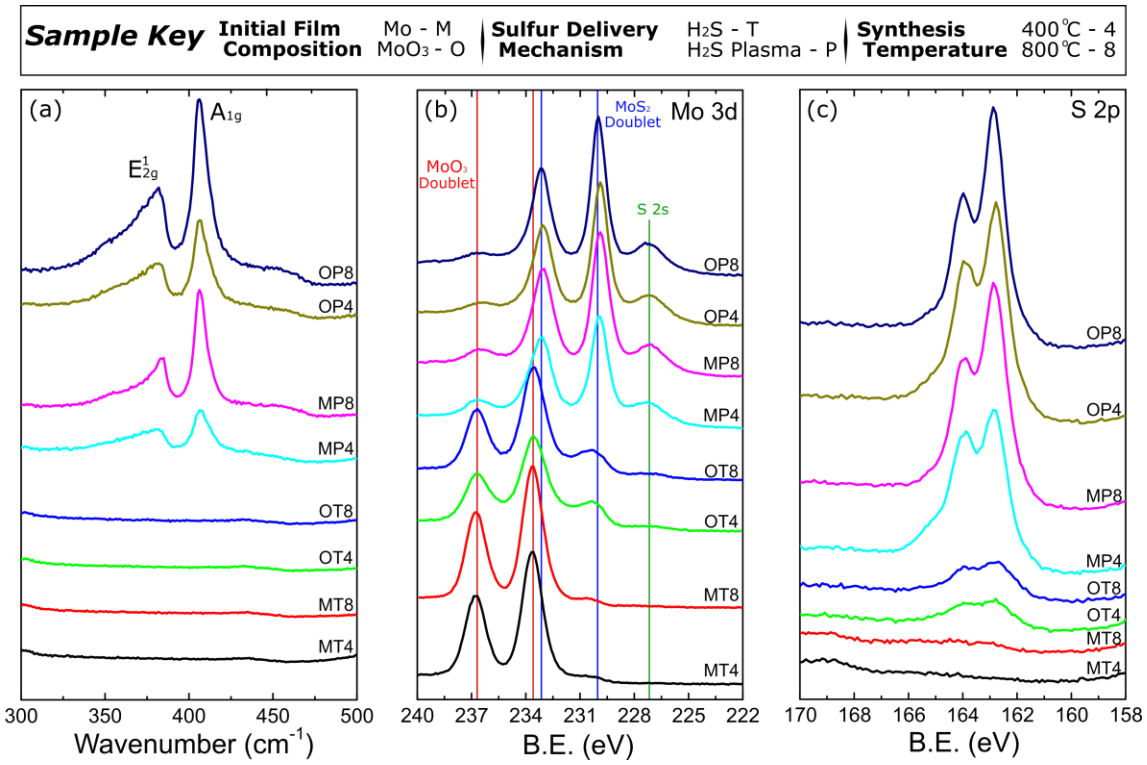

Figure 4.1. Raman (a) and XPS (b) and (c) of eight thin film synthesis conditions. The sample key above denotes the condition of each parameter: initial film composition corresponds to whether the initial Mo film was metallic or oxidized; sulfur delivery mechanism links whether the sample was exposed to H_2S flux directly or to a H_2S plasma; and the synthesis temperature denotes the stage temperature during synthesis. The combination of each of the three digits denotes the synthesis conditions (e.g., MP8 corresponds to a synthesis of metallic Mo using H_2S plasma at 800 C). The positions of the MoS_2 and MoO_3 doublets, as well as the S 2s singlet, are shown. All y-axes have arbitrary units.

Films synthesized at 800 ºC using plasma H_2S exhibit a stronger Raman response than their counterparts synthesized at 400 ºC. Additionally, the A_{1g} and E^1_{2g} peak FWHMs

of the 800 °C syntheses are smaller than their counterparts synthesized at 400 °C. The FWHMs for the four H_2S plasma samples are listen in Table 4.1. Both the increase in Raman signal and sharper peak shape seen with higher temperature are correlated to an improved physical structure[103, 213-214]. This is consistent with the literature, where MoS_2 synthesized at higher temperatures yield higher quality resulting films[68].

Table 4.1 Raman peak FWHMs for the H_2S plasma samples shown in Figure 4.1.

Sample	A_{1g} FWHM (cm^{-1})	E^1_{2g} FWHM (cm^{-1})
MP4	11.12	25.08
MP8	8.2	11.4
OP4	9.7	20.4
OP8	9.4	19.7

Comparing MoS_2 synthesized from metallic Mo initial films versus MoO_x films yields an interesting result. The Raman peak intensity for films synthesized from MoO_x initial films are larger than their counterparts synthesized from Mo, at 400 and 800 °C, respectively. This suggests that the reaction of H_2S with MoO_x is more favorable than H_2S with Mo, which is consistent with literature[69]. However, the FWHM of the peaks from films synthesized using Mo are smaller than the FWHM values of films synthesized from MoO_x (see Table 4.1). These results indicate that while MoO_x is more favorable for the MoS_2 synthesis reaction, Mo initial films yield more ordered, larger domain size MoS_2 films. Specifically, the FWHMs for the MoO_3 samples suggest that the individual grain size is on the order of 5 nm[103].

Figure 4.1 (b) shows the Mo 3d and S 2s XPS spectra for the films synthesized using the eight synthesis conditions. The Mo 3d spectra consists of five peaks: a S 2s peak (227 eV), a Mo 3d doublet corresponding to MoS_2 (230 and 233 eV), and a Mo 3d doublet corresponding to MoO_3 (234 and 237 eV). For all syntheses using H_2S without plasma, the Mo 3d spectra is dominated by the MoO_3 doublet. Additionally, no S 2s peak is present in the spectra. These results indicate that minimal sulfur integrated into the film. This is consistent with the Raman results from Figure 4.1 (a), where all thermal H_2S sulfur delivery films show no Raman signal. However, the two films synthesized from MoO_x using thermal H_2S do show a slightly larger MoS_2 contribution to the Mo 3d spectra, suggesting again that MoO_x is more reactive than metallic Mo. In contrast, all films synthesized using H_2S plasma show significant MoS_2 contribution, the presence of the S 2s peak, and minimal MoO_x contribution to the Mo 3d spectra. These results indicate that S effectively incorporated into the initial Mo containing films, yielding MoS_2. This result is consistent with the Raman results from Figure 4.1 (a) as well.

The S 2p XPS spectra for the eight synthesis conditions are shown in Figure 4.1 (c). Similar trends are observed as in Figure 4.1 (b), where films synthesized with H_2S show minimal sulfur incorporation, with slightly more sulfur incorporation occurring in samples synthesized from MoO_x initial films. This result also supports the assertion that MoO_x is more reactive than metallic Mo, where reaction II (eq. 4.2) can occur more easily. Films synthesized using a H_2S plasma show significantly stronger S signal than films synthesized with H_2S. This further suggests that H_2S plasma is required for the thin film reaction to occur when only the substrate is heated.

Fitting the Mo 3d and S 2p XPS spectra in Figure 4.1 (b,c) yields information on the film's stoichiometry. Details of XPS fitting are discussed below. Stoichiometry is calculated by summing the area of the S 2p spectra and the MoS_2 doublet's contribution to the Mo 3d spectra, and normalizing by the sulfur and molybdenum sensitivity factors, respectively (0.54 and 2.75). The ratio of the normalized peak areas then gives the ratio of S atoms to Mo atoms that are in the MoS_2 chemical state. Stoichiometries for the H_2S plasma synthesized films are as follows: MP4 – $MoS_{1.55}$; MP8 – $MoS_{1.80}$; OP4 – $MoS_{1.86}$; OP8 – $MoS_{1.78}$. Inspection of the stoichiometries for the 400 ^oC Mo and MoO_x samples again suggests that sulfur reacts much more favorably with MoO_x than metallic Mo. However, at higher temperatures (800 ^oC), the stoichiometry of both films are close to identical, which suggests that the higher temperature provides sufficient energy for the less favorable reaction I (eq. 4.1) to occur.

Combining the Raman and XPS results shown in Figure 4.1, a few conclusions can be made. One, H_2S alone is insufficient for sulfurization of a thin Mo containing film when only the substrate is heated. For sulfurization to occur, additional energy must be provided to the H_2S gas, usually provided by heating the growth environment. In our case, plasma is used as a method of providing energy to the S precursor by ionizing the H_2S into reactive S radicals. Other potential means to increase S reactivity include flowing the gas through a thermal cracker or using a more reactive sulfur source. Two, we have experimentally demonstrated that oxidized Mo in the form of MoO_x is in fact more reactive than metallic Mo. The stoichiometries calculated from the XPS shown in Figure 4.1 (b,c) verify that sulfur can incorporate more readily with MoO_x than Mo. And three, metallic Mo films

yield higher quality MoS_2 with larger domain sizes, indicated by the FWHM values of the Raman peaks, listed in Table 4.1.

4.3 Cyclic Synthesis Using Metallic Mo Films

The results of section 4.2 demonstrate that sulfur delivery via H_2S plasma is required for sulfur incorporation at low temperatures when only the substrate is heated. In an attempt to improve quality of the films synthesized at low temperatures, syntheses were segmented into shorter, repeated cycles at 400 ^oC. Four growth cycles involving a 12 s Mo sputter deposition followed by a 15 min H_2S plasma soak were performed. The Mo sputter time determines the thickness of the initial Mo film. For our sputter conditions and MBE geometry, a 12 s sputter time results in approximately one monolayer of Mo atoms on the growth substrate. Assuming one monolayer of Mo atoms converts to a single layer of MoS_2, a given number of cycles during synthesis should result in as many layers of MoS_2.

To determine film thickness, a step edge was created on synthesized films. To generate the step edge, a square of few-nanometer thick PMMA was transferred onto a portion of the film using a standard wet transfer process. The PMMA was then pulled off of the MoS_2 film, stripping the underlying MoS2 with it. Figure 4.2 shows AFM taken across the step edge of a film synthesized using four cycles. The area on the upper left corner of the film represents the underlying SiO_2, with the MoS_2 film occupying the lower right 3/4 of the image. The inset graph shows a topographical trace across the step edge, corresponding to the white arrow. The step height of the film is approximately 2.9 nm, which is consistent with four stacked 0.7 nm individual MoS_2 layers. In the case of a three-

cycle growth process, the measured step edge was 2.15 nm (not shown), which is consistent with three-layer MoS_2. These results suggest that film thickness can indeed be controlled by choosing the number of cycles during synthesis.

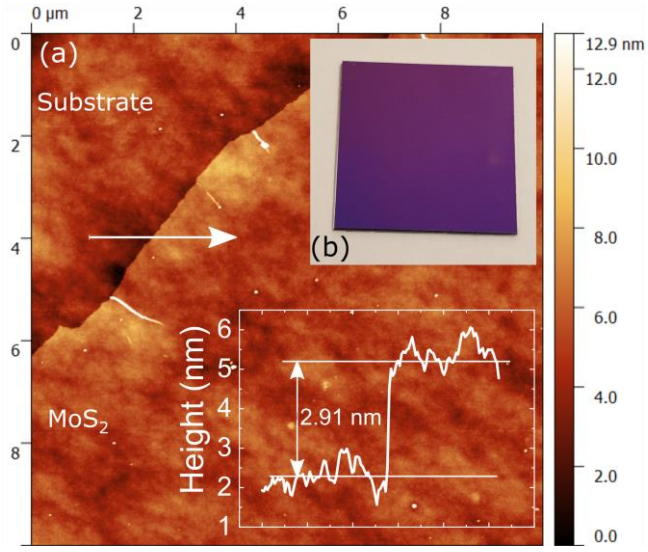

Figure 4.2. (a) AFM scan across the edge of a cyclic 400 ºC synthesized MoS_2 film. The scan area is 10 x 10 µm. The inset corresponds to the white arrow trace across the edge of the film. The extracted film thickness of 2.91 nm is consistent with four-layer MoS_2. (b) Optical image of a 2 x 2 inch synthesized film, exhibiting good uniformity. The discolored dot on the right is due to the placement of a setting pin during synthesis.

The film itself is atomically smooth, having an RMS roughness value of 0.352 nm, nearly identical to that of the underlying SiO_2. Additional scans taken away from the step edge (not shown) yield similar features and RMS roughness values. This implies that the film is locally uniform, and does not contain areas of inhomogeneity or delamination from the substrate[69]. Figure 4.2 (b) (inset) shows an optical image of a 2 x 2 inch film synthesized on an SiO_2/Si wafer. The film exhibits good color uniformity, suggesting that there are no significant variations in film thickness or largescale defects. Additionally, no isolated domains are visible, indicating that the film has totally coalesced.

To verify the thickness of the film measured via AFM, Raman was performed at various points across the three and four-layer films. A representative spectrum for each film is shown in Figure 4.3 (a). For MoS_2, the peak separation between the A_{1g} and E^1_{2g} can be used to determine film thickness[215]. A separation of 24.2 cm^{-1} is consistent with literature values of Raman measured on four-layer MoS_2, while the separation of 23.3 cm^{-1} is consistent with three-layer MoS_2. Both the AFM step height and Raman peak separation for both films indicate that cycling growth steps allows for precise control on resulting film thickness. In theory, any number of planar layers can be synthesized sequentially by performing additional growth cycles.

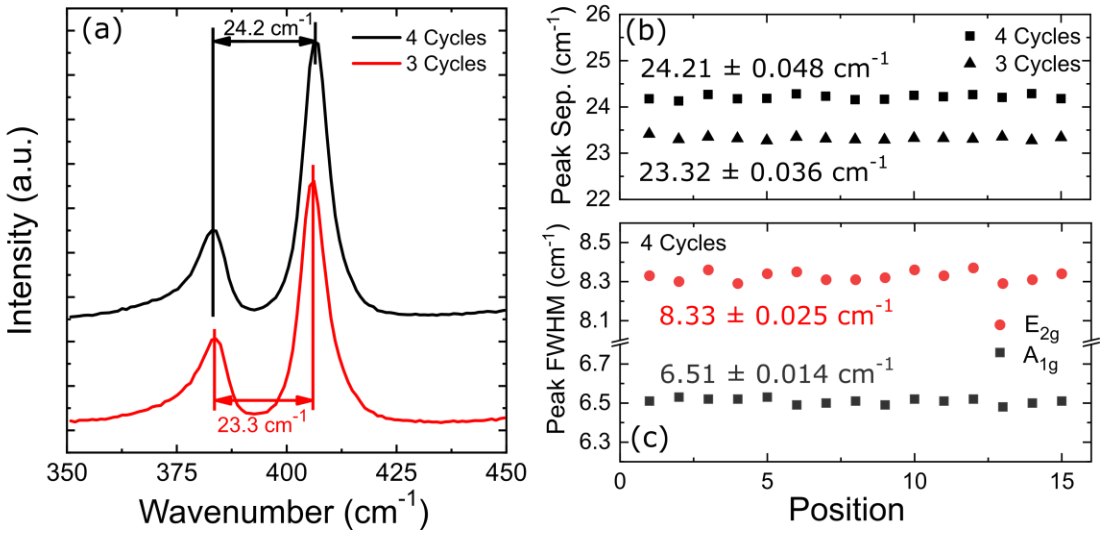

Figure 4.3. (a) Representative Raman spectra for a four and three cycle synthesized films, shown in arbitrary units (a.u.). Arrows denote peak separation. (b) Peak separation for the four and three cycle synthesized films taken at 15 points across the sample. The low deviation indicates high thickness uniformity for both samples. (c) A_{1g} and E^1_{2g} peak FWHMs for the four-cycle synthesized film. Low deviation for both peaks indicates structural uniformity across the film. (b) and (c) share the same x-axis.

Figure 4.3 (b) shows the peak separation of 15 points across the four- and three-layer 2x2 inch films. The small deviation in peak separation for both samples indicate that the film thicknesses are homogeneous and consistently four and three layers across the entire samples, respectively. The Raman peak widths for the four-layer film at the same 15 points are shown in Figure 4.3 (c). Similarly, the small deviation in both A_{1g} and E^1_{2g} peak widths suggest that the film's atomic structure and grain size are globally homogenous[68]. Similar deviations are seen in the three-layer sample (not shown).

Comparing the Raman peak width in Figure 4.3 (c) with the widths of the highest quality equivalent-thickness single step synthesis in Figure 4.1 (a) shows that the films synthesized in a cyclic process have sharper peaks, indicating improved domain size and atomic structure. This supports the idea that slowing down the growth by cyclic synthesis helps improve quality. To validate this assertion, PL was measured on both a four-layer cyclic synthesized film as well as an equivalent thickness single step synthesized film. Five PL spectra are shown for each sample in Figure 4.4. Both the A and B exciton peaks correspond to direct bandgap recombination events at the K and K' point, respectively[48]. The single step synthesis exhibits almost no PL response, only showing a weak B exciton peak located at 625 nm. Conversely, the cyclic synthesized film exhibits a strong A exciton peak at 675 nm, which corresponds to a band gap energy of 1.84 eV. The intensity increase in the PL spectrum suggests that the film has reordered to become more trigonal prismatic, corresponding to the semiconducting 2H allotrope of MoS_2[48]. The variance within each sample's spectra suggest that there is some electronic structure inhomogeneity across the film, despite the film exhibiting atomic structure homogeneity.

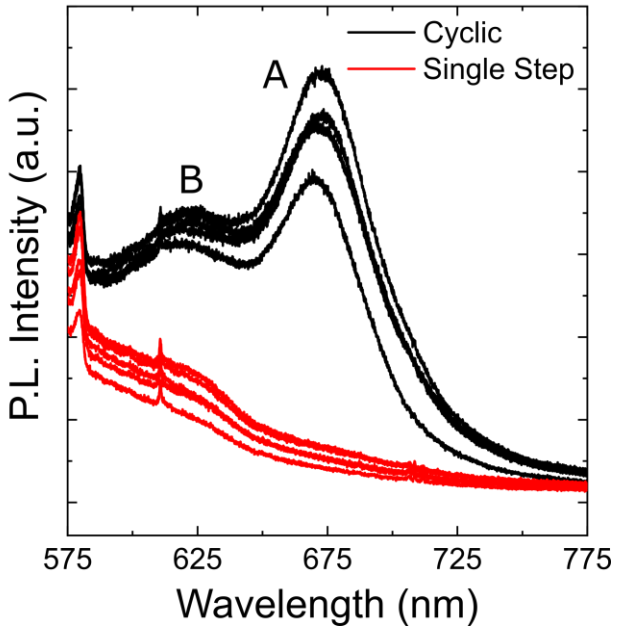

Figure 4.4. Five PL spectra taken at various points across the four-cycle cyclic sample and equivalent sputter duration single step sample. Both curves are shown in arbitrary units (a.u.). A and B peaks are labeled at 675 and 625 nm, respectively.

To calculate stoichiometry and the fraction of unreacted MoO_3, XPS was performed on the four-cycle synthesized MoS_2 film. The Mo 3d and S 2p spectra, along with their respective peak fits, are shown in Figure 4.5 (a,b), respectively. The Mo 3d spectrum can be fitted by the standard five peaks corresponding to the S 2s, a doublet of two peaks corresponding to the MoS_2 contribution of the Mo spectrum (the Mo $3d^{5/2}$ and $3d^{3/2}$ peaks) and a second doublet corresponding to the MoO_3 contribution to the Mo spectrum (another set of Mo $3d^{5/2}$ and $3d^{3/2}$ peaks). All peak widths corresponding to Mo peaks are constrained to be the same. The peak separation between the $3d^{5/2}$ and $3d^{3/2}$ is fixed at 3.1 eV for both Mo doublets, and the area ratio between the $3d^{5/2}$ and $3d^{3/2}$ peaks is constrained at 1.5:1. The positions of the two doublets respective to each other, as well as their peak areas

relative to each other, are allowed to change. All parameters corresponding to the S 2s peak were unconstrained.

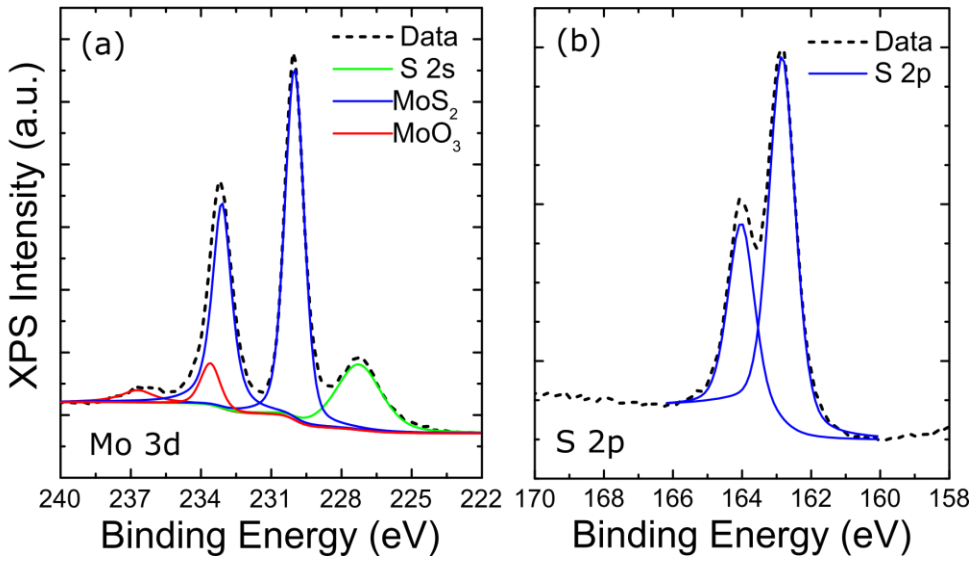

Figure 4.5. Fitted XPS spectra for the Mo 3d (a) and S 2p (b) spectra for a cyclic 400 ºC synthesized MoS_2 film, both shown in arbitrary units (a.u.). In (a), five peaks are present: a S 2s peak, a Mo 3d doublet corresponding to MoS2, and a Mo 3d doublet corresponding to MoO3. In (b), a single S 2p doublet is used to fit the spectrum.

The S 2p spectrum was fit using a single doublet, corresponding to the $2p^{3/2}$ peak and the $2p^{1/2}$ peak. The two peak widths were constrained to be the same, and the peak separation was fixed at 1.18 eV[68]. The area ratio between the $2p^{3/2}$ peak and the $2p^{1/2}$ peak was held at 2:1. Both the Mo spectrum's and S spectrum's peak positions and shapes are consistent with the semiconducting 2H phase of MoS_2[48].

From inspection, the MoO_3 doublet has a minimal contribution to the total Mo 3d spectrum, indicating that the majority of the Mo has sulfurized into MoS_2. Dividing the peak area of the MoO_3 doublet to the area of the MoS_2 doublet yields a MoO_3 percentage of 12%. Because the sputtered initial film is metallic Mo from a metallic Mo source, any

MoO_3 is due to unreacted Mo that oxidizes in ambient atmosphere. A small fraction of MoO_3 therefore indicates that the majority of the initial film sulfurized to form MoS_2.

Stoichiometry is calculated by normalizing the area of the MoS_2 Mo 3d doublet by molybdenum's sensitivity factor (2.75), normalizing the area of the S 2p doublet by sulfur's sensitivity factor (0.54)[216], and taking the ratio of the normalized areas. Doing so yields a stoichiometry of $MoS_{1.82}$. The resulting films are slightly under-stoichiometric, where approximately 10% of Mo–S bonds do not form, leaving the S atomic sites as S vacancies. The stoichiometry improvement seen in the cyclic synthesized film when compared to a single step synthesized film is also in agreement with the PL response seen in Figure 4.4. Kimi et al. have shown that improved stoichiometries result in stronger PL response, which is consistent with our findings[217]. This result suggests that the improvement in stoichiometry significantly improves the electronic structure of the synthesized film.

This under-stoichiometry is in good agreement with the calculated MoO_3 fraction. Approximately 10% of sulfur atomic sites are unoccupied at the conclusion of the synthesis, which then allows the associated unreacted molybdenum to oxidize upon exposure to atmosphere. It is likely that the 12% Mo that is in the MoO_3 state is due to the 10% S vacancies prior to atmospheric exposure and oxidation. It can be assumed that as the initial Mo film moves toward total sulfurization, the fraction of MoO_3 in the resulting MoS_2 film will decrease.

In order to fully compare the effects of initial film composition on resulting MoS_2 quality and validate our initial findings, a cyclic growth using MoO_x initial films was performed. The synthesis process for the MoO_x sample is identical to the four-cycle Mo

sample, except that after each Mo sputter step, the sample was cooled, moved to the load lock, and vented, allowing the sputtered Mo film to oxidize into MoO_x prior to H_2S exposure. After 10 min, the sample is brought back into the main chamber, and the temperature is elevated back to 400 ^oC. The sample was then soaked in H_2S plasma for 15 min, whereupon the cycle is repeated.

Figure 4.6 compares physical characterization results between the metallic Mo and MoO_x cyclic synthesized samples. Raman spectra for the Mo and MoO_x initial film samples is shown in Figure 4.6 (a). The FWHMs of the A_{1g} and E^1_{2g} peaks for the Mo sample are 6.51 and 8.33 cm^{-1}, respectively, whereas the FWHMs of the A_{1g} and E^1_{2g} peaks for the MoO_3 sample are 8.35 and 11.56 cm^{-1}, respectively. The sharper peaks in the Mo sample further support the claim that the films synthesized from initial Mo films have better structure than films synthesized from initial MoO_x films, and is consistent with the results summarized in Figure 4.1 (a).

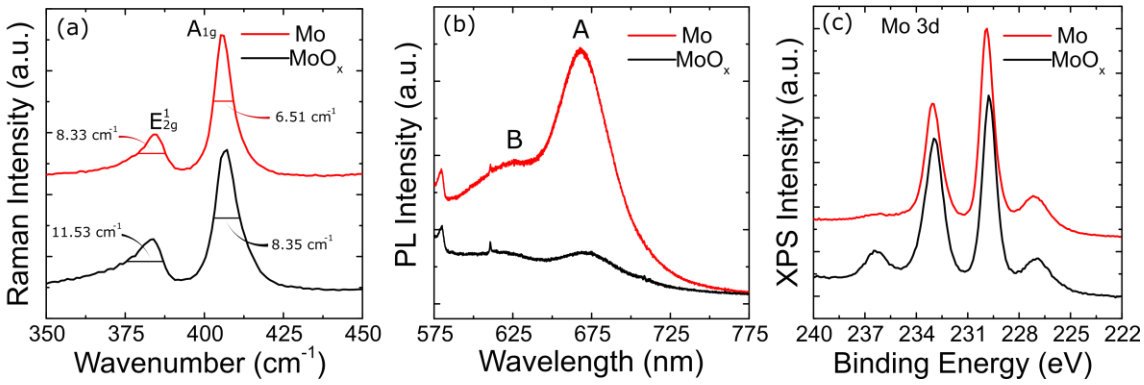

Figure 4.6. Raman (a), PL (b), and the Mo 3d XPS spectra (c) for cyclic synthesized MoS_2 at 400 ^oC, with initial metallic Mo and oxidized MoO_x films. The peak FWHMs are shown in (a), and the PL peaks are labeled in (b). (a)–(c) are all shown in arbitrary units (a.u.).

Figure 4.6 (b) shows PL spectra for cyclic samples using Mo and MoO_x initial films. The results indicate that Mo initial films result in MoS_2 having higher electronic quality. While the Mo sample's spectrum exhibits a strong A peak with a lesser B peak, the MoO_x cyclic sample's spectrum is significantly weaker in intensity. This result agrees with the Raman in Figure 4.6 (a), indicating Mo initial films yield better quality MoS_2. The normalized intensity of the PL spectrum of the MoO_3 cyclic spectra is larger than the normalized intensity of the PL spectrum for the single step Mo sample shown in Figure 4.4. The face that a cyclic growth using MoO_3, which has been shown to yield lower quality MoS_2, does have slightly stronger PL response compared to a single step synthesis using Mo, suggests that slowing the synthesis down via cycling steps has a larger effect than initial film composition on resulting film atomic and electronic structure.

To compare the chemical nature of MoS_2 synthesized cyclically from Mo versus MoO_x initial films, XPS was performed, and the Mo 3d spectra for the two samples is shown in Figure 4.6 (c). From inspection, the MoO_x sample has a much larger MoO_3 contribution to the spectrum. A calculation of the stoichiometry for the MoO_x sample gives an atomic ratio of $MoS_{1.69}$, and the MoO_3 peaks of the Mo spectrum accounts for 19% of the spectrum. The stoichiometries for the cyclic Mo and MoO_x samples are nearly identical, with the difference approaching the magnitude of the error in the calculation. However, a significant difference in MoO_3 fraction is clearly evident, with the MoO_x cyclic film exhibiting more resulting MoO_3. This result appears to contrast our initial experiment, where MoO_x was shown to be more reactive and yielded a higher stoichiometry. It is possible that the use of an H_2S plasma moves the reaction from a thermodynamic regime to a kinetic regime, where the reaction energies of reactions I and II (eqs. 4.1 and 4.2,

respectively) are not the dominant driver for synthesis. A more detailed investigation of the kinetic effects of using H_2S plasma would likely yield a more complete understanding of the effect of initial film thickness on resulting stoichiometry and MoO_3 fraction.

One potential explanation for the larger MoO_3 fraction in cyclic MoO_x synthesized films involves oxygen diffusion through synthesized MoS_2. MoS_2 has been suggested to a good diffusion barrier, similar to other 2D materials[218]. When a bulk Mo or MoO_x film sulfurizes, it sulfurizes from the top down. Therefore, the top layer of MoS_2 can be assumed to be more completely sulfurized than the underlying layers. When the film is then exposed to atmosphere, any unreacted Mo atoms that oxygen can reach will oxidize, and all Mo can be accounted for as either MoS_2 or MoO_x. In the cyclic synthesis cases, both films synthesized from Mo and MoO_x yield closely matching stoichiometries and MoO_3 fractions. For example, the film synthesized from Mo yields a stoichiometry of $MoS_{1.82}$ and a MoO_3 fraction of 12%; the stoichiometry of 1.82 implies that approximately 10% of Mo atoms are unreacted, which then oxidize in atmosphere, yielding the measured 12% MoO_3 fraction. However, when calculating the MoO_3 fraction in the single step syntheses shown in Figure 4.1, both MP4 and OP4 yield similar MoO_3 fractions, 16% and 14%, respectively. OP4 follows the same trend, where the stoichiometry of 1.86 and MoO_3 fraction of 14% are in agreement within the error of the fit. However, MP4's MoO_3 fraction significantly deviates from the stoichiometry, exhibiting only a 16% MoO_3 fraction despite a low stoichiometry of 1.55, which would in theory yield a MoO_3 fraction of around 25%.

The significant mismatch in the single step metallic Mo initial film's stoichiometry and MoO_3 fraction suggests that not all of the unreacted Mo oxidized when exposed to atmosphere. In the single step case, the top of the film will sulfurize more completely[69],

which would then act as an oxygen diffusion barrier to the underlying unreacted Mo atoms, leaving them in a metallic Mo state. However, in the case of the single step MoO_x sample, the unreacted underlying Mo atoms are already in an oxidized state, implying that all Mo is either in the MoS_2 or MoO_3 phases. When the synthesis is broken into cycles, each cycle is exposed to the H_2S plasma for the same amount of time as the entire single step syntheses, which allows the deposited Mo layer to more completely sulfurize[69], decreasing the overall unreacted Mo fraction. To better understand this phenomenon, *in situ* characterization would be necessary in order to probe the Mo state prior to exposure to atmosphere. Future work will continue to explore this diffusion mediated phenomenon.

In order to further characterize the electrical behavior of a MoS_2 film synthesized via cyclic sulfurization of Mo, two-terminal temperature-dependent conductivity measurements were performed. Devices were fabricated from the 400 ^oC four-layer MoS_2 films synthesized from metallic Mo initial films, and a variable range hopping (VRH) model is used to describe the in-plane conduction of the low-temperature synthesized MoS_2. Typically, VRH occurs due to defect-dominated conduction, where charge carriers "hop" from defect site to defect site. Because the trapping and de-trapping rate are temperature dependent, a change in temperature results in a change in conductivity. Previous work has been performed on applying the VRH model to explain conduction through TMD films[76, 219-222]. The VRH model for conductivity in a two-dimensional semiconductor is[219, 223-224]

$$\sigma(t) = \sigma_0 T^{0.8} \exp\left[-\left(\frac{T_0}{T}\right)^{1/3}\right] \quad \textbf{4.3}$$

where σ_o is a scaling constant an T_0 is a fitting parameter of the form

$$T_0 = \frac{13.8}{k_B N(E_F)\xi^2} \quad \textbf{4.4}$$

where k_B is Boltzmann's constant, $N(E_F)$ is the density of defect states at the Fermi level, and ξ is the localization length [with the dimension (m)]. Localization length has been correlated to domain size, and determines how efficiently a carrier can move through the film[225]. It refers to how confined a charge carrier is, where a smaller value implies that the carrier is more confined to a certain location. Recent work has shown that grain boundaries significantly reduce the localization length, which then increases hopping conduction.

Temperature dependent conductivities for three device sizes are shown in Figure 4.7, where $\sigma T^{0.8}$ is plotted on a logarithmic scale versus $T^{-1/3}$. All three devices exhibit similar linear trends, suggesting that VRH is a likely conduction mechanism. The strong temperature dependence and good agreement with the VRH model suggests that there is a relatively high defect density within the film, likely due to small grain sizes and unreacted areas of MoO_x. The relatively large FWHM values of the A_{1g} and E^1_{2g} Raman peaks indicate that the individual domains are on the nanoscale[103]. Thus, the film contains a high density of grain boundaries, which act as trap and scattering sites, which inhibit traditional carrier mobility as well as facilitate hopping conduction.

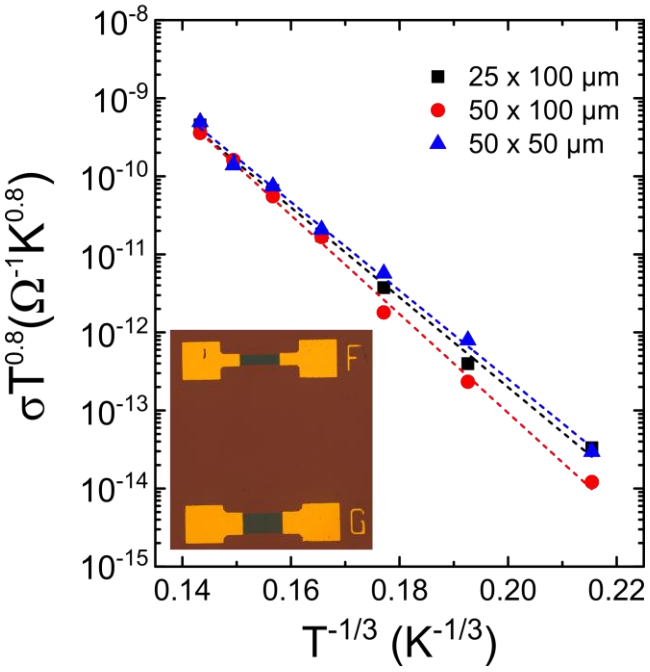

Figure 4.7. Temperature dependent conductivities extracted from three device sizes fabricated from 400 ºC cyclic synthesized MoS_2. Inset shows an optical image of a 25 x 100 µm (F) and 50 x 100 µm (G) device.

To concretely determine the grain structure of the film, STEM was performed on the 400 ºC synthesized MoS_2 used to fabricate the devices shown in Figure 4.7. Figure 4.8 shows a plane-view STEM image containing a number of grains, where all grains are on the order of 5 nm in diameter. Because the individual grains are so small, they are relatively difficult to resolve, so select few have been highlighted in color to assist in observation. The inset of Figure 4.8 shows the fast Fourier transform of the plane-view image, indicating that the film is primarily oriented along the [0001] direction[69]. The nanocrystallinity observed using STEM confirms the Raman peak widths seen in Figure 4.3 and Figure 4.6 is primarily due to grain size effects.

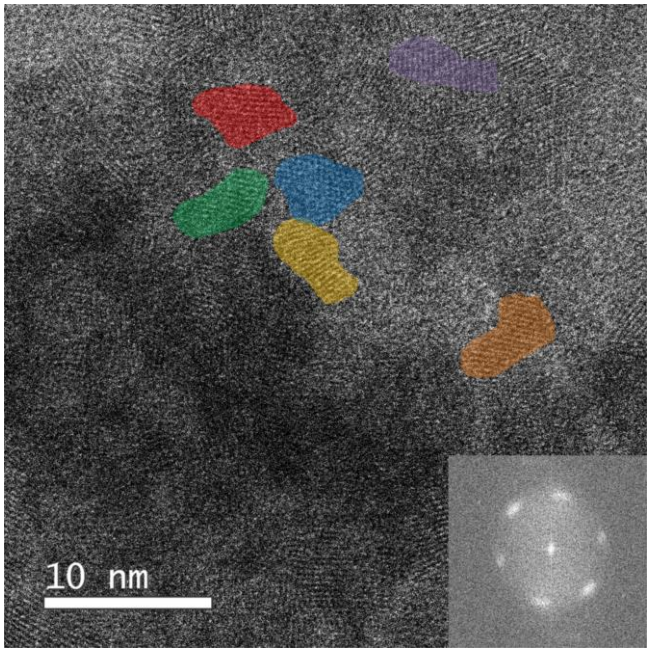

Figure 4.8. STEM image of the 400 ^{o}C MoS_2 synthesized from metallic Mo, with a few individual grains highlighted in color. The average grain size is on the order of 5 nm. The inset shows the FFT of the plane-view image.

The slope of the fits in Figure 4.7 can be used to determine T_0, which can then be related to localization length. The value for T_0 for each device is approximately 3 x 10^6 K, which is similar to previously reported T_0 values for TMDs[76, 219]. For a given T_0, $N(E_f)$ and ξ are inversely related, where a larger density of defect states at the Fermi level implies a smaller coherence length. The localization length of the films in literature were on the order of their respective grain size, so it is likely that the localization length for our 400 ^{o}C synthesized films is on the order of 5 nm. Additionally, all slopes are nearly identical. The high density of grain boundaries, indicated from the large Raman peak FWHMs, would explain the significant hopping conduction and short localization length. The devices were also measured under a sweeping gate bias in order to obtain a transfer curve, however the films exhibited minimal modulation of only a single order of magnitude, likely due to their

high defect density. Although the film exhibits defect mediated hopping conduction and minimal modulation under an applied gate bias, the PL response shown in Figure 4.4 and XPS spectra shown in Figure 4.5 suggest that the films are in the 2H semiconducting phase and do have the extended band structure necessary for direct band-to-band recombination. Further optimization of the synthesis process will likely yield higher quality films that can be more effectively modulated.

4.4 Effect of Atomic Structure and Stoichiometry on Electronic Performance

To provide better insight into the key structural and chemical variables leading to defects and their effect on electronic properties, the four-layer MoS_2 films synthesized at 400 ^oC were exposed to three different 800 ^oC annealing environments and were subsequently characterized. High temperature anneals of low temperature synthesized films were performed in order to exaggerate changes in atomic structure and stoichiometry. To measure the impact of these two material parameters, four samples were prepared. One sample was held as a control and named "As Grown." A second sample was annealed at 800 ^oC under a 4 sccm H_2S plasma at 300 W, resulting in a pressure of 10^{-5} Torr. The plasma conditions are identical to those used during H_2S plasma synthesis. A third sample was annealed under an identical H_2S flow at 800 ^oC, without striking a plasma. The fourth and final sample was annealed at 800 ^oC in a vacuum of 10^{-8} Torr. All anneals were 1 hour in duration.

Figure 4.9 (a) shows the A_{1g} and E^1_{2g} FWHM values for the As Grown, H_2S Plasma, H_2S, and vacuum anneals. The FWHM values of the two peaks for geological bulk crystals

are included as dashed lines for reference, which correspond to well-ordered films. Error bars for each data point are smaller than the data point itself.

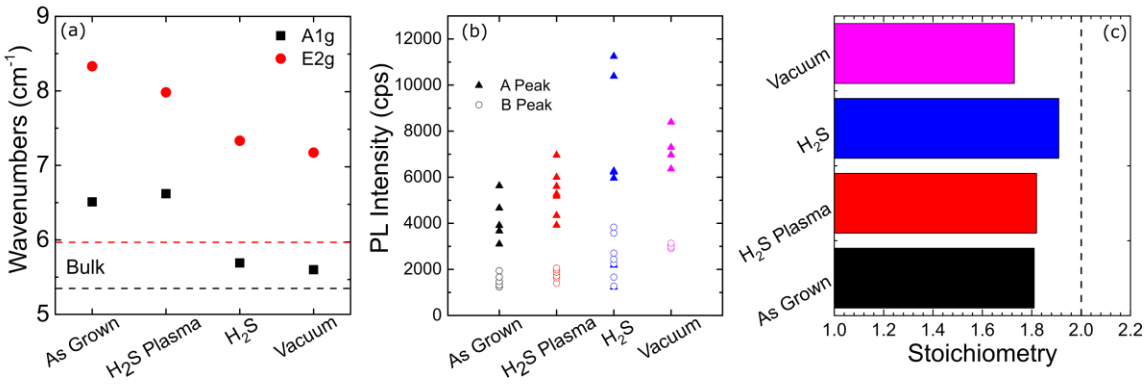

Figure 4.9. Raman peak FWHMs (a), PL A (solid triangles) and B (hollow circles) peak intensities in counts per second (b), and stoichiometries calculated from XPS (c) for as synthesized MoS_2, MoS_2 annealed under H_2S plasma, H_2S, and vacuum conditions. Bulk crystal Raman FWHMs are shown via the dashed lines in (a). Perfectly stoichiometric MoS_2 is represented by the dashed line in (c).

For both the A_{1g} and E^1_{2g} peaks, the vacuum anneal results in peak widths closest to high quality bulk values. Noticeably, the A_{1g} peak, which represents out-of-plane phonon nodes[215, 226], approaches the bulk value for both H_2S and vacuum anneals. This suggests that any perturbations in the layer-layer interaction of the four-layer film are resolved through annealing. The $E1+_{2g}$ peak corresponds to in-plane phonon nodes[215, 226]. For the case of the E^1_{2g} peak, all anneals result in a smaller FWHM, again with the vacuum anneal resulting in the smallest value. The FWHM of the E^1_{2g} after vacuum annealing is still approximately a full wavenumber away from the bulk value, indicating that the in-plane vibrations still suffer from inhomogeneity in the film. These results suggest that anneals are effective at reordering the atomic structure of MoS_2 and are more effective at normalizing the interlayer interactions than reducing perturbations in the intralayer

interactions. Vacuum annealing appears to be the most effective in reordering atomic structure.

A and B exciton PL peak intensities from spectra taken at various points on each sample are plotted in Figure 4.9 (b). H_2S plasma annealing results in a higher average PL signal intensity, followed by H_2S annealing and vacuum annealing. The increase in signal intensity can be associated with a more uniform electronic structure within the film. The large variance of peak intensities within each sample indicate that there is still significant electronic inhomogeneity across the film. Even so, the average intensity increase indicates that the anneals, specifically the H_2S and vacuum anneals, significantly improve the quality of the MoS_2. The suggested improved electronic structure observed from the PL spectra for each anneal condition is consistent with the trend observed in the Raman data shown in Figure 4.9 (a).

Stoichiometry for each annealed sample, calculated from XPS peak fits in the manner discussed above, is plotted in Figure 4.9 (c). The dashed line is located at the perfectly stoichiometric S:Mo ratio of 2:1. The H_2S plasma anneal does not appear to significantly influence sulfur incorporation, compared to the As Grown sample's sulfur percentage. However, annealing in H_2S does yield a 5% increase in sulfur concentration, resulting in the stoichiometry increasing from $MoS_{1.81}$ to $MoS_{1.91}$. Conversely, the vacuum anneal lowers the film's stoichiometry from $MoS_{1.81}$ to $MoS_{1.73}$. This is likely due to the low S partial pressure during the vacuum anneal. In this case, S is stripped from the film to balance S concentration in the film and surrounding environment. When some form of S is present in the annealing environment (either as H_2S plasma or H_2S), the partial pressure of

S in the annealing atmosphere is high enough such that the equilibrium reaction does not remove S from the film.

The combination of these physical characterization results shows that H_2S annealing yields both an improved atomic and electronic structure while maintaining a high stoichiometry. Although vacuum annealing yields sharper Raman peaks and stronger PL intensity, the difference in stoichiometry ($MoS_{1.91}$ versus $MoS_{1.73}$) indicates that some form of S partial pressure is required to maintain a highly stoichiometric film. Interestingly, the results suggest that H_2S is a more appropriate annealing environment than H_2S plasma. We previously showed that H_2S plasma is required for sulfurization of either Mo or MoO_x when only the stage is heated. However, these results indicate that while H_2S plasma is required for sulfurization, the plasma is less effective as an annealing environment.

One hypothesis to explain this relationship is that the plasma, although required to provide energy for the sulfurization reaction, does damage the MoS_2 film. Plasmas are commonly used as dry etchants for TMD materials, and in the case of MoS_2, an O_2 plasma can be used to induce defects into the film[213]. It would therefore be expected that a semidirect plasma would cause some degradation of the film. In this case, the ionized S radicals from the H_2S plasma have enough energy to incorporate into the film during synthesis; however, once the initial Mo film has been sulfurized into MoS_2, providing a S partial pressure via H_2S is sufficient for annealing out defects within the MoS_2 and filling individual vacant S atomic sites. We predict that a MoS_2 film annealed with H_2S plasma does undergo similar annealing effects but has a competing degradation mechanism due to the high energy ions bombarding the surface of the MoS_2.

To correlate physical characterization with electronic performance, two-terminal devices were fabricated from each of the four annealing samples. Devices were measured across the same range of temperatures from 100 to 340 K. Conductivities were extracted and plotted in Figure 4.10. Similar to Figure 4.7, each sample's conductivities can be fitted suing a VRH model, indicated by the linear fit overlaid on each dataset.

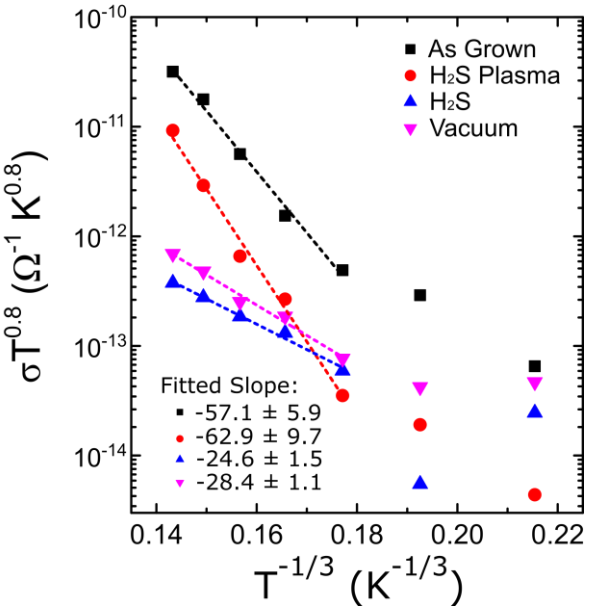

Figure 4.10. Temperature dependent conductivities extracted from devices fabricated using as grown, H_2S plasma annealed, H_2S annealed, and vacuum annealed MoS_2. The slopes of the linear fits are shown in the bottom left.

Two important pieces of information can be obtained from Figure 4.10. First, the conductivity at a given temperature is significantly lower for the H_2S and vacuum annealed films when compared to the As Grown and H_2S plasma annealed films. Additionally, the slope of the fitted trend line, which indicates the strength of the temperature dependence and is correlated to localization length, increases for the H_2S plasma annealed sample, but decreases significantly for the H_2S and vacuum annealed samples. This decrease in slope

indicates that the H_2S and vacuum annealed samples have a much weaker temperature dependence on conductivity due to the suppression of VRH conduction.

To explain this combination of phenomena, the total conductivity of a MoS_2 film can be thought of as two conductive pathways in parallel: an "intrinsic" conductivity relating to how efficiently carriers can flow through the film, and a hopping conduction conductivity which is determined by the localization length. In the As-Grown sample, the conductivity is relatively large, and its temperature dependence is strong. A large hopping conduction likely dominates the electronic transport through the film. This implies that the localization length is small. The H_2S plasma annealed sample has slightly lower conductivity but a steeper slope, indicating that the localization length is smaller, despite an overall conductivity decrease. In the case of the H_2S annealed and vacuum annealed samples, total conductivity is much lower, and the temperature dependence has weakened significantly, indicated by the shallower slopes. We hypothesize that the atomic structure of these samples has been reordered enough to significantly increase the localization length, which would severely mitigate hopping conduction. If the intrinsic conduction in each sample is low, the decrease in total conduction through each anneal would be explained by the reduction of hopping conduction. When hopping conduction is eliminated, the low intrinsic conductivity dominates, resulting in a lower total conductivity.

These electrical results agree with the physical characterization shown in Figure 4.9. The H_2S plasma annealed sample shows only slight improvements via physical characterization, and does not significantly improve the electrical performance of the film. However, the H_2S and vacuum anneals show much more improvement in Raman peak width and PL signal intensity, as well as significant reduction of hopping conduction. In

fact, H_2S annealing shows the lowest overall conductivity, as well as the smallest temperature dependence.

An interesting conclusion can be drawn by comparing the physical characterization data shown in Figure 4.9 with the conductivity data shown in Figure 4.10 for the vacuum annealed sample. The vacuum annealed sample exhibits much sharper Raman peaks and stronger PL peak intensities than the as grown sample, indicating that its structure has improved and the average domain size has increased. Although the stoichiometry has been significantly reduced, the conductivity data indicates that the VRH conduction has been strongly mitigated. This result suggests that improving atomic structure has more of an effect on electronic performance than stoichiometry. Moreover, the vacuum annealed sample exhibits similar Raman and PL spectra as the H_2S annealed sample, indicating that they are structurally similar. Additionally, the two samples display similar conductivity behavior. However, the difference in stoichiometry is fairly large, with the vacuum annealed sample having 10% less S than the H_2S annealed sample. This further supports the assertion that stoichiometry (specifically the number of S vacancies) is less critical compared to atomic structure and grain size in obtaining high electrical quality films.

4.5 Conclusions

In these experiments, the sulfurization mechanism of Mo containing films was investigated. A series of synthesis conditions were employed and the resulting MoS_2 films were characterized using Raman and XPS. Nearly stoichiometric MoS_2 was synthesized at 400 ^oC using the thin film reaction synthesis method. Initial oxidized MoO_x films were

shown to be more reactive, but metallic Mo films yielded MoS_2 with better atomic structure. H_2S plasma is required for sulfurization when only the stage is heated, because the surrounding atmosphere does not provide the requisite energy to facilitate the sulfurization reaction.

To improve film quality, synthesis was segmented into the repeated cycles of Mo deposition and S exposure. Excellent thickness control is demonstrated via cyclic synthesis, where four and three-layer films were synthesized and characterized to demonstrate high homogeneity. Additionally, MoS_2 synthesized in a cyclic process was found to have sharper Raman peaks, more intense PL, and higher stoichiometry than films synthesized in a single cycle. Metallic Mo and oxidized MoO_x initial films were synthesized using a cyclic process, whereupon physical characterization again indicated that metallic Mo initial films result in better structured, higher quality resulting MoS_2. Two terminal devices were fabricated from metallic Mo synthesized samples, and temperature dependent conductivities were measured, which suggested significant VRH, likely due to a high defect density and small grain sizes within the film.

Three different annealing conditions were investigated to better understand the effects atomic structure and stoichiometry have on electronic behavior, as well as provide insight on the S environment's effect on the thin film reaction. Physical characterization showed that H_2S plasma is not as effective as an annealing environment compared to H_2S or vacuum environments. Conversely, vacuum annealing resulted in the best atomic and electronic structure, but at the cost of significantly lower stoichiometry. Temperature dependent conductivities measured for each anneal condition corroborate the physical characterization results, where H_2S annealing and vacuum annealing result in better

electronic performance, with H_2S annealed samples exhibiting the highest electrical performance. Stoichiometry was shown to have a significantly smaller effect on hopping conduction than atomic structure and grain size.

This work demonstrates that the chemical state of the initial transition metal film (i.e., Mo versus MoO_x) plays an important role in thin film reaction synthesis of TMDs. Segmenting synthesis into the repeated cycles can be used to leverage more control over thickness uniformity as well as resulting film quality. Furthermore, H_2S plasma is required to provide energy for the reaction to synthesize the film at low temperature, but an as synthesized film can be degraded by further exposure to H_2S plasma. Moreover, stoichiometry was shown to have a significantly lower impact on the electrical behavior than atomic structure. In their current state, these materials are well suited for hydrogen evolution energy-based applications[227-228].

CHAPTER 5. LOW TEMPERATURE SYNTHESIS OF MOS_2 ON GOLD

One significant benefit of achieving low-temperature MoS_2 synthesis is that MoS_2 films can be synthesized on substrates that cannot withstand conventional synthesis temperatures. As such, MoS_2 can be synthesized directly onto substrates, such as plastics or metals, that otherwise would require transfer steps to yield MoS_2 placement. This is especially relevant in the case of layer-by-layer synthesis of vertical heterostructures, as synthesizing MoS_2 directly onto a contact metal is required. Because gold is one of the more commonly used contact metals in microelectronics and 2D materials research, this chapter will focus on synthesizing MoS_2 onto gold substrates and fabricating devices without any transfer steps.

5.1 Optimization of MoS_2 Synthesis on Gold

To explore MoS_2 synthesis on gold, samples were prepared for synthesis by e-beam evaporating 100 nm of gold onto 300 nm SiO_2/Si substrates. The substrates were cleaned using a standard acetone/isopropyl alcohol solvent clean, then loaded into the MBE chamber.

Synthesis was performed using the cyclic process discussed in CHAPTER 4.3. The temperature of the substrate was raised to 400 ^oC, and a 15-minute H_2S plasma pre-anneal was performed to further clean the sample surface. Once H_2S plasma annealed, three Mo

sputter/H_2S plasma soak cycles were performed in an attempt to yield 3-layer MoS_2. At the conclusion of the final sputter/soak cycle, the sample is cooled to 200 ^oC under vacuum, then moved to the load lock and cooled to room temperature under nitrogen.

The Raman response of the initial attempt at MoS_2 synthesis on gold is shown in Figure 5.1. The two characteristic phonon peaks are visible at ~405 cm^{-1} for the A_{1g} and ~380 for the E^1_{2g}, indicating that some MoS_2 exists in its characteristic hexagonal structure. However, the signal-to-noise ratio of the spectrum is extremely small, where the intensity of both peaks is barely above the background noise. Although metal substrates do provide a significantly larger Raman background signal and reduce the signal-to-noise ratio than insulating substrates, the resulting MoS_2 signal is significantly lower than other reported Raman spectra of MoS_2 on gold[229]. Therefore, MoS_2 film corresponding to the Raman spectrum in Figure 5.1 is likely of rather low quality, and as such the synthesis process requires optimization for synthesis on gold.

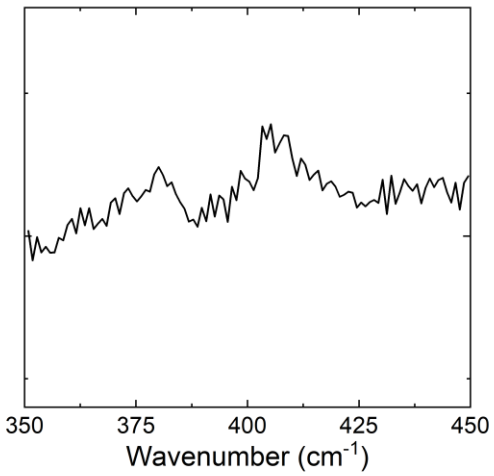

Figure 5.1. Raman response of a 3-cycle 400 ^oC metallic-Mo MoS2 synthesis process on a gold substrate. The y-axis is shown in arbitrary units. Faint A_{1g} and E^1_{2g} peaks can be seen at 405 and 380 cm^{-1}, respectively.

One possible explanation for the poor film quality is that sulfur reacts favorably with gold[230], yielding two competing sulfurization reactions between the gold substrate and deposited molybdenum films. Based on the results discussed in CHAPTER 4.2, oxidizing each deposited molybdenum layer to MoO_x should promote the sulfurization reaction, as MoO_x thermodynamically reacts more favorably with H_2S than metallic molybdenum. Therefore, the reactive sulfur species may be more likely to react with the oxidized molybdenum film as opposed to the gold substrate. In an attempt to improve the quality of MoS_2 films synthesized on gold, each molybdenum sputter step was moved to the load lock and oxidized, resulting in a synthesis process identical to the MoO_x initial film process discussed in CHAPTER 4.3.

Figure 5.2 (a) shows the Raman response for MoS_2 synthesized on gold using metallic and oxidized initial molybdenum films. The spectrum corresponding to the metallic molybdenum film is the same shown in Figure 5.1. It is immediately apparent that oxidized MoO_x initial films result in significantly higher quality resulting MoS_2 based on the improved signal-to-noise ratio of the spectrum. The peak separation of both spectra are similar, indicating that the resulting film thickness synthesized on gold is independent of initial molybdenum film composition, consistent with the results shown in Figure 4.6 (a) for MoS_2 synthesized on SiO_2 substrates. However, the Raman peak widths for MoS_2 synthesized on gold using MoO_x initial films are slightly larger than equivalent synthesized films on SiO_2 substrates, indicating that the quality of material synthesized on gold is slightly lower than material synthesized on SiO_2.

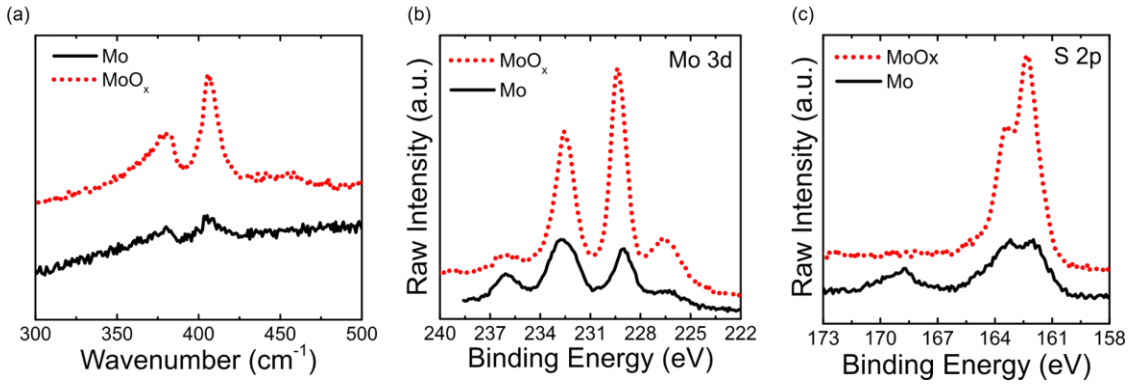

Figure 5.2. (a) Raman response of MoS_2 synthesized on gold substrates using metallic (Mo) and oxidized (MoO_x) initial molybdenum films. XPS Mo 3d (b) and S 2p (c) spectra for MoS_2 synthesized on gold using metallic (Mo) and oxidized (MoO_x) initial molybdenum films.

Figure 5.2 (b) shows the Mo 3d XPS spectra for MoS_2 synthesized on gold from the two different initial Mo films. The spectrum corresponding to MoS_2 synthesized from MoO_x initial films is dominated by the doublet of peaks at 230 and 232 eV corresponding to MoS_2. In addition, the spectrum exhibits only a small MoO_3 contribution at 236 eV, suggesting that the MoO_x sulfurized to near completion. Conversely, the spectrum corresponding to the metallic molybdenum initial film exhibits strong MoO_3 peak intensities at 233 and 236 eV. Moreover, the S 2s peak at 226 eV is not present in the metallic Mo spectrum, whereas it is not only present in the MoO_x initial film spectrum, but also exhibits a relative intensity that is consistent with MoS_2, as shown in **Error! Reference source not found.**.

The absence of sulfur in the metallic Mo initial film sample is corroborated by the S 2p XPS spectra shown in Figure 5.2 (c). The S 2p spectrum corresponding to the metallic molybdenyum initial film synthesis is weak in relative intensity compared to the C 1s

spectrum (not shown), indicating that there is not a large amount of sulfur present in the film. In contrast, the S 2p spectrum corresponding to the MoO_x initial film synthesis exhibits a strong signal corresponding to sulfur in the MoS_2 chemical state.

The stoichiometry of both MoS_2 films can also be calculated using the Mo 3d and S 2p spectra shown in Figure 5.2 (b,c). The calculated atomic ratio of MoS_2 synthesized on gold from metallic molybdenum initial films is only 1:1.02, indicating that the molybdenum initial film did not significantly react with the H_2S plasma. This is substantiated by the large MoO_3 percentage of the Mo 3d spectrum, where MoO_3 accounts for 51% of the molybdenum spectrum. In contrast, the atomic ratio between Mo and S in the MoO_x initial film sample is 1:1.94, indicating that the molybdenum reacted with the H_2S plasma nearly in full. These results confirm the hypothesis that oxidizing the initial molybdenum film will promote the sulfurization reaction, which is necessary for successfully MoS_2 synthesis on gold substrates.

5.2 Heterostructure Devices from MoS_2 Synthesized on Gold

Because MoS_2 synthesis on gold is now possible, transfer-free MoS_2 heterostructure can be fabricated by directly synthesizing MoS_2 onto bottom gold contacts. Because the metal/TMD/metal heterostructure is one of the simplest heterostructure architectures, in addition to their recent interest as memory select devices[21, 231], it is an obvious choice for initial heterostructure experimentation. In addition, the purely vertical structures contain no in-plane conduction, implying that the variable range hopping limitation discussed in CHAPTER 4 is not relevant to device operation, mitigating the

material constraint. Tri-layer MoS_2 was synthesized on gold substrates using the method discussed in CHAPTER 5.1, and top gold contacts were e-beam evaporated to yield a gold/MoS_2/gold device structure.

The device behavior of the gold/MoS_2/gold heterostructure devices is shown in Figure 5.3. Interestingly, the heterostructure devices exhibit resistive switching behavior, where the resistance of the device switches between a high and low resistance state as the source/drain voltage is swept. This switching behavior is highlighted by the arrows showing the voltage sweep direction, and the colors representing the high and low resistance state. The inset of Figure 5.3 shows the switching behavior on a linear scale, which breaks down the switching into four segments. As the source-drain bias is increased from 0 to positive biases, the device begins in a high resistance state (i). At around 0.5 V, the device begins to switch to a low resistance state and the current density increases before hitting the set compliance value of 0.08 A. When the bias is reduced, the current decreases linearly, but this time at a higher current density than during the positive voltage sweep (ii). Further decreasing the bias to negative values continues the linear I_d-V_d behavior, until approximately -0.75 V where the device switches back to a high resistance state (iii). Sweeping the bias back from -1 to 0 V brings the device state back to the initial point while maintaining the high resistance state (iv).

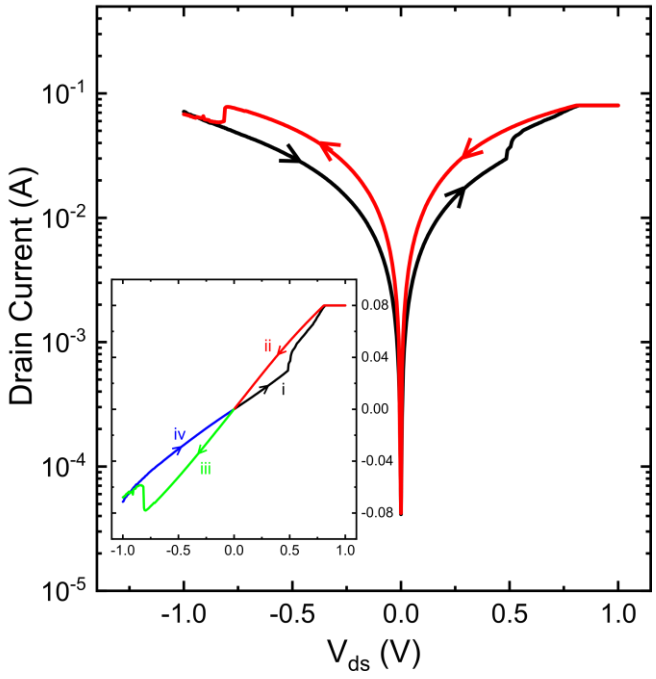

Figure 5.3. Device behavior of the gold/MoS_2/gold heterostructures. Switching is highlighted by the arrows and colors, which indicate the sweep direction and resistance state. The inset shows the same data on a linear scale, where the four switching regimes are indicated as (i) – (iv).

This switching behavior has traditionally been investigated in oxide materials systems[152], although recently switching has been observed in MoS_2 devices[95]. In this case, MoS_2 is synthesized using a traditional CVD process to yield individual flakes that do not fully coalesce into a single film. Although the grains do not fully coalesce, a number of grains do impinge on one another, resulting in a grain boundary between two single-crystal grains. Sangwan et al. then fabricated a device over this two-grain MoS_2 flake, where the source and drain contacts are located on opposite grains such that the grain boundary is located between them. When V_{ds} is swept, the resistivity through the film switches due to the motion of the grain boundary, which is confirmed through AFM[95]. In addition, the

resistivity of the device can also be modulated by an applied back gate, as the device architecture is the same as a standard FET.

Although the switching demonstrated by Sangwan et al.[95] and shown in Figure 5.3 are both observed in MoS_2 systems, it is likely that the mechanisms that dictate the switching behavior are different. The switching observed by Sangwan et al. is based on lateral grain motion in the direction of the applied bias. However, because the heterostructure device shown in Figure 5.3 operates based on out-of-plane carrier conduction, it is unlikely that applying a bias across the device will physically alter the lateral position of the grain boundaries. Reports in literature have shown filamentary switching in hBN systems, where metal ions diffusion through hBN interlayers to form a volatile low-resistance filament before diffusing back out of the interlayer[232]. It is possible that the switching behavior observed in Figure 5.3 is due to metal filament formation, although the resistance state of the gold/MoS_2/gold heterostructure appears to be non-volatile, as the resistance state is stored for more than 24 hours, which is in contrast to the observed behavior in the hBN filamentary systems. As such, further investigation is necessary to determine the cause for the switching behavior. Nevertheless, although the switching window of the devices shown in Figure 5.3 is small, the switching window is comparable to the devices demonstrated by Sangwan et al.[95] despite the likely difference in switching mechanism.

While the gold/MoS_2/gold heterostructures do demonstrate switching behavior, they are ohmic in nature. This device characteristic indicates that an insulating interlayer is needed in order to induce tunneling across the structures. Therefore, to induce tunneling behavior in the transfer-free, directly synthesized low-temperature MoS_2 devices, tunnel

heterojunctions were fabricated using a high-k interlayer as a tunnel barrier. Tri-layer MoS_2 was again synthesized directly onto gold substrates using the previously discussed method, after which 2.78 nm of Al_2O_3 or 2.71 nm of HfO_2 were ALD deposited onto the bottom layer MoS_2. After the high-k interlayer was deposited, tri-layer MoS_2 was synthesized directly onto the dielectric and was capped with a top gold contact deposited via e-beam evaporation. A resulting vertical structure of gold/MoS_2/interlayer/MoS_2/gold is consequently achieved, notably without requiring any transfer steps, implying that each interface is pristine.

The device I_d-V_d behavior of the Al_2O_3 interlayer device is shown in **Error! Reference source not found.** (a). A clean non-linearity is observed, indicating that the device is non-ohmic and that the device characteristics are dictated by tunneling across the dielectric interface. **Error! Reference source not found.** (b) re-plots the behavior in a FN plot, which shows the voltage threshold for the transition between direct tunneling (DT) and FN tunneling. In addition, (b) shows the evolution of the band structure from direct tunneling to FN tunneling. The FN tunneling threshold voltage is extracted from the minimum point on the FN plot, which is then shown in (a) as dotted red lines. HfO_2 interlayer structures exhibit similar behavior (not shown), and will be discussed in more detail later.

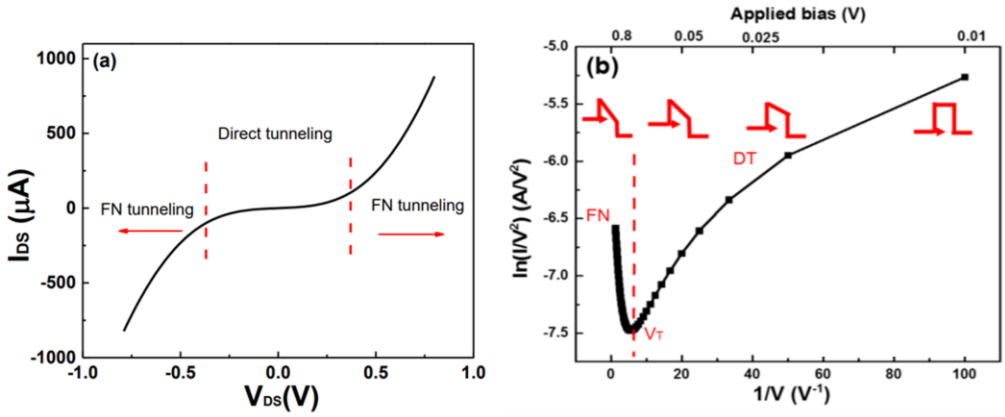

Figure 5.4. Device characteristics for an Al_2O_3 interlayer MoS_2 tunnel junction. (a) shows the device behavior in a normal scale, highlighting the different tunneling regimes occurring at different voltages. (b) re-plots the device data from (a) in a FN plot, and shows the band structure change leading to FN tunneling with increasing bias.

Because the heterostructures are symmetric, they theoretically are a plausible architecture for NDR tunneling applications. However, it is apparent from **Error! Reference source not found.** that the devices do not exhibit any NDR behavior. The lack of NDR behavior is likely due to fact that the material quality is relatively low, where disorder induces inhomogeneity in the electronic structure of the films and mitigates any NDR effects[22]. As such, further electrical characterization of these heterostructures as-fabricated likely will not yield any additional information. However, these devices will be discussed in more detail in CHAPTER 6.

5.3 Conclusions

In this chapter, low-temperature synthesis of MoS_2 on gold substrates was successfully achieved. In contrast to the results discussed in **Error! Reference source not**

found., where metallic molybdenum initial films yield higher quality resulting MoS_2, thin film reaction synthesis of MoS_2 on gold substrates requires oxidizing each deposited molybdenum film to MoO_x prior to sulfurization. Because sulfur reacts with gold much more favorably than with SiO_2, the sulfur-gold interaction competes with the sulfur-molybdenum interaction, preventing complete sulfurization of metallic molybdenum films. By oxidizing the molybdenum film, the sulfur-MoO_x interaction thermodynamics improve the favorability of the sulfurization reaction, resulting in successful MoS_2 synthesis. However, MoS_2 films synthesized on gold substrates still exhibit lower quality than equivalent synthesis on SiO_2 substrates, indicating that further optimization is required for synthesis on gold.

Two-terminal vertical heterostructures were fabricated from MoS_2 synthesized directly onto gold without requiring any transfer steps. Gold/few-layer-MoS_2/gold heterostructures displayed ohmic behavior, and exhibited memristive non-volatile switching. Although the switching window was small, the behavior mirrored switching characteristics in other MoS_2 device systems[95]. Placing a high-k dielectric interlayer between tri-layer MoS_2 films induced tunneling behavior, yielding symmetric tunnel junctions. NDR was not observed, suggesting that the film quality is too poor to exhibit the well-defined homogenous electronic structure needed for resonant tunneling, indicating further optimization of low-temperature synthesis on gold is required. Nevertheless, these results demonstrate that directly synthesizing MoS_2 onto metallic substrates can be utilized to fabricate vertical heterostructures without requiring transfer steps.

CHAPTER 6. RADIATION EFFECTS ON 2D VERTICAL HETEROSTRUCTURES

In recent years a number of studies have explored the radiation hardness of 2D materials for potential space systems[172, 174-175, 185, 189, 191, 233]. In particular, the surrounding environment of 2D materials has been demonstrated to strongly influence the electronic properties of the 2D film[234-235], and therefore can impact the radiation response of a 2D device. As such, an understanding how the intralayer interactions in 2D heterostructures impact radiation response is necessary. In this chapter, the radiation response of graphene and MoS_2 heterostructure devices is explored, utilizing low-frequency noise and electronic characterization in conjunction with atomistic modelling to understand what defects are generated when exposed to different forms of radiation, and how those defects influence device behavior.

The work discussed in this chapter was performed in close collaboration with Pan Wang, Dr. Andrew O'Hara, Dr. Daniel Fleetwood, and Dr. Sokrates Pantelides, all of whom are located at Vanderbilt university. My involvement in the work focused on device fabrication and initial characterization of the passivated graphene FETs and MoS_2 vertical tunnel junctions. Pan and Dr. Fleetwood were primarily involved in the irradiation and post-irradiation device characterization of the samples, while Dr. O'Hara and Dr. Pantelides contributed valuable atomistic modeling and DFT calculations to yield insight on defect energies and densities that arise due to radiation exposure.

6.1 Radiation Response of Passivated Graphene FETs[1]

In this section, the role of overlayers in the radiation response of graphene FETs was studied. Graphene FET devices were fabricated onto a 300 nm SiO_2/Si substrate and cleaned using the techniques discussed in CHAPTER 2. Two different passivation materials were chosen to reside on top of the graphene devices: Al_2O_3 and hBN. Al_2O_3 was deposited using ALD, yielding two separate samples with 4 and 19 nm thick Al_2O_3 overlayers. 40 nm hBN was transferred on top of the graphene FETs using a standard wet transfer technique[15]. An additional set of devices was left unpassivated to act as a control group.

The graphene FETs were irradiated with 10 keV X-rays at a dose rate of 30 krad(SiO_2)/min at room temperature while grounding the source and drain contacts and applying a gate bias of +5, 0, or -5 V. Baking was performed in ambient conditions at temperatures up to 400 K.

When low-frequency noise is caused by random thermally activated processes with broad energy distributions relative to *kT*, the frequency and temperature dependences of the noise are correlated by the Dutta-Horn model, which can used to relate defect energy to temperature and frequency through the simple expression[236-237]

$$E_0 \approx -kTln(\omega\tau_0) \qquad \textbf{6.1}$$

[1] Adapted with permission from Wang, P.; Perini, C.; O'Hara, A.; Tuttle, B. R.; Zhang, E. X.; Gong, H.; Dong, L.; Liang, C.; Jiang, R.; Liao, W.; Fleetwood, D. M.; Schrimpf, R. D.; Vogel, E. M.; Pantelides, S. T., Radiation-Induced Charge Trapping and Low-Frequency Noise of Graphene Transistors. *IEEE Transactions on Nuclear Science* **2018**, *65* (1), 156-163.

where $\omega = 2(\pi)(f)$ and τ_o is the transport scattering time. For eq. 6.1 to successfully be used, the noise must be accurately described by the full Dutta-Horn model. Low-frequency ($1/f$) noise measurements were performed on the graphene FETs at temperatures ranging from 85 to 400 K. V_{ds} was held at 0.02 V, with a fixed gate bias of -20 V from the Dirac point, where the current is at a minimum. Figure 6.1 shows the noise frequency dependence of the graphene transistors with 19 nm Al_2O_3 compared to predicted values using the full Dutta-Horn model. The agreement between the measured and calculated dependences implied that 6.1 can be used to infer defect energies from $1/f$ noise measurements.

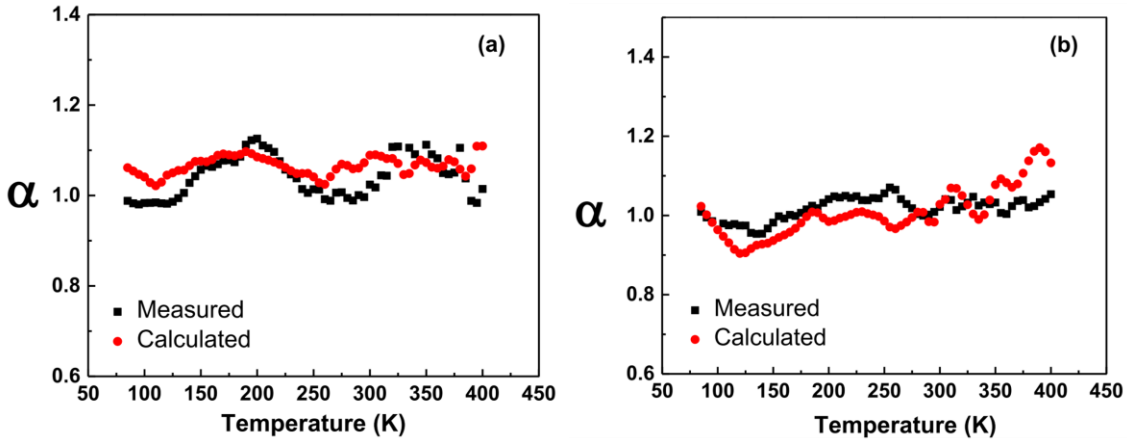

Figure 6.1. Comparison of measured and predicted noise frequency dependence of the 19 nm Al_2O_3 passivated graphene FETs before (a) and after (b) baking at 400 K for 24 hours.

To obtain a baseline for the performance of the graphene FETs, the effects of room-temperature aging and high-temperature baking were explored. Figure 6.2 shows I_d-V_g characteristics for a 19 nm Al_2O_3 passivated FET before and after it was baked at 400 K. After an initial 24 hour bake at 400 K, the CNP shifts approximately 10 V closer to 0, before shifting to its original value when stored in ambient conditions for 48 hours. A

subsequent bake successfully reduces the voltage value of the CNP, indicating that the regeneration process is reversible.

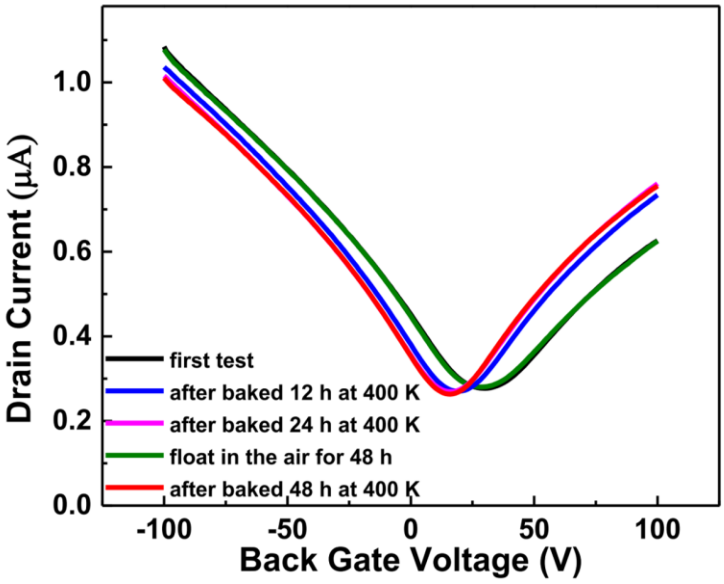

Figure 6.2. I_d-V_g curves with V_d = 0.02 V for a 19 nm Al_2O_3 passivated graphene FET before and after devices were baked at 400 K. The Dirac point shifts closer to 0 V when baked, and returns to its initial value when re-exposed to atmosphere.

To understand what defects and impurities may lead to the observed changes when exposed to baking, normalized 1/*f* noise measurements were taken on the 19 nm Al_2O_3 passivated FETs. Figure 6.3 shows the normalized low-frequency noise magnitude S_V *f*/*T* from 85 to 400 K for the different baking conditions. The top axis of Figure 6.3 represents the effective defect energy, obtained from eq. 6.1. For these defect-energy distribution estimates, the value of τ_o was set at 1 x 10^{-13} seconds for graphene[238]. The magnitude of the low-frequency noise decreases after the device is baked at 400 K, and returns to its original level after exposure to air for 49 hours. The reduction in trapped-negative charge density (CNP shift towards negative values) observed in Figure 6.2 and decrease in noise observed

in Figure 6.3 are likely due to outgassing and desorption of water-related mobile impurities in through the graphene passivation layer[239-240] and/or defect passivation due to hydrogen motion within the dielectric layers[241]. A noticeable peak is visible in Figure 6.3 at ~200-225 K, corresponding to effective defect energies of 0.4 to 0.5 eV (upper x-axis). The breadth of the effective defect energy distribution implies that there is not a single defect type that dominates the response; in contrast, various hydrogen/water complexes are likely responsible for the shifts in CNP and increased noise.

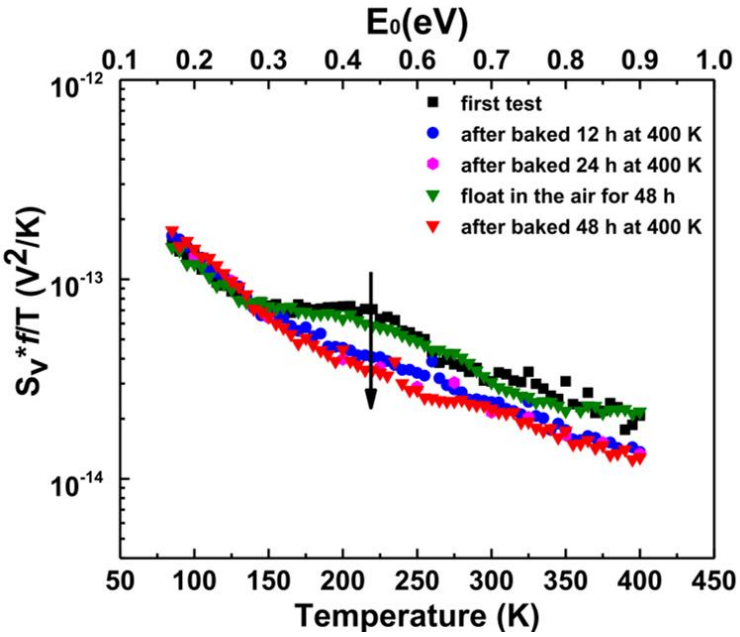

Figure 6.3. Normalized low-frequency noise magnitude S_V *f/T* at *f* = 10 Hz for the device shown in Figure 6.2 as a function of temperature for different baking conditions. Devices were measured at $V_g - V_{CNP}$ = -20 V.

Now that a baseline for the graphene FET performance is established, including defect and impurity effects that are intrinsic to the device structure, an understanding of the impact of radiation can be obtained. Figure 6.4 shows I_d-V_g characteristics as a function of dose rate at room temperature for graphene FETs passivated with 19 nm Al_2O_3. Prior to

irradiation, the FETs exhibit the characteristic electron conduction under positive gate biases and hole conduction at negative gate biases[36]. The deviation from 0 V of the CNP is primarily due to process-related charging at the graphene/insulator interfaces, which can be both positive or negative. For devices irradiated under a +5 and 0 V applied gate bias, the CNP shifts negatively (Figure 6.4 (a,b)), whereas the devices irradiated under a -5 V applied gate bias shifts positively (Figure 6.4 (c)).

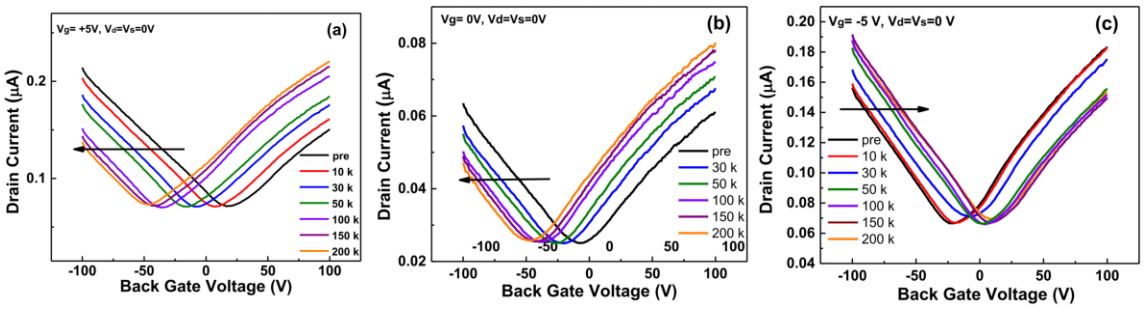

Figure 6.4. I_d-V_g curves as a function of total ionizing dose for graphene FETs passivated with 19 nm Al_2O_3 for applied gate biases of +5 (a), 0 (b), and -5 V (c). Devices were irradiated with 10 keV X-rays at a dose rate of 30 krad(SiO_2)/s with -5 V bias applied to the gate.

To this point, only the 19 nm Al_2O_3 passivated FETs have been discussed. The effects of the three different overlayers (4 nm Al_2O_3, 19 nm Al_2O_3, and 40 nm hBN) on each sample's resulting CNP shift is summarized in Figure 6.5 for devices irradiated under +5, 0, and -5 V applied gate biases. For all passivation layers, the CNP shift is strongly bias dependent; all CNP shifts are negative under +5 and 0 V applied biases during irradiation and positive under -5 V applied bias during irradiation. This response is qualitatively similar to previous studies on radiation response of graphene transistors[186, 188, 242]. Additionally, a significant effect of the passivation layer on the resulting radiation response is observed. The unpassivated graphene devices exhibit the smallest CNP shifts when

exposed to X-rays for all bias conditions. The radiation response of the unpassivated devices are similar to those observed by Zhang et al., and can be ascribed to radiation-induced electron trapping caused by oxygen atoms adsorbed on the graphene surface. Although the response of the hBN passivated devices are considerably larger in magnitude than the response reported by Zhang et al.[188], the amount of trapped charge is weaker than both Al_2O_3 passivated devices; when factoring in the relative thicknesses of the passivation layers, it is clear that the hBN exhibits the least amount of charge trapping. The devices passivated with 19 nm Al_2O_3 exhibits the largest CNP shifts, indicating that they experience the strongest doping due to a high density of trapped charge. Whereas dehydrogenation during baking is expected to primarily occur at the over-layer graphene interface, radiation induced charge trapping should occur at both interfaces above and below the graphene. The negative CNP shifts for +5 and 0 V biases are likely due to radiation-induced hole trapping in either the underlying SiO_2 or overlying Al_2O_3. Conversely, the positive shifts under -5 V biases are likely due to electron trapping that occurs at either interface.

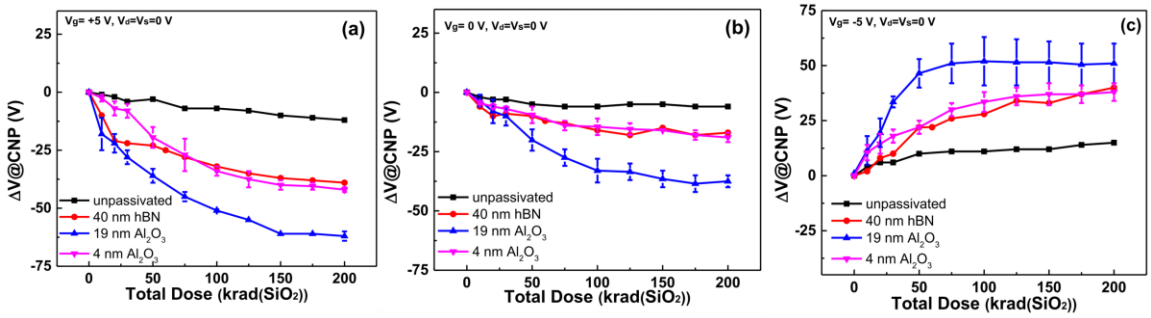

Figure 6.5. CNP shifts as a function of X-ray dose for devices irradiated under applied gate biases of +5 (a), 0 (b), and -5 (c) V. Error bars shows device to device variations on a given sample.

To learn the specific defect types and energies and are responsible for the Al_2O_3 devices observed behavior in Figure 6.5, 1/*f* noise measurements of each sample were performed. Figure 6.6 shows the low-frequency noise measurements for the 4 nm and 19 nm Al_2O_3 passivated graphene FETs, as well as an unpassivated control FET, as a function of temperature. For all devices, peaks at defect energies of ~0.4 and ~0.7 eV are observed after 100 krad(SiO_2) irradiation. The unpassivated devices shown in Figure 6.6 (c) exhibit an additional increase in noise magnitude at low temperatures. Of note, these noise peaks are not commonly observed when Si-based MOS devices are X-ray irradiated[236, 243], suggesting that the observed peaks correspond to defects associated specifically with graphene and its interfaces, as opposed to bulk SiO_2.

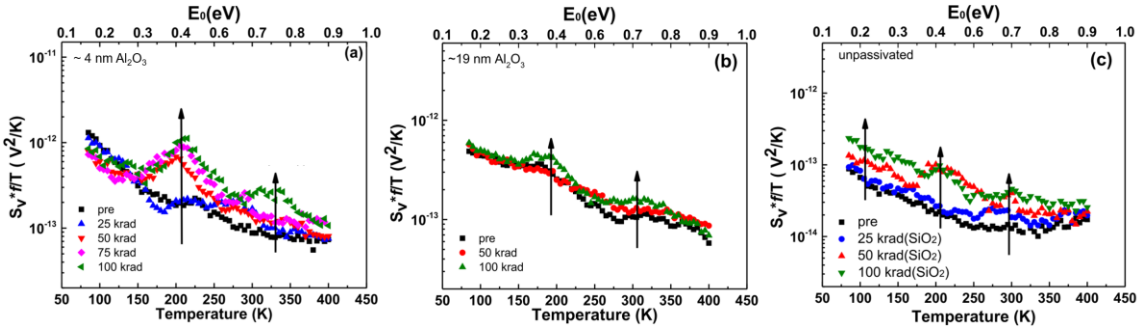

Figure 6.6. Normalized low-frequency noise from 85 to 400 K at f = 10 Hz under various irradiation doses under -5 V applied gate bias. Devices with 4 nm and 19 nm Al_2O_3 are shown in (a) and (b), respectively. (c) corresponds to an unpassivated device. Black arrows note the position of defect-induced peaks in the noise with increasing dose. Devices were biased at $V_g - V_{CNP}$ = -20 V during noise measurements.

DFT calculations were performed in order to associate specific defect types with the observed 0.4 and 0.7 eV defect energies[244]. In particular, defect calculations revealed that a dehydrogenated oxygen site in the dielectric adjacent to the graphene film generates defect levels at 0.3 and 0.7 eV into the density of states of the system, which is consistent

with the observed defect energies obtained from the noise measurements shown in Figure 6.6. The low temperature noise increase observed in the unpassivated device (Figure 6.6 (c)) likely results from trap sites induced by adsorbed atmospheric molecules on top of the graphene.

It is known that hydroxyl radicals bind with a broad distribution on energy levels that are sensitive to microstructure in alumina[245]. Additionally, DFT studies in the literature have shown that adsorbed water at the graphene/Al_2O_3 interface traps negative charge from the graphene layer[246]. The CNP shifts positively after baking, which corresponds to a reduction of OH^- ion density near the graphene/dielectric interfaces when exposed to high temperatures. Atmospheric exposure allows hydroxyls to return to that interface, restoring the doping density to the original value. Moreover, the DFT calculations performed by Wang et al.[244] suggest that the presence of depassivated oxygen and oxygen vacancies can contribute to CNP shifts when exposed to X-ray radiation. As such, it is likely that both oxygen and hydrogen/water related defects are important in determining the radiation response and low-frequency noise in graphene transistors.

6.2 Radiation Response of MoS_2 TFET Heterostructures[2]

The previous study on radiation effects on graphene FETs yielding valuable information concerning the oxide adjacent to the 2D film. However, the previously

[2] Adapted with permission from Wang, P.; Perini, C.; O'Hara, A.; Gong, H.; Wang, P.; Zhang, E. X.; McCurdy, M. W.; Fleetwood, D. M.; Schrimpf, R. D.; Pantelides, S. T.; Vogel, E. M, Total-ionizing-dose effects and proton-induced displacement damage on MoS_2-interlayer-MoS_2 tunneling junctions. *IEEE Transactions on Nuclear Science* **2018**, *66* (1), 420-427.

discussed radiation experiments focused on in-plane conduction of a heterostructure device, where the overlayers simply acted to passivate the 2D film from the environment. As such, the next logical step of investigating the radiation response to 2D heterostructures involves investigating heterostructure device architectures that operate on out-of-plane carrier conduction.

To facilitate the investigation of radiation effects on out-of-plane heterostructure devices, the radiation response of the MoS_2/interlayer/MoS_2 tunnel junctions discussed in CHAPTER 5 was investigated. Heterostructures were fabricated using low-temperature 400 ^oC synthesized MoS_2, where the interlayer consists of either Al_2O_3 or HfO_2. Notably, these structures require no transfer steps; the bottom layer $MoS2_2$ film are synthesized directly onto the bottom gold contacts, the interlayer dielectric is deposited using ALD, and the top layer MoS_2 is synthesized directly onto the dielectric interlayer. Al_2O_3 and HfO_2 were chosen for two reasons. First, the oxidation state of the metal is different for each dielectric. The previously discussed radiation studies on graphene FETs indicated that oxygen sites play a significant role in the radiation response of the device; the passivation state and vacancy concentration of oxygen in the dielectric significantly influences the behavior when exposed to ionizing radiation. Second, the work function of the two dielectrics is different, which should therefore yield different barrier heights at the MoS_2/insulator interface and therefore yield different tunneling behavior.

To fabricate the devices, 80 wells were etched into 300 nm SiO_2 using SF_6 plasma. Bottom gold contacts were e-beam evaporated into the wells, whereupon MoS_2 was directly synthesized onto the gold using the technique described in CHAPTER 5. 2.71 nm of HfO_2 and 2.78 nm of Al_2O_3 were deposited onto the bottom layer MoS_2 via ALD.

Afterwards, a subsequent top MoS_2 layer was directly synthesized onto the dielectric interlayer, and top gold contacts were deposited onto the top of the heterostructure using e-beam evaporation, yielding a total structure of Au/MoS_2/interlayer/MoS_2/Au. The resulting heterostructure is purely vertical, so that current flow tunnels between the MoS_2 layers predominantly out-of-plane.

X-ray irradiation effects were first explored on the vertical tunnel junctions. Both heterostructures were irradiated with 30.3 krad(SiO_2)/min X-rays at room temperature while biasing the drain contact at 0.3 V. Figure 6.7 (a,b) shows the I_d-V_d behavior as a function of X-ray dose for the Al_2O_3 and HfO_2 heterostructures, respectively. Markedly, no significant deviations in electrical behavior are observed with increasing dose for either sample for exposures up to 1 Mrad(SiO_2), suggesting that these heterostructures are stable and not significantly influenced by X-ray irradiation. This result is in significant contrast to the in-plane graphene FETs examined in the previous study.

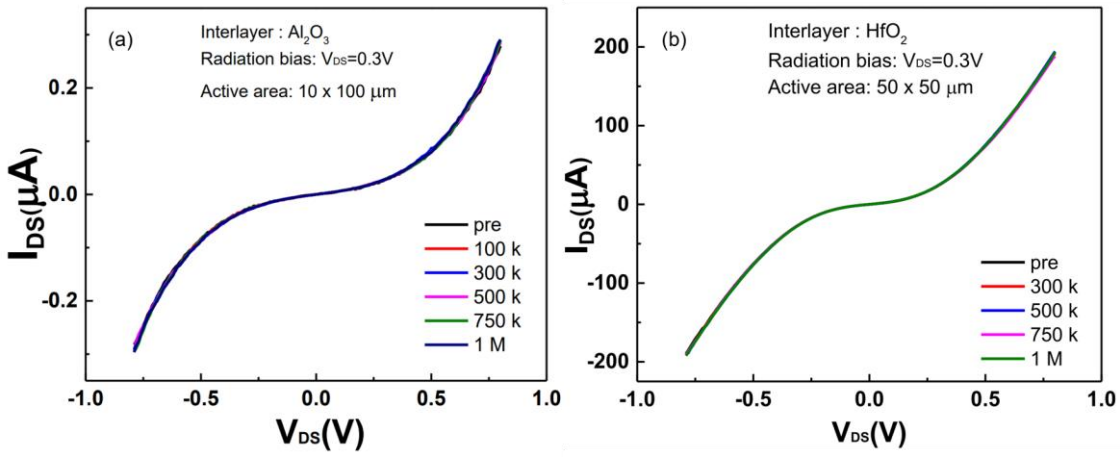

Figure 6.7. I_d-V_d curves as a function of X-ray total ionizing dose for MoS_2 tunnel junctions with interlayer dielectrics of Al_2O_3 (a) and HfO_2 (b). Devices were irradiated with 10 keV X-rays with 0.3 V bias applied to the drain during exposure.

As the MoS_2/insulator/MoS_2 vertical heterostructures are strongly resistant to X-ray irradiation, the next logical step is determining the tunnel junction's response to proton irradiation. The heterostructures were exposed to increasing fluences of protons, up to 10^{14} protons/cm^2. I_d-V_d device characteristics for each structure as a function of proton fluence are plotted in Figure 6.8. No significant changes in device behavior are observed for either structure for fluences up to 10^{13} protons/cm^2. Further increasing the proton fluence induces an increase in current for the Al_2O_3 interlayer devices (Figure 6.8 (a)), whereas the HfO_2 interlayer devices exhibit no noticeably change in device behavior with increasing fluence (Figure 6.8 (b)).

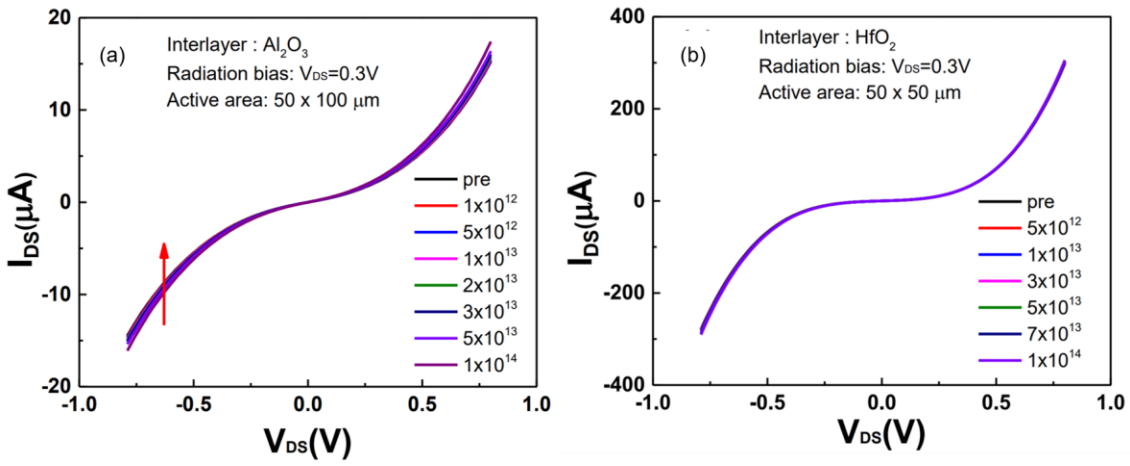

Figure 6.8. I_d-V_d response as a function of proton fluence for MoS_2 tunnel junctions with Al_2O_3 (a) and HfO_2 (b) interlayers. The HfO_2 devices exhibit a noticeably higher current density.

The device measurements shown in Figure 6.8 can be replotted in FN form, which yields information on the change in injection behavior with increasing proton fluence. Figure 6.9 plots the *I*-*V* data shown in Figure 6.8 in FN form. The inset of Figure 6.9 (a) shows the transition voltage between FN tunneling at high voltages (low 1/*V*) and direct

tunneling at low voltages (high 1/*V*) for the Al_2O_3 interlayer sample. A clear shift of the FN threshold voltage is observed for the Al_2O_3 interlayer sample, decreasing from 0.54 V to 0.48 V after receiving a proton fluence of $10^{14}/cm^2$. Conversely, the HfO_2 interlayer devices exhibited no change in FN threshold voltage. The fact that the Al_2O_3 devices exhibit a FN threshold voltage shift with increasing proton fluence while the HfO_2 interlayer devices do not strongly suggests that the changes in device behavior are defect related, and not due the indirect-to-direct band gap transition in MoS_2 structures irradiated with 100 keV protons observed by Foran el al[247].

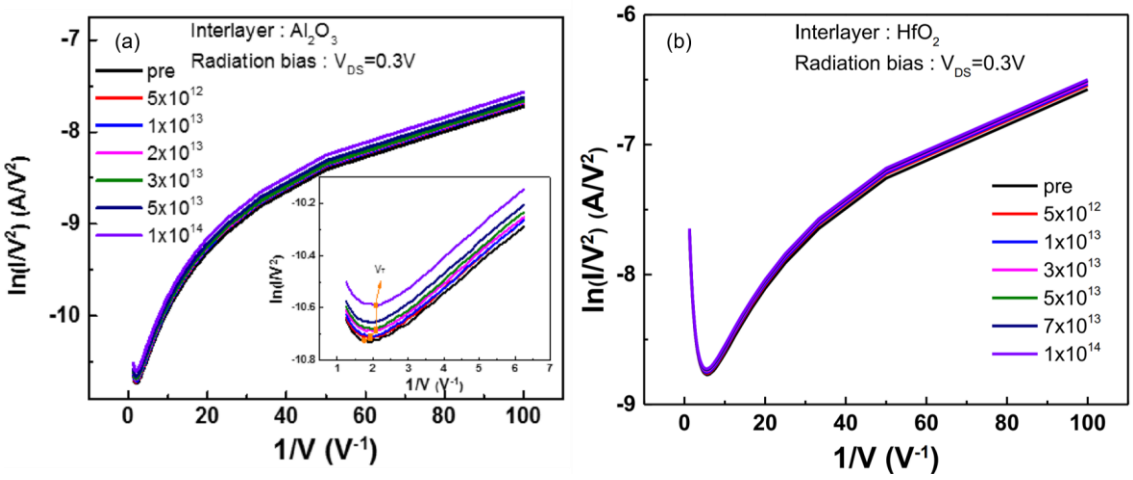

Figure 6.9. FN plots of the *I-V* data shown in Figure 6.8. The inset of (a) shows the evolution of the transition from direct tunneling to FN tunneling with increasing proton fluence.

The lack of X-ray radiation response in both heterostructures (Figure 6.7) suggests that ionizing-dose-induced depassivation of defect precursors plays little to no role in the radiation response of the heterostructure device's behavior. In contrast, the noticeable response to proton irradiation in the Al_2O_3 interlayer heterostructure, but not the HfO_2 interlayer heterostructure, suggests that physical displacement damage (such as vacancy

formation) in the Al_2O_3 may lead to trap-assisted tunneling. The displacement of light atoms (i.e. oxygen) may create defect states with energy levels aligning close to the conduction band of the MoS_2.

To understand the nature of the proton-induced defects, DFT calculations were performed using the VASP code[248-249]. The exchange-correlation functional was calculated using the Perdew, Burke, and Ernzerhof generalized gradient approximation[250] with a van der Waals interaction correction[251] and pseudopotentials[252]. A 550 eV plane-wave-cutoff energy was employed and a 2 x 2 x 1 k-point grid was used for Brillouin-zone integrations. Atomic positions were relaxed until all forces were less than 0.01 eV/Å.

Because the primary layer-dependent differences in the electronic structure of MoS_2 occur between one and two layers, the MoS_2 was represented as a bilayer for calculations. HfO_2 was modeled using the monoclinic phase, and the θ-Al_2O_3 phase was chosen due to its lower density and oxygen-bond coordination allows for a better comparison with amorphous gate oxides[253-254]. The oxides were 1 nm thick oriented along the [100] direction, and the lateral dimensions were chosen to minimize interfacial strain with the MoS_2. Both heterostructure models exhibit the expected type-I band alignment.

Oxygen vacancies in Al_2O_3 introduce two unique defect levels: a fully occupied level near the Al_2O_3 valence band and an empty level near the Al_2O_3 conduction band. These states are shown in Figure 6.10 (a) with respect to the MoS_2 and Al_2O_3 band structures. Neither of these states are near the MoS_2 conduction band, and therefore should not contribute to trap assisted tunneling. However, partial passivation of the oxygen vacancy by hydrogen causes significant shifts in the defect energy levels. These shifts can

be seen in Figure 6.10 (a) as the V_o + H states, which correspond to an unoccupied interfacial (I) and near interfacial (NI) which yield unoccupied states 0.24 eV above and 0.2 eV below the MoS_2 conduction band, respectively. Additionally, passivated oxygen vacancies in the bulk of the oxide, corresponding to the states labeled as B in Figure 6.10, yield an occupied state 0.05 eV below the MoS_2 conduction band. Sources of hydrogen to passivate these oxygen defects by diffusing through the interface include lower energy protons from irradiation and hydrogen captured during ALD. Aluminas have previously been shown to easily absorb hydrogen[255-256], and therefore partially passivated oxygen vacancies likely affect the increase in tunnel current after exposed to proton irradiation.

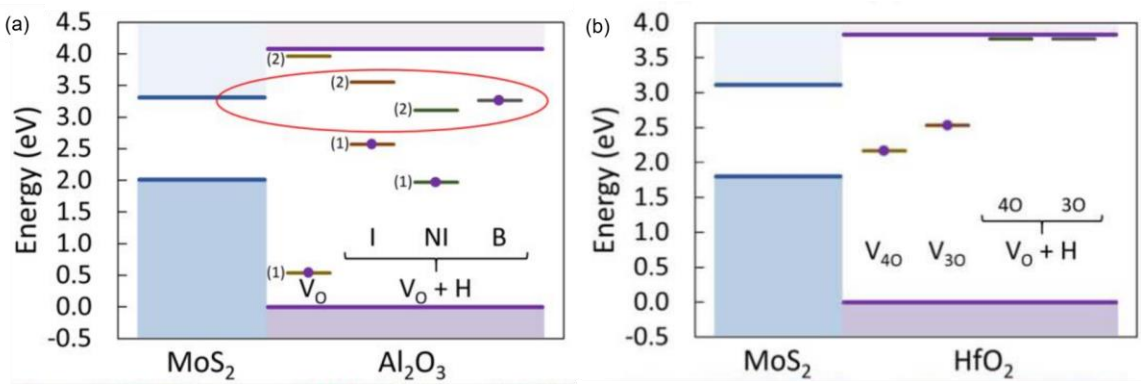

Figure 6.10. Modeled band alignment and defect energies for relevant defects at the MoS_2/Al_2O_3 (a) and MoS_2/HfO_2 (b) interfaces. The red oval in (a) highlights the defect levels most likely to contribute to trap assisted tunneling.

In the case of HfO_2, oxygen vacancies introduce a hole trap 0.58 or 0.94 eV below the MoS_2 conduction band for 3-fold and 4-fold coordinated vacancies, respectively. These defect levels can be seen in Figure 6.10 (b). When passivated, these defect energies move close to the HfO_2 conduction band. In both the passivated and unpassivated vacancy cases, no defect states align closely with the MoS_2 conduction band, and therefore these defect

states likely do not contribute to trap assisted tunneling in the tunnel junction heterostructures, which is consistent with the lack of irradiation response seen in Figure 6.8 (b).

6.3 Conclusions

Graphene FETs were fabricated and subsequently passivated with hBN and Al_2O_3. Current-voltage and low-frequency noise measurements provide insights into the energy distribution of defects in graphene transistors. Charge trapping at the graphene/insulator interfaces results in CNP shifts, positively for negative bias irradiation and negatively for positive bias irradiation. The noise of these devices is described well by the Dutta-Horn model, consistent with a wide range of other microelectronic material systems. Both hydrogen-related impurities and oxygen defect complexes lead to significant changes in device behavior, indicating their relevance in performance, reliability, and radiation response of graphene-based heterostructure devices. In particular, the 2D/insulator interface was found to significantly influence device performance.

Purely vertical MoS_2 heterostructures were fabricated to further explore the 2D/insulator interface. The MoS_2 heterostructures demonstrated resilience to X-ray irradiation, where little to no response was observed for doses up to 1 Mrad(SiO_2). When exposed to proton irradiation, Al_2O_3 interlayer devices exhibited a radiation response, where the FN tunnel current voltage threshold decreased with increasing proton fluence. Conversely, the HfO_2 interlayer structures did not exhibit any response to proton irradiation. DFT calculations reveal that passivated oxygen vacancies in Al_2O_3 lead to

defect states closely aligned with the MoS_2 conduction band, which likely contribute to trap assisted tunneling. No such defect states occur in HfO_2, where both passivated and unpassivated oxygen vacancies yield defect energies strongly misaligned with the MoS_2 conduction band, consistent with the lack of observed device response to proton irradiation for the HfO_2 interlayer structures.

In summary, this work explored the effect of X-ray and proton irradiation on 2D heterostructure devices. These results indicate the importance of the interface between the 2D material and surrounding dielectric. Various defect and impurity complexes can significantly influence device performance, and therefore understanding how surrounding layers impact 2D heterostructure device performance and reliability is of the utmost importance. Understanding the influence of these defects allows for engineering device architectures by choosing material systems that are resilient to defect effects.

CHAPTER 7. LOW TEMPERATURE SYNTHESIS OF SULFIDE HETEROSTRUCTURES

To this point, the majority of the heterostructures discussed in this work have utilized MoS_2 as the only 2D material in the structure. As stated previously, a significant benefit of 2D materials is the ability to stack arbitrary 2D layers onto one another. As such, adding a dissimilar 2D material is crucial to understand how defect effects influence 2D heterostructures with differing 2D layers. A significant amount of research has explored the MoS_2/WS_2 heterostructure system, notably for use in rectifying applications[61, 67, 73, 257]. Therefore, this chapter will explore low temperature synthesis of WS_2 and MoS_2/WS_2 heterostructures and their associated device behavior.

7.1 Low Temperature WS_2 Synthesis

In order to synthesized WS_2 films at 400 ^oC, the low temperature synthesis process for MoS_2 discussed in CHAPTER 4 was adapted for a tungsten process. The synthesis process was simply altered, where tungsten was exchanged for molybdenum during each sputter cycle. Because tungsten deposits more slowly than molybdenum, each sputter step was performed for 16 seconds to yield a tungsten monolayer as opposed to the 12 seconds used for molybdenum. All other process parameters for each synthesis cycle, including H_2S

plasma power and soak time, temperature, and chamber pressure, are identical to those used for MoS_2 synthesis in CHAPTER 4.

Figure 7.1 shows a representative Raman spectrum for a WS_2 film synthesized on SiO_2 using three synthesis cycles. The characteristic A_{1g} and E^1_{2g} WS_2 phonon nodes are visible at 417 cm^{-1} and 354 cm^{-1}, respectively. The resulting peak separation of 63 cm^{-1} agrees well with literature values observed in three layer WS_2 films[258]. This result further supports the previous finding of excellent thickness control via cyclic synthesis in our low temperature synthesis process.

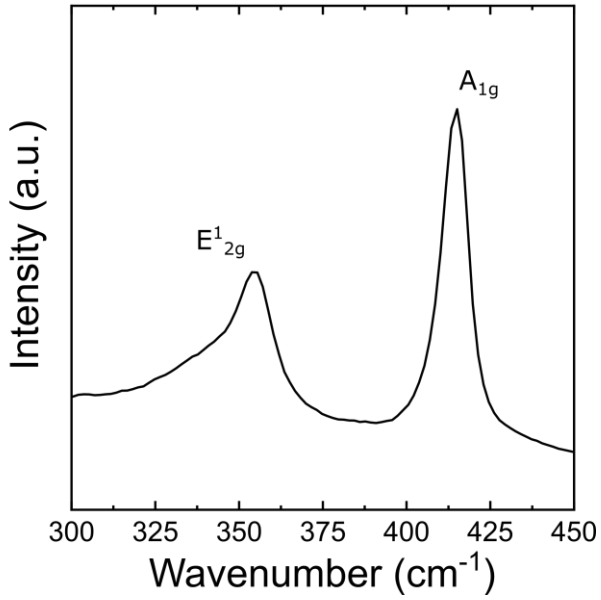

Figure 7.1. A representative Raman spectrum from a three cycle WS2 synthesized film. The A1g and E12g peaks are labeled. The y-axis shows Raman intensity in arbitrary units.

XPS measurements were performed on the tri-layer WS_2 films in order to determine their stoichiometry. The fitted XPS spectra for the W 4f and S 2p peaks are shown in Figure 7.2 (a) and (b), respectively. The same fitting method is used as described in CHAPTER

4, this time with tungsten specific parameters. The peak separation of the two W 4f doublets, corresponding to WS_2 and WO_3, is fixed at 2.1 eV, and the area ratio of the $4f^{7/2}$ to $4f^{5/2}$ is fixed at 4:3. The position of the two doublets relative to each other is unconstrained. The parameters of the W $5p^{3/2}$ are unconstrained. The S 2p spectrum was fit using the same parameters discussed in CHAPTER 4.

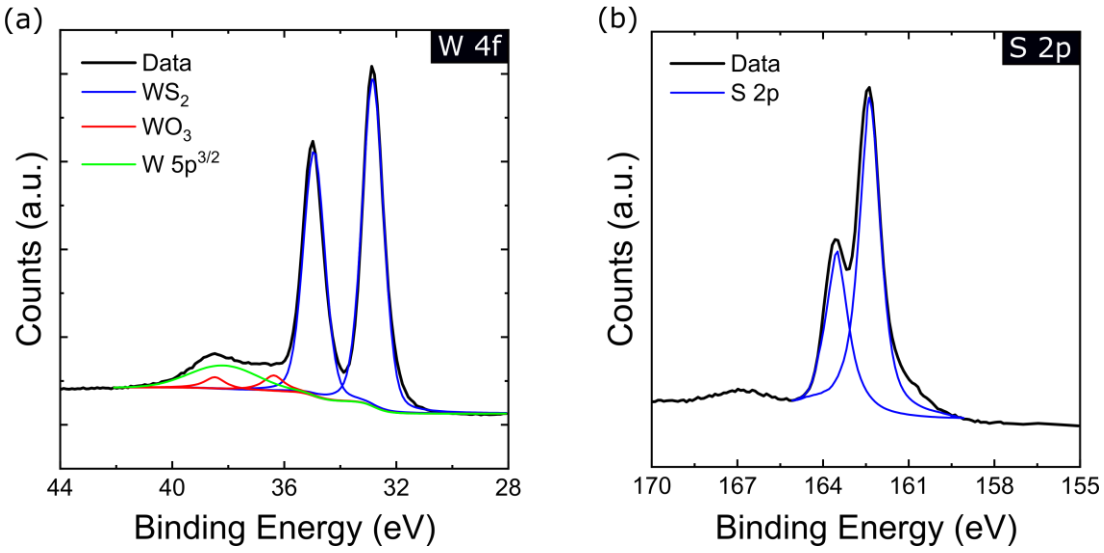

Figure 7.2. Fitted XPS spectra of the W 4f (a) and S 2p (b) spectra for the three-layer WS2 film synthesized at 400 oC. In (a), five peaks are used, corresponding to a WS2 W 4f doublet, a WO3 W 4f doublet, and a single W 5p3/2 peak. A single S 2p doublet is used to fit the spectrum in (b).

From the fitted XPS spectra shown in Figure 7.2, the stoichiometry of the film can be calculated using the same method as described earlier. By normalizing each element's peak areas to its respective sensitivity factor (2.75 for W and 0.54 for S)[216], the stoichiometry of the film can be determined to be $WS_{1.96}$. The stoichiometry is nearly at the ideal 2:1 ratio, again indicating that the low temperature synthesis procedure yields nearly stoichiometric material.

The Raman and XPS results shown in Figure 7.1 and Figure 7.2 indicate that exchanging the transition metal sputtering step from molybdenum to tungsten does not significantly influence the synthesis process. As such, it is likely that MoS_2 and WS_2 synthesis can be integrated to directly synthesize heterostructures without either material significantly influencing the synthesis of the other. These results suggest that low temperature heterostructure synthesis is feasible, and therefore should be investigated.

7.2 Heterostructure synthesis

The results presented in the previous section suggest that synthesizing MoS_2/WS_2 heterostructures at 400 ^oC using the previously discussed synthesis method is feasible. In order to test this hypothesis, two six cycle syntheses were performed on SiO_2 substrates to yield three-layer by three-layer MoS_2/WS_2 and WS_2/MoS_2 heterostructures, where the material listed first corresponds to the material synthesized first. The heterostructures were synthesized at 400 ^oC, using the same synthesis parameters discussed in the previous section and CHAPTER 4 for WS_2 and MoS_2, respectively.

Raman spectra for the as grown three-layer MoS_2, three-layer WS_2, and both six-layer heterostructures are shown in Figure 7.3 (a). From inspection, it is clear that characteristic phonon nodes for both MoS_2 and WS_2 are present in both heterostructure orientations, indicating successful heterostructure synthesis. Interestingly, the bottom material that was synthesized first exhibits a stronger Raman response that dominate the spectrum for both heterostructure orientations. In addition, the peak separations of the individual MoS_2 and WS_2 spectra are approximately one wavenumber smaller than the

corresponding peak separations of the MoS_2 and WS_2 peaks doublets in both heterostructure Raman spectra. This increase in peak separation for the heterostructure spectra indicates that the electronic structure of the individual materials behaves as if the individual materials are thicker than they actually are[259]. That is, the three-layer MoS_2 and WS_2 layers in the heterostructures behave closer to a bulk film as opposed to two independent three-layer films. This interaction is relevant for implications involving the material's band structure, as stated earlier[46]. Nevertheless, it is apparent that both individual materials exist independently in both heterostructure orientations.

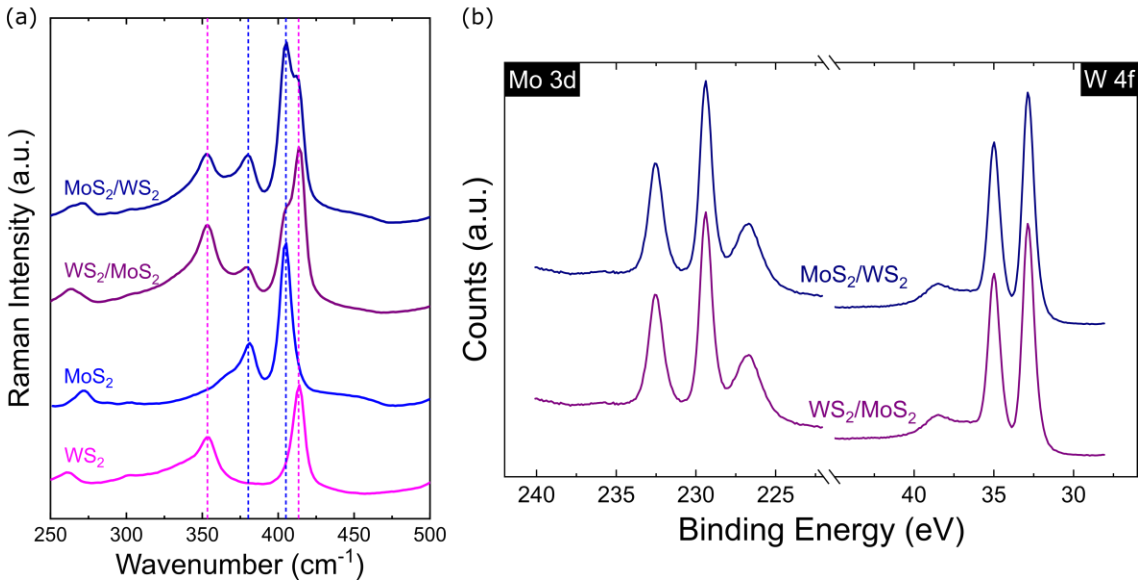

Figure 7.3. (a) Raman spectra of three-layer WS_2, three-layer MoS_2, and both three-by-three-layer heterostructures. The peak positions the MoS_2 and WS_2 peak doublets are noted by the blue and pink dashed lines, respectively. The Mo 3d and W 4f XPS spectra of both heterostructures is shown in (b).

The Mo 3d and W 4f XPS spectra for both heterostructure orientations are shown in Figure 7.3 (b). From inspection, it is clear that the chemical composition of both layers is independent of heterostructure orientation (i.e. synthesis order). The Mo 3d spectra for

both heterostructure orientations exhibit minimal MoO_3 contributions, evidenced by the lack of significant peak signal at 236 eV. Similarly, the satellite peak at 38 eV for both W 4f spectra is primarily composed from the W $5p^{3/2}$ and does not exhibit significant WO_3 contributions. In addition, the stoichiometry of the entire heterostructure can be determined by normalizing the peak area of the Mo 3d, W 4f, and S 2p (not shown) spectra. Because the peak positions of the MoS_2 and WS_2 S 2p doublets are essentially degenerate, it is not viable to calculate each material's individual stoichiometry. Instead, a "total" stoichiometry of the heterostructure can be obtained, by normalizing the S 2p doublet area to the sum of the Mo 3d and W 4f doublet's areas. Doing so yields a "total" stoichiometry of the MoS_2/WS_2 heterostructure of 1:1.97, and a "total" stoichiometry of the WS_2/MoS_2 heterostructure of 1:1.98. While it is possible that the individual material's stoichiometries differ, the fact that both heterostructure orientations yield similar nearly stoichiometric atomic ratios, in addition to the minimal transition metal oxide signal for both molybdenum and tungsten in both heterostructure orientation, suggests that the "total" heterostructure stoichiometry mirrors each material's individual stoichiometry.

To further explore the band structure of the heterostructures, PL measurements were performed on the tri-layer MoS_2 and WS_2 as well as both heterostructures. The PL response for the four samples are shown in Figure 7.4. Characteristic photon emissions energies corresponding to the A and B photon nodes at 625 and 675 nm, respectively, are visible for the three-layer MoS_2, consistent with the results seen in Figure 4.4. In addition, a characteristic WS_2 PL peak is visible at 625 nm, consistent with results found in the literature[260-262]. The 625 nm peak corresponds to a photon emission of 2 eV, indicating that

the synthesized WS_2 also exhibits a consistent band structure and band gap with films in literature synthesized at high temperatures.

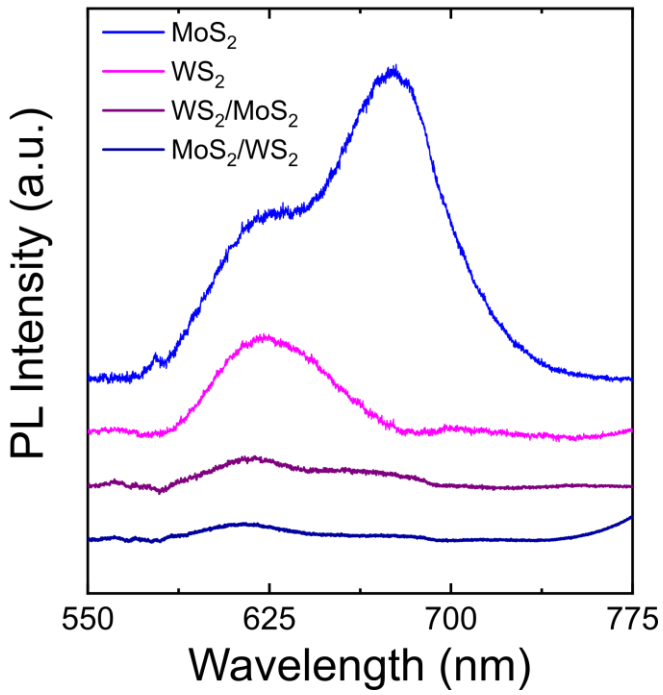

Figure 7.4. PL response of tri-layer MoS_2 and WS_2, as well as both heterostructure stacks. The A and B photon peaks are visible for MoS_2 at ~625 and ~675 nm.

When the MoS_2 and WS_2 films are coupled into a heterostructure, the resulting PL peak intensity is significantly quenched. This quenching is observed in both heterostructure orientations, again indicating that synthesis order does not strongly influence either material. This quenching has been associated with exciton dissociation, where excited carriers migrate across the p-n junction formed at the MoS_2/WS_2 interface to their associated lower energy levels[263-264]. When the excitons dissociate and split, no carriers coexist locally to recombine and emit photons, effectively diminishing PL response. The fact that the low temperature synthesized heterostructures exhibit PL quenching suggests

that the MoS_2 and WS_2 have homogeneous band structures and form a clean junction, successfully forming a p-n junction at the interface. However, because increasing a TMD's thickness by adding layers shifts its band structure from a direct to indirect band gap, thicker TMDs commonly exhibit minimal PL response[265-266]. As stated previously, the increase in Raman peak separation for the heterostructures compared to the peak separation for the individual materials (Figure 7.3 (a)) indicates that the separate materials behave as though they are thicker than they actually are. As such, it is entirely possible that the observed PL quenching in Figure 7.4 is due to an effective increase in film thickness, further decreasing the changes for exciton recombination at the optical bandgap. At this point, it is difficult to concretely determine the mechanism driving the PL quenching.

In order to suppress direct tunneling across the TMD layers, thicker heterostructures were synthesized for device measurements. The thickness of the heterostructure was doubled, where six layers of both MoS_2 and WS_2 were synthesized layer-by-layer utilizing a 12-step synthesis process. An XPS depth profile of a MoS_2/WS_2 heterostructure (MoS_2 synthesized before WS_2), shown in Figure 7.5, was performed to investigate the discretization of the two TMD layers. The atomic fractions shown in Figure 7.5 are calculated by integrating the total peak area of each element and normalizing the area the element's sensitivity factor. It is important to note that because the sampling depth of the XPS used is relatively deep (> 5 nm), each measured point consists of a convolution of multiple layers in the structure.

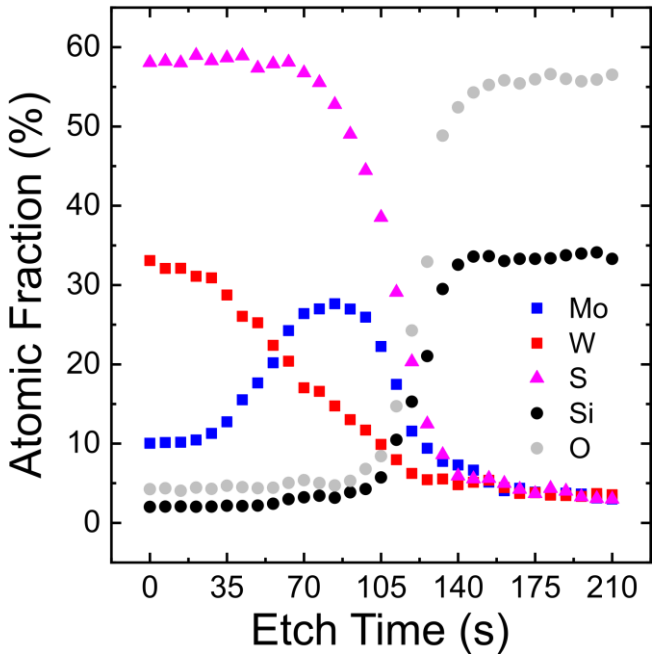

Figure 7.5. XPS depth profile of a 12-layer MoS_2/WS_2 heterostructure, as synthesized on a SiO_2 substrate.

The depth profile shown in Figure 7.5 reveals that the heterostructure was synthesized successfully, where relatively discretized molybdenum and tungsten regions can be seen. Between seconds 0 and 35 of sputtering, primarily tungsten is detected, with a relatively small contribution of signal coming from molybdenum. At around 50 seconds of sputtering, the molybdenum signal overtakes the tungsten, indicating that the measurement has reached the underlying MoS_2. However, it is important to note that a significant amount of tungsten signal is detected during seconds 50 – 100. The residual tungsten signal suggests that the second transition metal sputtered does intercalate into the initial TMD. That is, tungsten sputtered onto MoS_2 will diffuse into the MoS_2, yielding a $Mo_xW_{1-x}S_2$ alloy. These alloys have been investigated for bandgap engineering[267], however the alloying observed in this case likely muddles the MoS_2/WS_2 interface and may

negatively impact device characteristics. Nevertheless, two distinct regions corresponding to molybdenum and tungsten sulfides are observed, indicating that the transition metal interdiffusion does not persist to the extent of forming a uniform alloyed film across the entire depth of the structure.

In addition, the total sulfur signal seen in Figure 7.5 is consistently approximately twice as strong as the combined signal from both transition metals, further indicating that the synthesized TMDs are close to stoichiometric. A sharp transition is observed at approximately 115 seconds, where the transition metal and sulfur signals decrease and are overtaken by the silicon and oxygen signals from the substrate. Notably the sulfur signal decreases more rapidly than the transition metals, due to the preferential sputtering of sulfur compared to transition metals[268]. The lack of significant molybdenum, tungsten, and sulfur signal in the substrate region indicates that the synthesis has minimal effect on the underlying SiO_2. This result is important in demonstrating that this synthesis process can be ported to similar oxide substrates (for example high-k dielectrics) without concerns of altering the electronic properties of the oxide. As such, any effects due to modifying the interlayers of the directly synthesized heterostructures discussed in CHAPTER 5 and CHAPTER 6 can be assumed to be minimal.

To study the electrical performance of the thick heterostructures, purely vertical heterostructures were fabricated from the 12-layer stacks. Because films synthesized on SiO_2 substrates are of higher quality, the films synthesized on SiO_2 substrates were utilized for device fabrication. The 12-layer stack was transferred onto gold contacts, after which top gold contracts were electron beam deposited on top of the heterostructure, resulting in a full device architecture of gold/MoS_2/WS_2/gold, from bottom to top.

The device characteristics for four different thick MoS_2/WS_2 heterostructures are shown in Figure 7.6. Although there is some variance in current density between the four devices, the behavior for each device is symmetric and does not exhibit the expected rectification characteristics. It is possible that the absence of rectification can be due to a lack of a well-defined interface between the two TMDs. In the absence of a pristine, discrete interface between the two different materials, it is probable that carriers are not impeded from injecting to the opposite material as they would be in a typical type-II band alignment. Due to the potential for transition metal intermixing, the current method of synthesis involving sputtering each transition metal is likely not well-suited for achieving discrete heterostructure synthesis with well-defined interfaces.

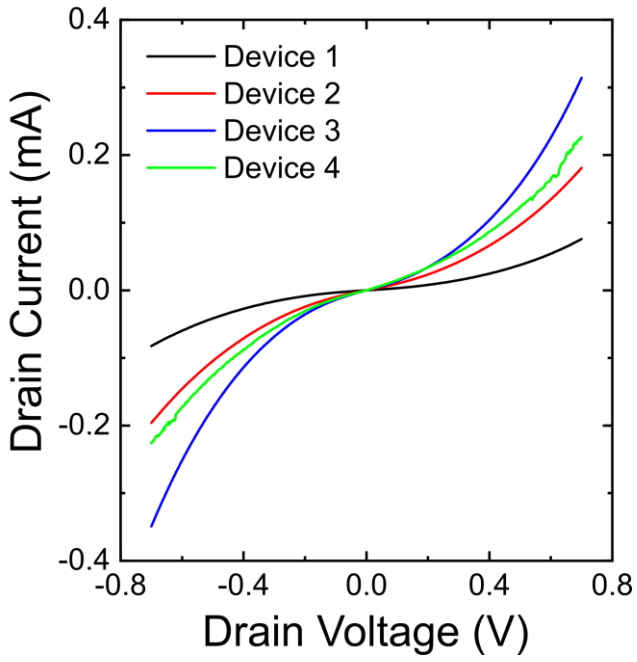

Figure 7.6. *I-V* characteristics of four 12-layer MoS_2/WS_2 heterostructure devices. Some variance in current density can be seen between individual device measurements, although the *I-V* relationship appears identical for each device.

Perhaps more interesting than the lack of rectification in the 12-layer heterostructure devices is the symmetry of the device in the positive and negative bias regimes. The nonlinearity in the *I-V* relationship shown in Figure 7.6 indicates that the devices' operation is predicated on tunneling across a barrier. One common source of tunneling is the Schottky barrier at the TMD/metal interfaces. Although the MoS_2/WS_2 interface is not as sharp as intended, the two gold/TMD interfaces should be dissimilar, based on the depth profile shown in Figure 7.5; one interface is predominantly MoS_2/gold, while the opposite interface is WS_2/gold. Because the work functions and electron affinities of MoS_2 and WS_2 differ, the Schottky barrier height formed at both interfaces should be different, which in turn should yield asymmetric injection behavior. The fact that the observed behavior in Figure 7.6 indicates that there is an additional mechanism influencing the gold/TMD interfaces, enabling symmetric behavior in both bias regimes.

One possible explanation for the symmetric behavior seen in Figure 7.6 is rooted in Fermi level pinning at the TMD/metal interfaces. It has been demonstrated that defects in TMDs can pin the work function of a coupled metal close in energy to defect levels, reducing the effective barrier height at the interface[158-159]. Our material synthesized at 400 ^{o}C has been shown to be highly defective (CHAPTER 4), so it is highly likely that Fermi level pinning effects play a significant role in determining each TMD metal interface.

To further investigate the tunneling mechanisms and potential pinning effects responsible for device operation, temperature dependent measurements were performed on the 12-layer MoS_2/WS_2 heterostructure devices. Figure 7.7 (a) plots the *I-V* relationship of a 12-layer heterostructure device measured at 300 K and 77 K. When measured at low temperatures, the device maintains its symmetric behavior in both the positive and negative

bias regimes. However, the *I-V* relationship clearly exhibits a temperature dependence, where the slope of the *I-V* curve changes between the two measurement temperatures.

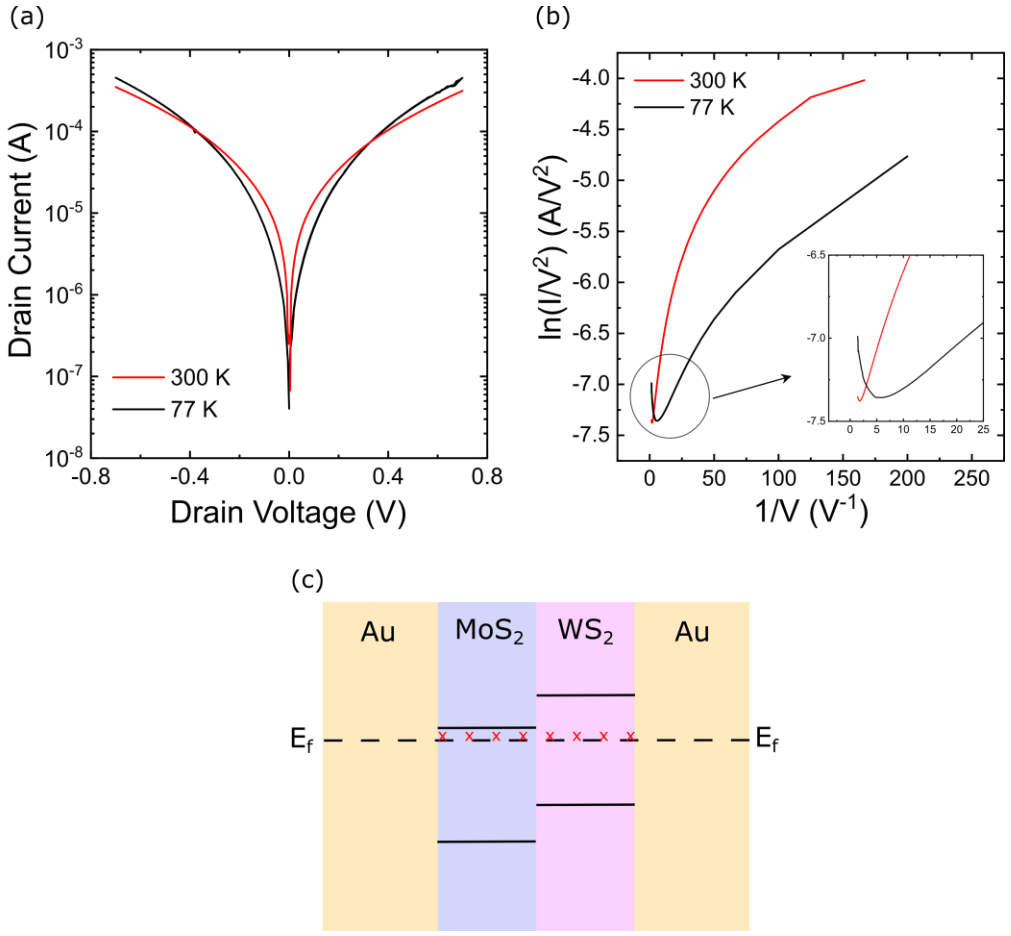

Figure 7.7. (a) Device behavior of a 12-layer MoS_2/WS_2 heterostructure, measured at temperatures of 77 and 300 K. (b) FN plot of the device data shown in (a) for both measurement temperatures. The inset shows a zoomed in view of 1/V values close to 0. The minimum corresponds to the FN threshold voltage, which can be extracted as 0.19 and 0.46 V for the low and high temperature measurements, respectively. (c) A simplified band alignment of the heterostructure, where defects in the MoS_2 and WS_2 pin the Fermi level across the structure. Note that built-in potentials and band bending at interfaces is ignored for simplicity in this diagram. The band diagram is not to scale.

This temperature dependence is can be further explored by re-plotting the *I-V* response shown in Figure 7.7 (a) in FN form. Figure 7.7 (b) shows the *I-V* response of a

12-layer heterostructure device as a function of measurement temperature in a FN pot; the inset shows a zoomed in view of the low 1/V (high V) region. As discussed earlier, the minimum in the *I-V* relationship in FN form represents the transition between thermionic emission and direct tunneling to FN tunneling, where FN tunneling occurs at higher voltages. The temperature dependence of the FN threshold voltage can yield information on the effective barrier height, which will be discussed in more detail later. As seen in the inset of Figure 7.7 (b), the FN threshold voltage in MoS_2/WS_2 heterostructure devices is moderately dependent on temperature, where the threshold voltage shifts from 0.19 V at 77 K to 0.46 V at 300 K. The moderate temperature dependence suggests that the height of the tunnel barrier restricting current flow is at least a few tenths of an eV, which is discussed in more detail in CHAPTER 8. Because the device behavior is symmetric in both bias regimes, it is likely that this effective barrier height is the same for both directions of electron injection.

To fully understand the mechanism yielding the symmetric device behavior, the potential pinning effects must be correlated to the symmetric injection behavior. To present a more complete picture of the effects taking place, a rudimentary band structure of the entire heterostructure can be constructed, which is shown in Figure 7.7 (c). It is important to note that this band structure is simplified, where effects such as band bending and built in potentials are ignored. However, this representation is sufficient for understanding the mechanisms that yield symmetric behavior in these heterostructure devices.

When sulfur vacancies exist in MoS_2 and WS_2, defect states are introduced into the band gap. These defect states differ in energy relative to the valence and conduction bands of each material. In the case of MoS_2, a shallow donor state is introduced that is nearly

degenerate with the conduction band edge; conversely, V_S in WS_2 introduce midgap states that lie around 0.4 eV below the conduction band minimum[269]. However, both defect states reside close to one another in energy with respect to the vacuum level, meaning that when MoS_2 and WS_2 are coupled, the V_S states in both material align closely to one another[257, 269]. These defect levels are represented as red Xs in Figure 7.7 (c).

As previously noted, the MoS_2 and WS_2 synthesized at 400 ^oC is very defective, and therefore the density of sulfur vacancies is likely high. In the case of a high defect density, the density of states at the associated defect state energies is proportionally high. Therefore, the it is likely that strong Fermi level pinning occurs when a metal is coupled to this material. When a metal is strongly pinned, the work function of the metal (and therefore the Fermi level in the semiconductor) is raised to the defect state energy. However, because the defect energies in MoS_2 and WS_2 are closely aligned in energy space, the Fermi level is pinned to a single energy across the structure. The Fermi level is shown pinned close to the defect energies in Figure 7.7 (c). Note that the band diagram and associated energy levels are not drawn to scale.

Because the work function of the metal, and therefore Fermi level in the MoS_2, lies close in energy to the conduction band minimum, electrons can easily inject directly into the MoS_2 conduction band. Therefore, any tunneling that occurs in the heterostructure under an applied bias consists solely of electrons tunneling across the WS_2 layer. As such, the tunnel barrier height in the two bias regimes consists of the difference in the conduction bands of MoS_2/WS_2 and the difference between the WS_2 conduction band and gold work function coupled to the WS_2. Because the defect states in MoS_2 align closely with the defect energies in WS_2, the work function of the gold coupled with the WS_2 aligns with the work

function of the gold coupled to the MoS_2, and therefore the MoS_2 conduction band as well. Consequently, the two barrier heights on both WS_2 interfaces are equal, which then results in the symmetric tunneling behavior in both bias regimes observed in Figure 7.6.

This pinning behavior is also consistent with the device results shown in Figure 5.3. In the gold/MoS_2/gold heterostructure using MoS_2 synthesized at 400 ^oC, the conduction across the structure is ohmic in both the high and low resistance states. Schottky barrier effects are commonly observed in metal/TMD interfaces, giving rise to an exponential *I-V* relationship due to tunnel-based injection across the Schottky barrier[270]. However, the MoS_2 heterostructures fabricated using 400 ^oC shown in Figure 5.3 exhibit purely ohmic behavior and do not show any exponential injection behavior. This behavior is well described by band alignment due to pinning shown in Figure 7.7 (c), further supporting the presence of strong pinning effects that fix the metal work function to the sulfur vacancy defect energy.

7.3 Conclusions

In this chapter, WS_2/MoS_2 heterostructures synthesized sequentially at low temperatures were investigated. Initially, WS_2 synthesis at 400 ^oC was demonstrated using the technique discussed in CHAPTER 4 by exchanging the molybdenum sputter step for a tungsten sputter step. Similar control over thickness was observed by cyclically synthesizing WS_2 layer-by-layer. The WS_2 exhibited high stoichiometry, indicating that the two-step synthesis technique can also be ported to additional TMD systems.

WS_2/MoS_2 heterostructures were directly synthesized layer-by-layer. Raman measurements indicate that discrete MoS_2 and WS_2 regions exist in heterostructures synthesized in both MoS_2/WS_2 and WS_2/MoS_2 orientations. However, both three-layer MoS_2 and WS_2 exhibit electronic structures akin to 6-layer films. The similarities in atomic structure between MoS_2 and WS_2 appear to couple the material together such that they do not behave as independent materials adjacent to each other, but rather separate materials with an electronic structure corresponding to the total thickness of the heterostructure. XPS measurements indicate that the "total" stoichiometry of the structure is independent of synthesis order, and that the total structure maintains a near-stochiometric atomic ratio. However, XPS depth profiling reveals that some amount of transition metal intermixing occurs, indicating that the sputter-based synthesis approach used for low temperature synthesis may not be suitable for heterostructure synthesis with dissimilar transition metals. However, discrete molybdenum and tungsten rich regions can be seen, indicating that the intermixing does not fully alloy the entire structure.

Electrical measurements of the MoS_2/WS_2 heterostructures do not yield the expected rectifying behavior, and moreover exhibit a symmetric *I-V* relationship. The behavior is exponential, indicating that the device operates on tunneling across a barrier. Temperature dependent measurements reveal that the FN threshold voltage and *I-V* behavior changes between high and low temperature measurement conditions, suggesting a non-trivial barrier height. By visualizing band alignment of the full heterostructure, it is apparent that sulfur vacancies introduce defect states that strongly pin the Fermi level across the structure and enable direct electron injection into the conduction band of the MoS_2. In addition, the defect states in MoS_2 and WS_2 align in energy, leading to a

symmetric tunnel junction across the WS_2 from the MoS_2 conduction band to the opposite gold contact.

These results indicate that sulfide heterostructures can be successfully synthesized at low temperatures, although there is significant room for optimization to limit intermixing and reduce defect density. In addition, these experiments highlight the relevance of Fermi level pinning at the metal/TMD interface, in particular its relevance when working with low quality materials.

CHAPTER 8. FERMI LEVEL PINNING AT THE MOS_2/METAL INTERFACE

An important consideration for all heterostructure devices is the influence of Fermi level pinning at the metal/semiconductor interface. The pinning studies found in the literature discussed previously explored defect effects on pinning strength, and demonstrated atomic scale inhomogeneities in the effective barrier height between the MoS_2 and metal contact. However, little work has been conducted to investigate the effect of wafer-scale MoS_2 quality (i.e., quality differences on a scale larger than 10 μm) on pinning and the resulting device behavior. The results shown in CHAPTER 7 demonstrate the impact that Fermi level pining can have in heterostructure devices, especially when working with lower quality material. Therefore, this work explores the impact of wafer-scale MoS_2 quality on Fermi level pinning. MoS_2 of varying qualities are synthesized and subsequently characterized using Raman spectroscopy and XPS. Symmetric and asymmetric purely vertical heterostructure devices are fabricated from both film qualities, and their electrical characteristics are measured and modeled to determine the dominant injection mechanism. UPS is used to probe the work function of the metal/MoS_2 interfaces, which show consistency with the electrical measurements by revealing lower effective work functions of metal in contact with low-quality MoS_2. Whereas the previous chapters focused on material synthesized at low temperature, this chapter will explore Fermi level pinning effects in MoS_2 films synthesized at higher temperatures. As Fermi level pinning is a subtler mechanism, high temperature synthesized films are used in order to mitigate any effects unrelated to pinning.

8.1 Purely Vertical Heterostructure Device Operation

The device architecture utilized for this pinning study is the simple two-terminal metal/TMD/metal heterostructure, shown in Figure 8.1 (a) for the case of MoS_2. As stated earlier, current flow through this device is purely vertical and out-of-plane; no lateral current transport occurs through the MoS_2. The three injection mechanisms (Direct tunneling, TE, and FN injection) are represented by the band diagram of the heterostructure device shown in Figure 8.1 (b). With sufficient MoS_2 thickness (greater than ~5 nm), direct tunneling is mitigated and carrier injection is limited to TE and FN injection. Both of these injection mechanisms strongly depend on the Schottky barrier height, which in turn can be influenced by pinning effects. Therefore, different levels of pinning strength should yield different injection behavior, and therefore different device characteristics.

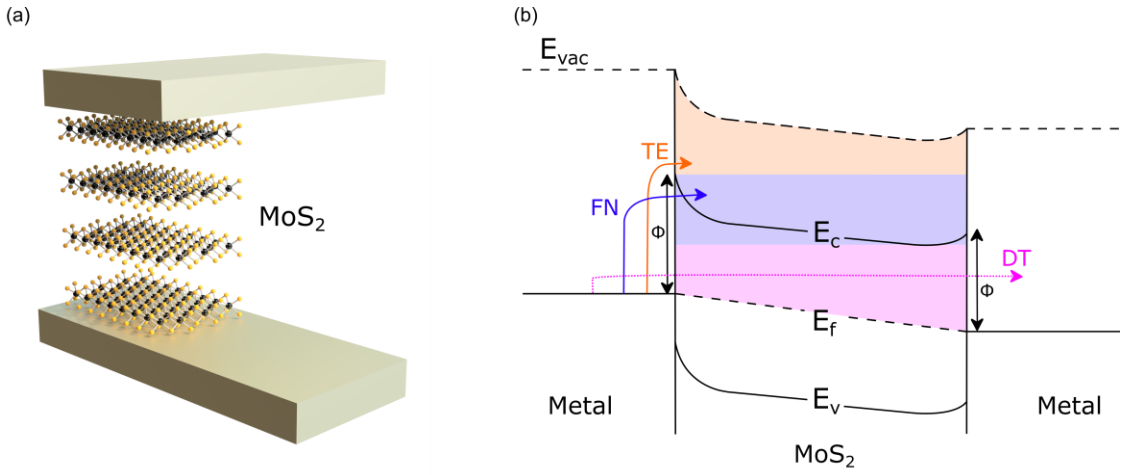

Figure 8.1. (a) Schematic of a metal/TMD/metal purely vertical heterostructure, with MoS_2 as the TMD. The associated band structure of the device is shown in (b). The three forms of carrier injection are shown via colored arrows along with their associated energy levels. The three injection mechanisms are TE, FN tunneling, and DT.

8.2 Synthesis of Varying Quality MoS_2 Films

To generate MoS_2 films of various qualities, MoS_2 synthesis was performed at "low" (700 ^oC) and "high" (900 ^oC) temperatures[68]. Molybdenum (1 nm) was evaporated onto a thermally grown SiO_2 by electron beam evaporation. The thin film was placed in a tube furnace along with a quartz crucible with 50 mg of sulfur powder (sigma-Aldrich). The furnace was evacuated to a base pressure of 10^{-6} Torr and then backfilled with argon to 5 Torr. The chamber was then sealed, and the temperature was increased to the desired synthesis temperature (700 and 900 ^oC), whereupon temperature was held for 1 hour before cooling under argon.

Representative Raman spectra for each synthesis are shown in Figure 8.2 (a). The peak separation between the out-of-plane A_{1g} phonon node and the in-plane E^1_{2g} phonon node yields film thickness information[215]. Both the high and low temperature synthesized MoS_2 yield spectra with a peak separation of 23.4 cm^{-1}, consistent with three-layer MoS_2. Minor variation over the full 2 x 2 in^2 wafer was observed, with an inhomogeneity of only ± 0.2 layers measured. The FWHM of both peaks also yields qualitative information about the physical structure of the film, with sharper peaks indicating higher quality material[103, 213]. As noted in Figure 8.2 (a), the 900 ^oC MoS_2's A_{1g} and E^1_{2g} FWHMs are both sharper and closer to values obtained from exfoliated geological MoS_2 crystals than the 700 ^oC synthesized film, indicating that the 900 ^oC film is of higher quality[68].

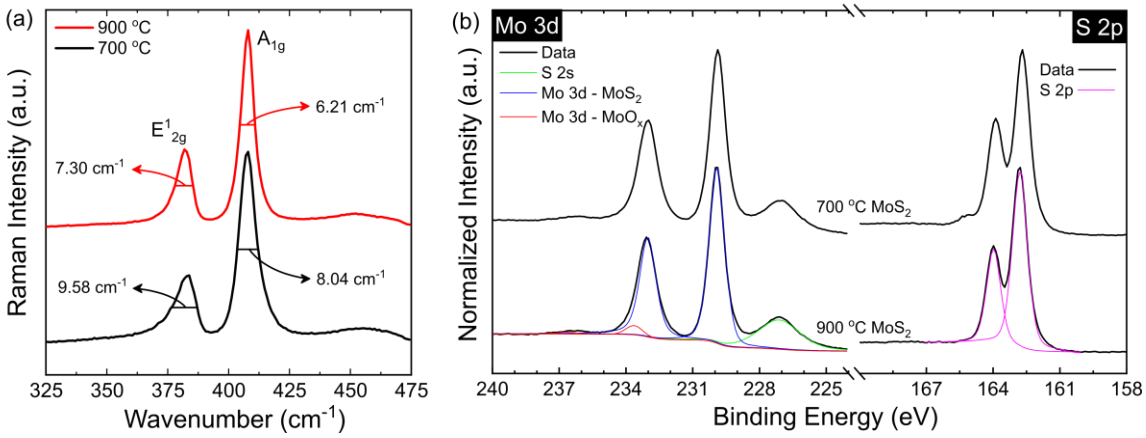

Figure 8.2. (a) Raman spectra for the 900 and 700 °C synthesized MoS_2. Peak widths for the A_{1g} and E^1_{2g} peaks are shown, with uncertainty on the order of ±0.04 cm^{-1}. (b) XPS Mo 3d and S 2p spectra for the 900 and 700 °C synthesized MoS_2, including the peak fits for the 900 °C synthesis. The Mo 3d spectrum includes the S 2s contribution as well as the MoS_2 and MoO_3 Mo 3d doublets. The S 2p is fit with a single S 2p doublet.

To determine the stoichiometry of the MoS_2, XPS was performed on the synthesized films. Figure 8.2 (b) shows the Mo 3d and S 2p XPS spectra for the 900 and 700 °C synthesized MoS_2, as well as the fit for the 900 °C spectra. To fit the Mo 3d spectrum, five standard peaks are used: The S 2s found at approximately 227 eV, a Mo 3d doublet corresponding to the MoS_2 Mo $3d^{5/2}$ and $3d^{3/2}$ peaks, and a second Mo 3d doublet corresponding to the MoO_3 Mo $3d^{5/2}$ and $3d^{3/2}$ peaks[271]. The peak separation of each Mo 3d doublet between Mo $3d^{5/2}$ and $3d^{3/2}$ is held constant at 3.1 eV, and the area ratio between the peaks is fixed at 1.5:1. Additionally, the peak widths of all four Mo 3d peaks are constrained to be the same. The position of each doublet relative to the other, as well as the S 2p peak, is allowed to change. All parameters corresponding to the S 2p peaks were unconstrained. Similarly, the S 2p spectrum is fit with a single doublet corresponding to the S $2p^{3/2}$ and $2p^{1/2}$ peaks, with the peak separation fixed at 1.18 eV, the peak widths

constrained to be the same, and the area ratio between the S $2p^{3/2}$ and $2p^{1/2}$ fixed at 2:1. Both the Mo spectrum and S spectrum are consistent with the position and peak shapes of the semiconducting 2H phase of MoS_2[48].

The stoichiometry calculation was performed by normalizing the area of the MoS_2 Mo 3d doublet by molybdenum's sensitivity factor (2.75), by normalizing the area of the S 2p doublet by sulfur's sensitivity factor (0.54),[216] and taking the ratio of the normalized peak areas. Doing so for 900 ^oC MoS_2 yields a stoichiometry of 1.99:1, nearly at the perfectly stoichiometric 2:! Ratio. The Mo 3d and S 2p spectra for 700 ^oC MoS_2 are nearly identical in peak shapes, positions, and relative intensities, and the stoichiometry calculation from the fitted spectra yield an atomic ratio of 1.98:1.

The difference in Raman peak widths and similarity in stoichiometries between the 700 ^oC and 900 ^oC MoS_2 indicates that the primary difference in quality between the two films involves atomic structure and grain size[103]. The 700 ^oC film therefore has a higher density of grain boundaries, which typically are Mo-terminated and are high-energy sites[272-273].

8.3 Symmetric Heterostructure Device Behavior

To study the effects of Fermi level pinning in metal/MoS_2/metal heterostructure devices, purely vertical two-terminal heterostructures were fabricated in a cross-point architecture, shown optically in Figure 8.3 (a). Each set of 8 cross-bars (4 bottom and 4 top) yield 16 devices per array, with a single device located at the intersection of each

cross-bar. Each cross-bar has a width of 10 µm, resulting in an active device area of 100 µm^2. Planar, three-layer MoS_2 was repeatedly transferred using a standard wet transfer method[15] to yield approximately 6 nm of MoS_2 encapsulated between top and bottom 80 nm gold contacts. Each intersection of cross-bars results in the same device structures shown in Figure 8.1 (a), which consists of van der Waals MoS_2 stacked vertically between symmetric gold contacts.

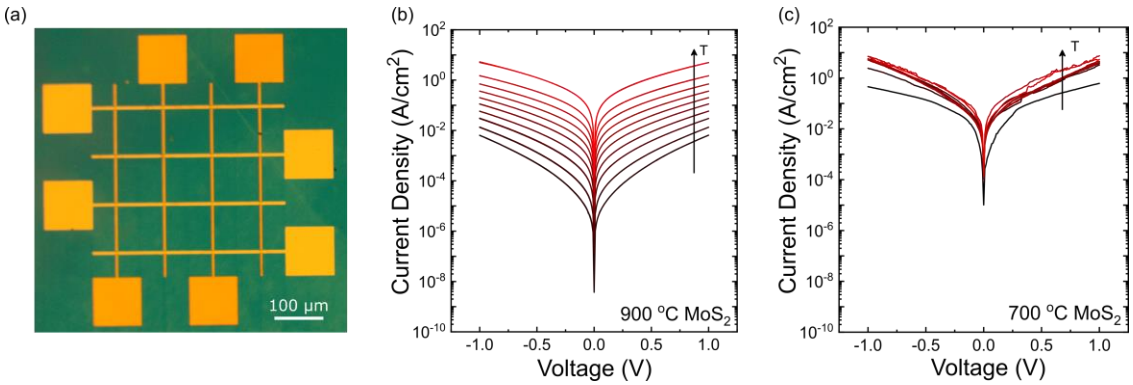

Figure 8.3. (a) Optical image of a cross-point array of purely vertical heterostructures. Each intersection between cross-bars is a single active device. Temperature dependence of I–V measurements for the 900 (b) and 700 °C (c) MoS_2 vertical structures. Measurements were conducted at temperatures ranging from 100 K (black curves) to 400 K (red curves) in increments of 30 K.

As discussed previously, the current through the vertical heterostructures is due to a combination of FN and TE injection. FN injection is a process that follows an exponential tunneling form

$$I_{FN} \propto \frac{V^2}{\emptyset} \exp\left(-\frac{8d(2m)^{1/2}\emptyset^{3/2}}{3\hbar qV}\right) \qquad \textbf{8.1}$$

where V is the applied bias, m is the carrier effective mass, $\hbar$ is the Plank constant, d is the Schottky barrier width, and φ is the Schottky barrier height (SBH)[231, 265, 274-277]. Because the FN tunnel current is dependent on the integral of the difference in Fermi functions in the metal and MoS_2, FN tunnel current can be regarded as temperature-independent. Therefore, FN injection should contribute equally to current density across all measurement temperatures[25]. In contrast, TE injection is a temperature-dependent process and is of the form

$$I_{TE} = A^* T^2 e^{-q\varphi/kT}\left(e^{qV/kT} - 1\right) \quad \textbf{8.2}$$

where A^* is the Richardson constant, T is the temperature, and k is the Boltzmann constant[276, 278-279]. Both FN and TE injection mechanisms are dependent on the effective barrier height at the metal/MoS_2 interface, and therefore any changes in the barrier height due to Fermi level pinning should influence both injection mechanisms.

The temperature dependence of the current-voltage relationship is shown for both high- and low-temperature MoS_2 devices in Figure 8.3 (b,c). The 900 ^oC MoS_2 devices exhibit a strong temperature dependence across the temperature range of 100-400 K. Conversely, the 700 ^oC MoS_2 exhibits essentially no temperature dependence. Additionally, the current density at all temperatures for the 700 ^oC MoS_2 is similar in magnitude to that for the 900 ^oC MoS_2 at high measurement temperatures (i.e., >340 K).

An alternative way to view the I-V data shown in Figure 8.3 is in an FN plot. By viewing the I-V data in a $\ln(I/V^2)$ versus $1/V$ form, the transition between FN tunneling and TE injection can be observed as the minimum in the $\ln(I/V^2)$ curve[231, 280]. The temperature

dependence of the 900 ^{o}C MoS_2 devices is shown in Figure 8.4 (a). From inspection, two distinct features immediately visible in the data. First, the strong temperature dependence is again visible, with increasing temperature giving rise to larger current densities. The second feature is subtler: the FN threshold voltage shifts to higher voltages with increasing temperature, as highlighted by the blue triangle. Alternatively, this phenomenon can be described as the FN threshold voltage shifting to lower voltage values with decreasing temperature. This shift agrees with the conventional understanding of carrier injection; by decreasing the temperature, TE injection is mitigated and less FN tunnel current is required to dominate the *I-V* relationship[281-282]. The *I-V* characteristics of the 700 ^{o}C MoS_2 devices are shown in Figure 8.4 (b). In contrast to the 900 ^{o}C MoS_2 devices, the 700 ^{o}C devices not only exhibit minimal temperature dependence, but the FN threshold voltage also does not exhibit the same shift to higher voltage values with increasing temperature. The lack of FN threshold dependence on measurement temperature exhibited by the 700 ^{o}C MoS_2 devices as well as the strong FN threshold temperature dependence exhibited by the 900 ^{o}C MoS_2 devices is shown in Figure 8.4 (c). For the 900 ^{o}C devices, the voltage required to shift from TE injection to FN injection increases from 0.2 V to nearly 0.7 V from 130 to 400 K. Conversely, the 700 ^{o}C devices show no apparent temperature dependence, where the FN threshold voltage maintains a constant average value of approximately 0.4 V.

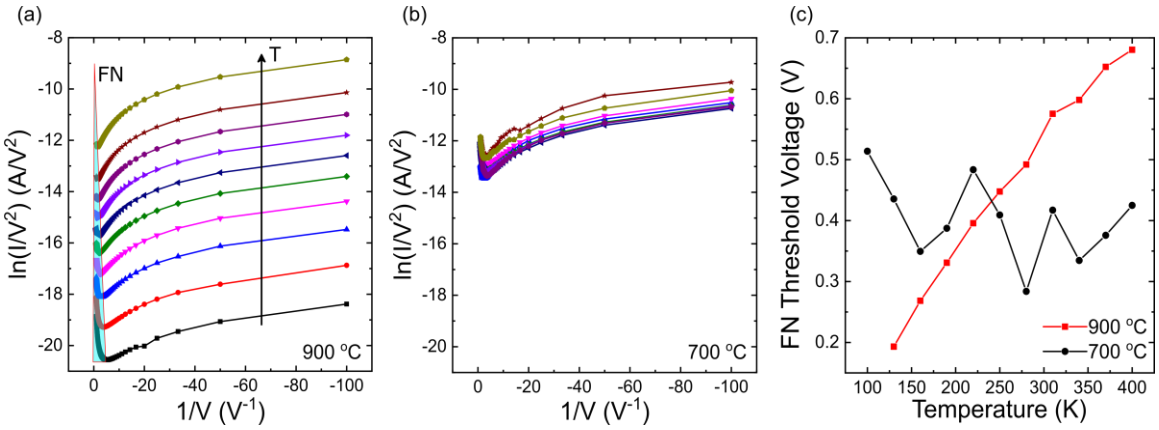

Figure 8.4. FN plots of the temperature dependence of the *I*−*V* relationship for 900 (a) and 700 °C (b) devices. The FN injection regime is highlighted in (a) by the blue triangle. The temperature dependence in (b) is essentially nonexistent. The FN threshold voltage at each temperature for both MoS_2 films is shown in (c). Error bars are smaller than the shown data points.

The disparity in temperature dependence between the high- and low-quality MoS_2 devices suggests that the low-quality MoS_2 devices are dominated by a temperature-independent mechanism, whereas the high-quality MoS_2 devices have contributions from both temperature-independent and -dependent mechanisms. To verify that these two mechanisms of injection are consistent with the observed behaviors of the 900 and 700 °C MoS_2 devices, device modeling was performed to fit the measured *I*-*V* data.

From eq. **Error! Reference source not found.**, the barrier height at the gold/MoS_2 interface can be extracted using the slope of the high voltage FN regime of the $\ln(I/V^2)$ versus $1/V$ trendline. Rewriting eq. **Error! Reference source not found.** yields

$$q\emptyset = \left(\frac{(slope)(3hq)}{8\pi d\sqrt{2m^*}}\right)^{2/3} \qquad \textbf{8.3}$$

where d is the FN barrier width. From the slope of the linear portion of the trendline in the low $1/V$ regime, an effective barrier height can be extracted, given an effective electron mass and Schottky barrier width. An effective mass ratio of $0.18m^*/m_o$ is used, as per the results of Zhu et al[231]. This specific value is chosen because the effective mass was calculated specifically in the out-of-plane direction, corresponding to the orientation of current flow in these purely vertical heterostructures. An effective barrier width of 0.3 nm is used, as per the study by Ahmed et al[275]. Ahmed et al. utilized 14 nm-thick MoS_2 flakes in their experiments, a thickness that produced interface characteristics analogous to "bulk" MoS_2 contacted with metal. Similarly, this work uses relatively thick MoS_2 films, so values corresponding to the interaction between "bulk" MoS_2 and metal are essential. By taking the slope of the linear portion of the trendline in the low $1/V$ regime, using the out-of-plane effective mass for MoS_2 calculated by Zhu et al.[231] and the barrier width determined by Ahmed et al.[275], the effective barrier height can be extracted for the gold/MoS_2 interface for both the high- and low-quality MoS_2 devices. Specifically, a barrier height of 0.44 eV is extracted for the high-quality MoS_2/gold interface, whereas a height of 0.18 eV is extracted for the low-quality MoS_2 interface.

Using the extracted effective barrier heights determined from the FN injection portion of the *I-V* characteristics, contributions from both FN and TE injections can be modeled and compared to the measured device data using eqs. **Error! Reference source not found.** and 8.2, respectively. Figure 8.5 (a) shows the experimental device characteristics of the 900 ^oC MoS_2 devices measured at 130 and 500 K in a FN plot form. The single FN contribution and the two temperature-dependent TE contributions are superimposed, where TE injection dominates at low voltages (high $1/V$ values) and FN

injection dominates at high voltages (low 1/*V*). the modeled FN injection follows the description of the FN tunnel current well: a linear regime at high biases followed by a levelling off at low biases. Similarly, the modeled TE contributions align well with the experimental data, dominating injection behavior at low biases before being overtaken by FN injection at larger biases. The modeled device characteristics agree well with the measured behavior, indicating that FN and TE injections are the mechanisms that dictate device behavior. In addition, the effective SBH of 0.44 eV extracted from **Error! Reference source not found.** is in good agreement with both the measured behavior as well as previously studied injection barrier heights[231].

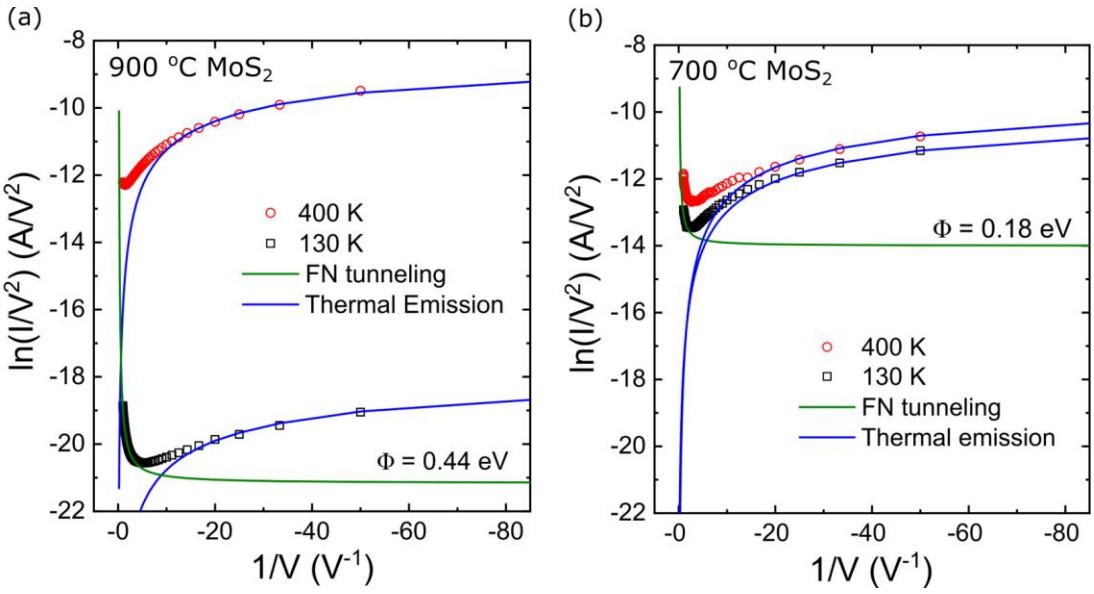

Figure 8.5. Modeled I−V characteristics of the 900 (a) and 700 °C (b) MoS_2. Measurement temperatures of 130 and 400 K are denoted by black squares and red circles, respectively. The FN and TE contributions are plotted in green and blue, respectively. Two TE curves are plotted in (a,b) because of the temperature dependence of the TE contribution.

The device characteristics measured at 130 and 400 K, as well as the FN and TE modeled contributions, for the 700 °C MoS_2 devices are shown in Figure 8.5 (b). Notably,

both high-and low-temperature measurements exhibit similar current magnitudes, which falls in agreement with the overall larger FN contribution across all biases. IN addition, the TE contribution loses some of its temperature dependence, where TE contributions at both 130 and 400 K exhibit similar current densities. The combination of increased FN injection along with mitigation of TE temperature dependence can be explained by the reduced effective SBH, which dropped significantly to 0.18 eV. The FN contribution in the low-voltage regime saturates at a larger value for a smaller barrier height, which is consistent with the findings from Zhu et al[231]. Additionally, these results demonstrate that a decrease in the effective barrier height leads to a smaller difference in TE contributions between two temperatures, evidenced by the similar current magnitudes for the 130 and 400 K measurements at the low bias regimes shown in Figure 8.5 (a,b).

The significant reduction in the barrier height in the 700 ^{o}C MoS_2 sample suggests that gold is susceptible to strong Fermi level pinning effects that arise from material quality effects. The increase in interaction may be due to an increase in the defect density and grain boundary edges in the MoS_2, which can act as sites for gold to interact more strongly with the adjacent MoS_2. The increased interaction leads to stronger electrostatic coupling between the layers, pinning the gold's work function and effectively reduced the SBH at the interface.

This observed change in SBH at the MoS_2/gold interface, observed experimentally and verified theoretically, is due to a change in the gold's effective work function. It appears that because the lower quality MoS_2 has an overall higher defect density (primarily due to grain boundaries), the MoS_2 pins the gold's work function at a higher energy level[161]. The reduction of the gold's effective work function reduces the barrier height at the

interface and enables a larger FN tunneling current density at a given applied bias. In contrast, the high-quality MoS_2 does not pin the gold's work function as strongly, resulting in a larger SBH and a lower overall FN tunnel current density. Because the SBH is larger, a larger applied bias is required to induce significant FN injection, and at higher temperatures, TE provides a larger injection current than FN tunneling at low-to-moderate biases. A band diagram schematic showing the differences between the high- and low-quality MoS_2 devices is shown in Figure 8.6 (a,b) respectively. In the case of low-quality MoS_2, the effective barrier height at the gold/MoS_2 interface is reduced because of a strong interaction between defect states in the MoS_2 and the adjacent gold. We also note that the 900 ^oC MoS_2 case is note absent from pinning effects, as metal-induced gap states (MIGS) cam exist in the absence of defects[158]; these results simply imply that defect effects strongly influence the pinning strength between the high and low MoS_2 film qualities when in contact with gold.

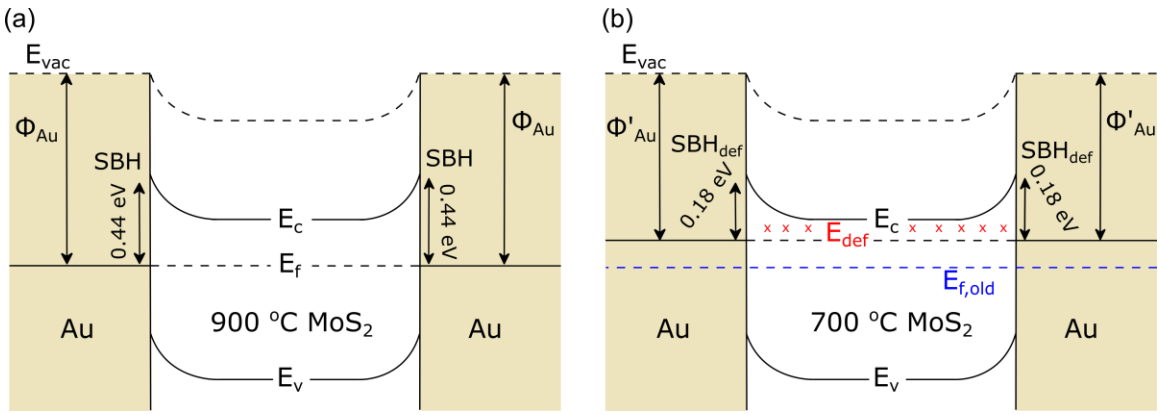

Figure 8.6. Band diagrams for the symmetric Au structures are shown in (a,b) for the 900 and 700 °C MoS_2, respectively. In (b), shallow conduction band defects are denoted by the red x, the work function of the Au when pinned is given by φ'_{Au}, and the defect-induced reduced effective SBH height is labeled as SBH_{def}. $E_{f,old}$ in (b) corresponds to the E_f and Au band edge when in contact with high quality MoS_2, where weaker pinning effects are assumed. Drawings are not to scale.

8.4 Asymmetric Heterostructure Device Behavior

Because the injection behavior at the MoS_2/metal interface is dependent on the contact metal's work function, choosing a metal with a different work function should significantly change the *I-V* behavior. As such, the role of material quality on fermi level pinning can be further explored. Therefore, a second set of heterostructure devices was fabricated, this time using platinum as the bottom contact metal. Platinum has a larger work function than gold and should yield asymmetric injection in the forward and reverse bias regimes because of offering SBHs at each interface[156, 283]. Specifically, the SBH of the MoS_2/gold interfaces is expected to be significantly lower than that of the MoS_2/platinum interface, and therefore injection into MoS_2 from gold (positive biases) is expected to be more favorable than injection from platinum (negative biases).

Room temperature *I-V* characteristics for the 700 and 900 ^oC asymmetric MoS_2 devices are shown in Figure 8.7 (a). the positive and negative bias regimes are highlighted as injection from gold and platinum, respectively, by the metal's corresponding color. Interestingly, the high-quality MoS_2 synthesized at 900 ^oC yields device characteristics that are symmetric, opposed to initial expectations. This result suggests that gold and platinum are pinned to a similar energy level when in contact with the 900 ^oC MoS_2/ leading to similar barrier heights at both interfaces. However, the 700 ^oC MoS_2 does result in asymmetric device characteristics, with approximately 2 times larger current densities in the gold injection regime. This implies that the barrier height at the gold/MoS_2 interface is

smaller than that at the platinum/MoS_2 interface, leading to preferential injection from the gold.

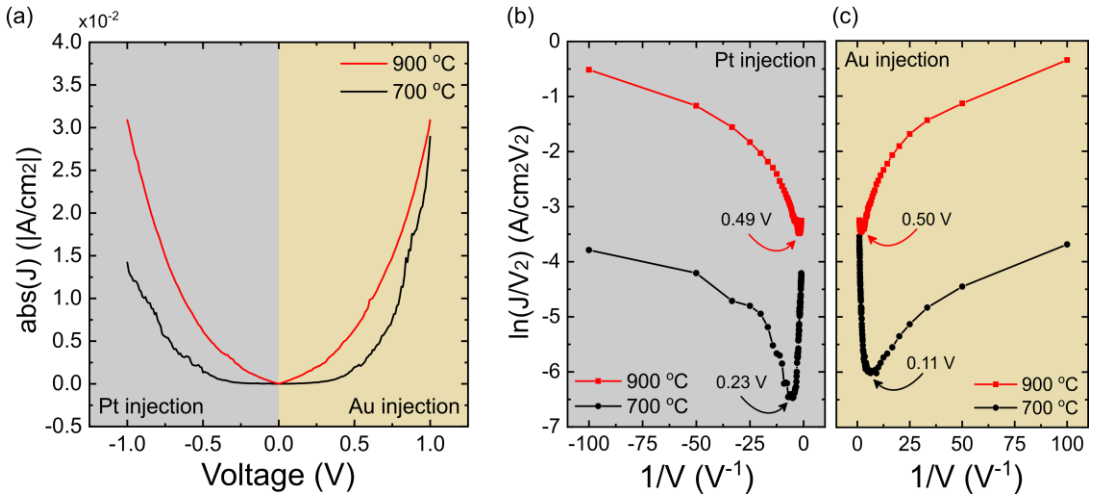

Figure 8.7. (a) Absolute value of the *I*−*V* relationship for the 900 and 700 °C MoS_2 asymmetric Au/Pt devices measured at room temperature. The positive bias regime corresponds to injecting electrons from the Au into MoS_2, whereas the negative bias regime corresponds to injecting electrons from the Pt into MoS_2. (b,c) show the same data plotted in (a) but presented in FN plots for the Pt and Au injection regimes, respectively. The FN threshold voltage is noted for each curve, given by the voltage value at each minimum.

The *I*-*V* characteristics are replotted in FN plot form in Figure 8.7 (b,c) for platinum and gold injections, respectively. The FN threshold voltage is given for each interface for both MoS_2 qualities. The FN threshold voltage for the 900 °C MoS_2 asymmetric structure is nearly identical for both injection regimes; TE is overtaken in the current density at near 0.5 V in both directions. The 700 °C asymmetric structure yields a noticeable different upon observation of the FN plots. The FN threshold voltage is larger at the Pt injection interface compared to that at the gold injection interface. The discrepancy between the two threshold voltages suggests that the gold's work function is pinned to a higher energy value than the platinum's work function, reducing the barrier height at the gold/MoS_2 interface

more drastically than the platinum/MoS_2interface. The reduction in the effective barrier height leads to an increased FN tunnel current, shifting the FN threshold voltage to lower values.

As performed for the symmetric gold/MoS_2/gold heterostructures, the effective barrier height can be extracted for both high-and low-quality MoS_2/platinum interfaces using eq. 8.3. Doing so yields an effective barrier height of 0.46 eV for the 900 ^oC MoS_2/platinum interface and a barrier height of 0.33 eV for the 700 ^oC MoS_2/platinum interface. The modeled behavior for the high- and low-quality dMoS_2 devices is shown in Figure 8.8 compared to their respective experimental data.

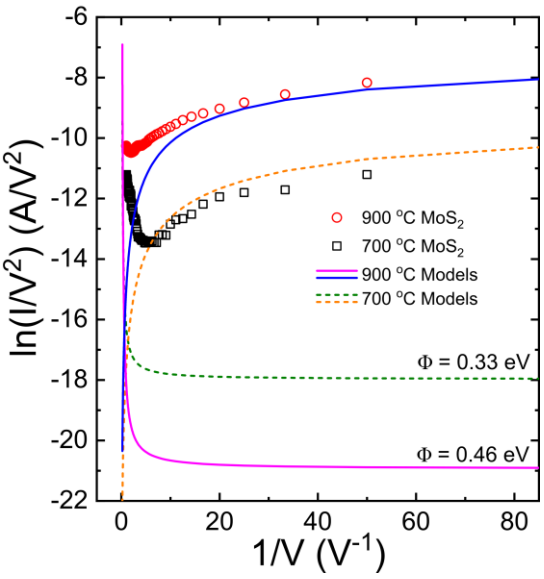

Figure 8.8. Modeled I−V characteristics of the 900 and 700 °C MoS_2 asymmetric heterostructures measured at room temperature. The FN and TE contributions are plotted as solid and dashed lines for the 900 and 700 ^oC devices, respectively.

8.5 Physically Characterizing the MoS_2/Metal Interface

To concretely probe the work function of the metal/MoS_2 interface, UPS was used to explicitly calculate the work function of a measured sample using the following equation

$$\emptyset = h\nu - (E_{SEE} - E_f) \quad \textbf{8.4}$$

Where $h\nu$ is the incoming photon energy, E_{SEE} is the secondary electron edge (SEE) energy, and E_f is the Fermi energy. Because the incoming photon energy is a known value and both the E_{SEE} and E_f can be extracted from the UPS spectrum, the work function can be explicitly calculated. Previous studies have used UPS to examine the effective work function of metals deposited onto MoS_2 as a function of the metal thickness[163], but to our knowledge, no studies have been performed on the effect of macroscopic MoS_2 quality on Fermi level pinning and the resulting metal work function.

Figure 8.9 (a) shows the UPS spectra for the as-grown 900 and 700 ^oC MoS_2 films. The SEE and E_f are highlighted on the 900 ^oC spectrum. Figure 8.9 (b,c) shows the UPS spectra for the bulk control gold and platinum surfaces, respectively. The statistical calculation of each surface's work function is shown in Figure 8.9 (d) using a standard box and whisker plot, and is consistent with the literature values of each surface's work function[156, 163, 283]. Notably, the 700 ^oC MoS_2 has a larger variance of the calculated work function compared to the 900 ^oC film, which can be attributed to the broader SEE the 700 ^oC film exhibits, seen by the increased width of the shaded region. The larger variance in the calculated work function can be attributed to increased inhomogeneity in the film because of the higher defect density and additional disorder. The calculated work functions of the control metals shown minimal variance.

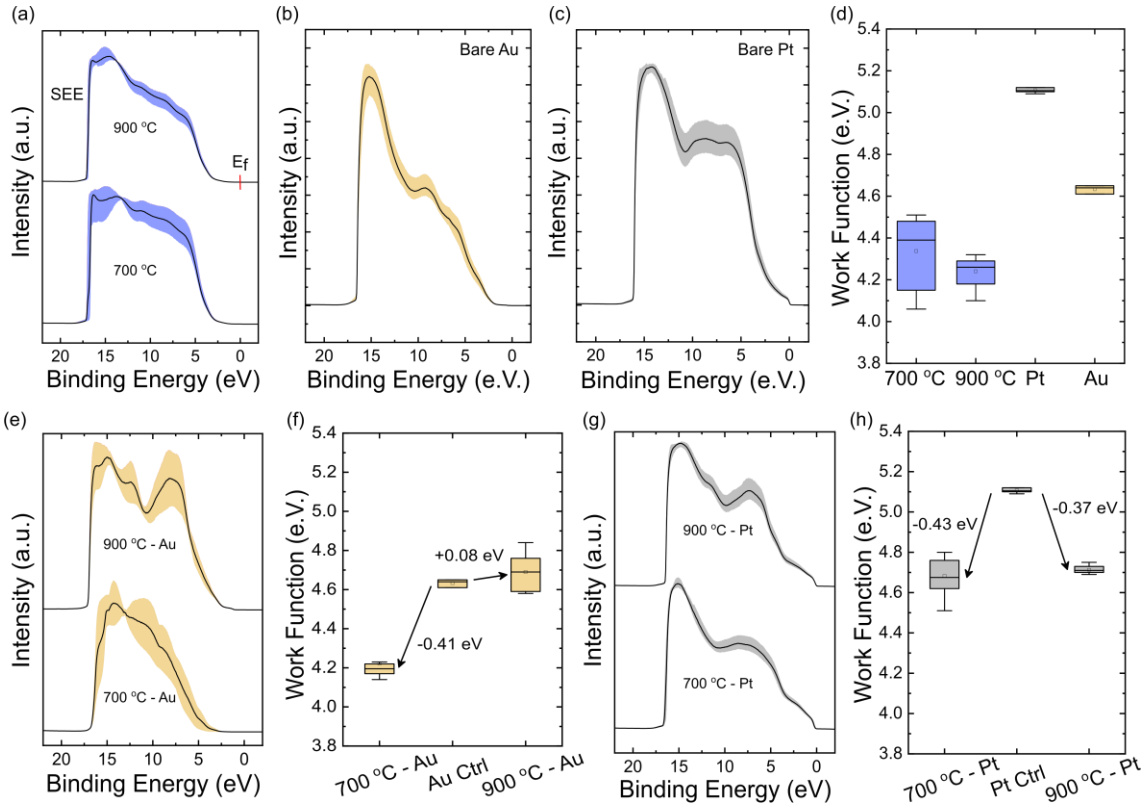

Figure 8.9. UPS spectra of MoS_2/metal interfaces. The UPS spectra for as-grown 900 and 700 °C MoS_2 are shown in (a). The secondary electron edge and E_f are shown on the 900 °C spectrum in (a). (b,c) show the control UPS measurements for bulk Au and Pt control surfaces, whereas (d) contains the statistics of the calculated work functions for each spectrum in (a–c). The measured UPS spectra for Au in contact with both high- and low-quality MoS_2 are plotted in (e), and the calculated work functions for both are compared to a bulk Au control's work function in (f). Similarly, (g) shows the UPS spectra for Pt in contact with high- and low-quality MoS_2 and (h) shows the calculated work functions compared to a bulk Pt control. For all spectra, the shaded region represents the area between the maximum and minimum spectra measured for each sample, and the solid black trendline represents the average of all spectra taken.

To determine the work function of the MoS_2/metal interface, samples were prepared where a thin metal layer was evaporated onto the high- and low-quality MoS_2. The thickness of the metal is strictly limited by the measurement depth of the UPS technique, and therefore depositing thicker metal films would skew the work function

determination by introducing the "bulk" metal[163]. Therefore, 0.5 nm of gold and platinum were deposited on both MoS_2 qualities via e-beam evaporation at a rate of 0.01 nm/s.

The UPS spectra for the 0.5 nm gold/MoS_2 interfaces are shown in Figure 8.9 (e), and the calculated work functions of each interface are shown in Figure 8.9 (f), along with the control gold work function. Noticeably, the work function of the gold in contact with the low-quality MoS_2 is drastically reduced, suggesting strong pinning toward the MoS_2 conduction band edge. Additionally, the 0.41 eV gold work function reduction is consistent with the extracted effective SBH reduction shown in Figure 8.5. The agreement between the modeled reduction in SBH from electrical results and measured work function change using UPS further supports the strong Fermi level pinning seen at the 700 ^oC MoS_2 gold interface. Conversely, the high-quality MoS_2 does not appear to strongly modify the gold work function, as the work function of the 900 ^oC MoS_2/gold interface exhibits a negligible shift from the control gold work function. Figure 8.9 (g,h) shows similar data pertaining to the platinum/MoS_2 interfaces. The work function calculations for the platinum interfaces yield interesting results. The 900 ^oC MoS_2 appears to pin the work function of the platinum to a similar value as the gold work function. the similar energy level that both metals are pinned to is consistent with the symmetric *I-V* relationship observed in Figure 8.7 and the similar extracted barrier heights in Figure 8.8.Gong et al. have shown theoretically that MIGS can occur in MoS_2 metal interfaces, leading to pinning effect that do not require a large defect density[158]. When observing gold's and platinum's work functions when in contact with the 700 ^oC MoS_2, a clear different of approximately 0.5 V is observed. The definitive difference in the interface work function at the gold/MoS_2 and platinum/MoS_2

interfaces corroborates the asymmetric *I-V* behavior and the different in the FN threshold voltage for each interface shown in Figure 8.7.

From the calculated work functions of each MoS_2/metal interface, a new set of representative band diagrams can be drawn. Band diagrams for the 900 and 700 ^oC MoS_2 asymmetric gold/platinum devices are shown in Figure 8.10 (a,b), respectively. Unexpectedly, the 900 ^oC MoS_2 asymmetric structure results in a relatively symmetric band diagram, where the different between the platinum and gold work functions is only 0.03 eV. Conversely, the 700 ^oC MoS_2 asymmetric structure results in an asymmetric band structure, where the difference between the platinum and gold work functions is 0.47 eV. The effective barrier heights extracted from Figure 8.8 are also included, showing similar barrier heights at each interface for the 900 ^oC MoS_2 and asymmetric barrier heights at each interface for the 700 ^oC MoS_2.

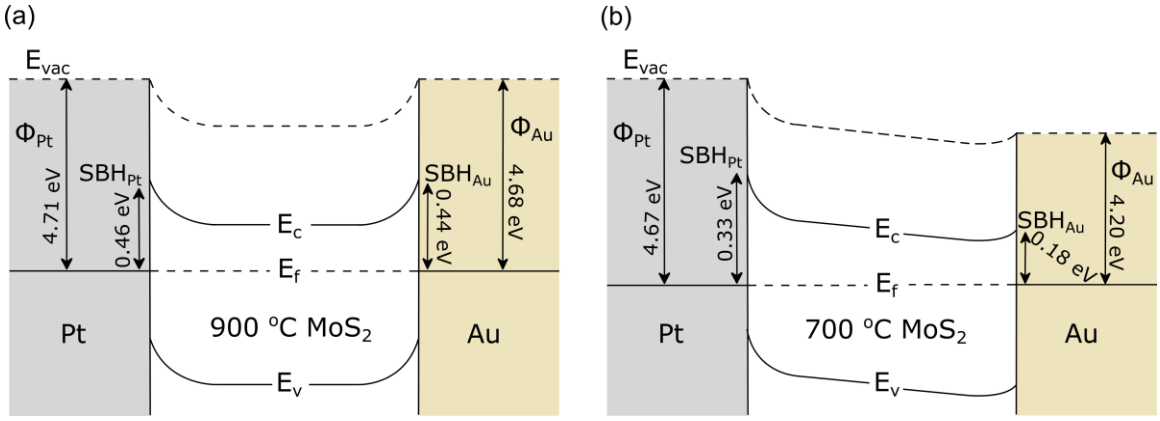

Figure 8.10. Band diagrams for the 900 (a) and 700 °C (b) MoS_2 asymmetric Pt/MoS2/Au vertical heterostructures, calculated using the extracted barrier heights from Figure 8.8 and the calculated work functions from Figure 8.9. Drawings are not to scale.

To understand the reason behind the significant difference in pinning between the high- and low-quality MoS_2 asymmetric structures, XPS was performed on each MoS_2/metal interface sample. By investigating shifts in the core levels, potential bonding and interactions can be determined between MoS_2 and the metal. Figure 8.11 shows XPS spectra for the different samples, with each spectrum normalized to the C 1s peak's position. The Mo 3d core level spectrum for the as-grown high- and low-quality MoS_2 films, in addition to the gold thin film interface samples, is shown in Figure 8.11 (a). A clear shift of 0.29 eV is observed in the 700 ^oC gold/MoS_2 spectrum, whereas both the as-grown films as well as the 900 ^oC MoS_2/gold spectra exhibit degenerate peak positions. Prior work has shown that a shift to lower binding energies in the Mo 3d spectrum indicates a partially covalent metal/MoS_2 interface[157]. A similar shift is observed in the 700 ^oC MoS_2/gold sample, indicating some amount of covalent bonding between gold and MoS_2, forming a partially covalent interface (a deviation from the expected van der Waals interaction). Similarly, a shift of 0.36 eV is observed in the S 2p spectrum for the 700 ^oC MoS_2/gold sample, whereas the as-grown films and the 900 ^oC MoS_2/gold sample again exhibit degenerate peak positions, observed in Figure 8.11 (b). This shift has also been previously observed as a result of increased covalent interaction between gold and sulfur atoms[284]. In Figure 8.11 (c), the Au 4f spectra for both MoS_2/gold interface samples are shown and compared to a standard gold reference spectrum. The 700 ^oC MoS_2/gold interface again exhibits a noticeable shift, this time manifesting in the Au 4f doublet position. This shift can also be attributed to a transition away from a van der Waals interaction and further supports the trend of a partially covalent gold/MoS_2 interface[284-285]. Notably, no such shifts are observed for the 900 ^oC MoS_{23}/gold interfaces for any of the

Mo 3d, S 2p, or Au 4f spectra; all differences in the peak positions of each respective spectra, compared to the reference samples, are less than 0.03 eV.

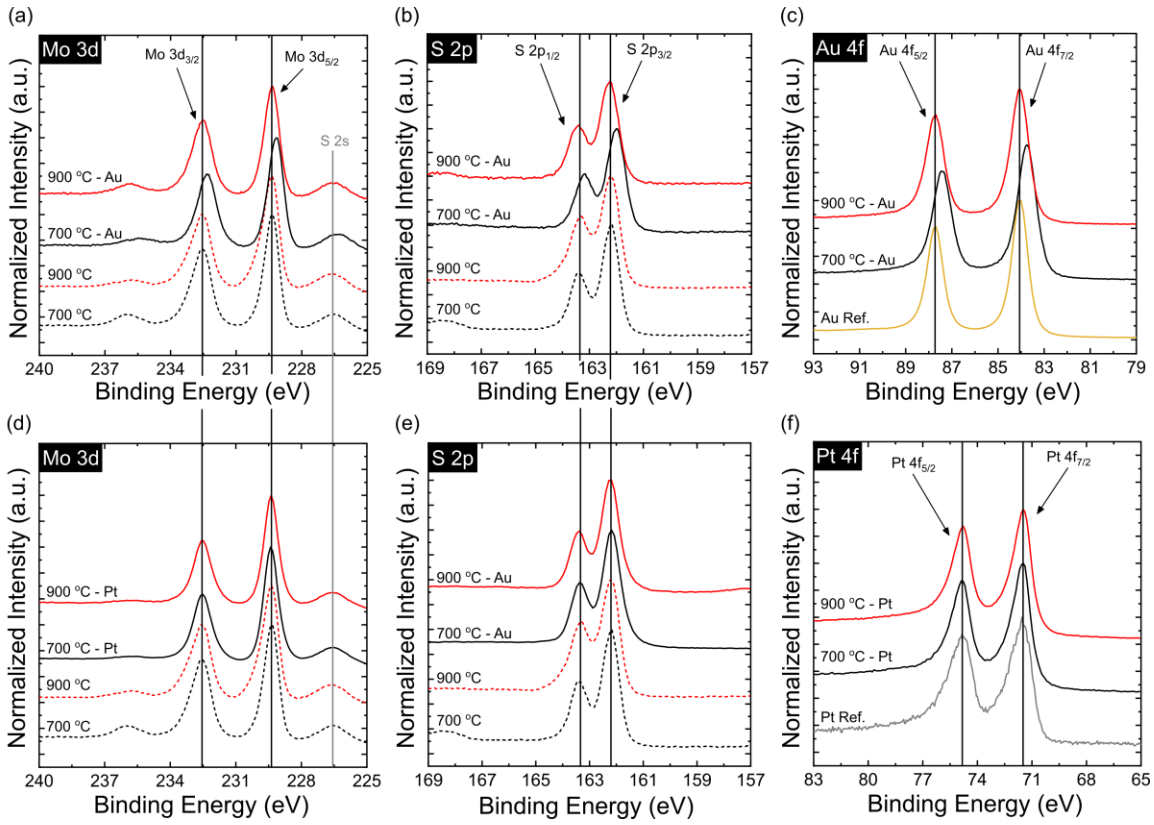

Figure 8.11. Mo 3d spectra for the MoS_2/Au (a) and MoS_2/Pt (d) interfaces, compared to the as-grown spectra (dashed lines). The MoS_2 Mo $3d^{3/2}$ and $3d^{5/2}$ peak positions are denoted by the black lines in (a,d), along with the S 2s peak by the gray line. (b,e) show the S 2p spectra for the MoS_2/ Au and MoS_2/Pt interfaces, respectively, compared to the as-grown spectra (dashed lines). S $2p^{1/2}$ and $2p^{3/2}$ are denoted by black lines. (c) shows the Au 4f core level spectra for the MoS_2/Au interfaces, compared to the bulk Au reference spectrum. Au $4f^{5/2}$ and $4f^{7/2}$ are denoted by black lines. (f) shows the Pt 4f core level spectra for the MoS_2/Au interfaces, compared to the bulk Pt reference spectrum. Pt $4f^{5/2}$ and $4f^{7/2}$ are denoted by black lines.

The observed strong interaction between the defective MoS_2 and gold can be explained by looking at an analogous system. A large amount of literature exists on the

interaction chemistry between sulfur and gold, particularly in the self-assembled monolayer (SAM) community[230, 286-289]. Specifically, in the context of SAMs, the sulfur-gold bond takes the form of a metal thiolate, which is extremely strong and yields a bond strength of approximately 44 kcal/mol[287]. Similarly, in a defective MoS_2 film comprising a high density of point defects and grain boundaries, sulfur atoms that do not have a full valence of electronic bonds to molybdenum can interact strongly with the adjacent gold film. This chemical interaction forms a covalent bridge between the gold and MoS_2, electrically coupling the two materials more strongly than a typical van der Waals interaction.

In Figure 8.11 (d,e), the Mo 3d and S 2p core level spectra are shown for both as-grown MoS_2 films as well as the 700 and 900 ^oC MoS_2/platinum interfaces. IN contrast to the 700 ^oC MoS_2/gold interface, platinum does not exhibit any core level shifts in either the Mo 3d or S 2p spectra, where any different in peak position is less than 0.04 eV. The lack of any observable shift in either spectrum suggests that the interface between platinum and MoS_2, both high and low qualities, remains predominantly van der Waals. One possible explanation is simply that platinum does not interact as strongly with sulfur as gold is known to, leading to a more inert interface. Figure 8.11 (f) shows the Pt 4f spectra for both MoS_2/'platinum interface samples as compares them to a platinum bulk reference sample. As in Figure 8.11 (d, e), no observable peak shift is detected, further supporting the conclusion that minimal covalent interaction occurred between platinum and MoS_2 of either quality.

The lack of interaction between platinum and both qualities of MoS_2 is in noticeable contrast to the case of defective MoS_2 in contact with gold. This result can also be explained

from the perspective of sulfur-based thiol SAM functionalization to platinum. Whereas the gold-sulfur interaction is strong and leads to a strong covalent interaction, sulfur thiols do not bond as strongly to platinum surfaces[290]. Specifically, sulfur-based thiols bonded to gold yield a single doublet contribution to the resulting S 2p XPS spectrum. In contrast, these thiols, when exposed to platinum surfaces, yield three different doublets in the resulting S 2p spectrum, indicating that a significant portion of the sulfur end groups did not functionalize to the platinum surface. The reduced functionalization percentage suggest that sulfur and platinum do not interact as covalently as sulfur and gold, which is consisted with our observed interfaces between MoS_2 contacted to gold and platinum.

These XPS results are consistent with the UPS data and calculated work functions for each interface. A strong core level shift is observed in all 700 ^oC MoS_2/gold spectra, which is in agreement with the reduction in the work function when gold contacts 700 ^oC MoS_2, as seen in Figure 8.9. The low-quality MoS_2 contains a high level of defect states, which offer sites for covalent bonding between MoS_2 and gold, resulting in a partial covalent interface. The increased covalency between MoS_2 and gold then leads to a strong interaction between the materials, leading to strong Fermi level pinning. This pinning then reduces the work function of gold, leading to an effective reduction of the SBH. In contrast, the 900 ^oC MoS_2 does not result in any noticeable covalent interaction via XPS core level shifts, which is consistent with the lack of observed pinning resulting in an unchanged gold work function. Similarly, the platinum/MoS_2 interfaces exhibit no core level shifts in the XPS spectra, suggesting minimal covalent interaction at the interface. The minimal interaction leads to a fixed amount of pinning due to MIGS, resulting in comparable work functions of platinum in contact with both high- and low-quality MoS_2.

8.6 Conclusion

In this study, the effect of MoS_2 material quality on Fermi level pinning was investigated, and an understanding of the relationship between wafer-scale material quality and effective contact metal work function was established. MoS_2 films of varying qualities were synthesized, and purely vertical heterostructure devices were fabricated using gold/gold and platinum/gold contracts. The temperature dependence of the devices was explored, and it was found that low-quality MoS_2 devices are dominated by a temperature-independent injection mechanism. FN plots revealed that the FN threshold voltage is temperature-dependent for the 900 ^oC MoS_2 device but independent for the 700 ^oC MoS_2 devices. Device modeling was performed to verify the injection mechanisms, which demonstrated good agreement between the experimental and theoretical behaviors. Additionally, effective barrier heights were extracted from the device models, which revealed that low-quality MoS_2 strongly pins gold and reduces the SBH at the interface. Pinning that results in low barrier heights leads to temperature independent injection, where FN tunneling dominates injection regardless of measurement temperature. Asymmetric devices were used to realize that high-quality MoS_2 does not result in asymmetric *I-V* behavior. In contrast, low-quality asymmetric MoS_2 devices do exhibit an asymmetric *I-V* relationship and yield different FN threshold voltages for gold and platinum injection, suggesting different barrier heights at each interface. UPS was performed to calculate the effective work function of each interface, which revealed that 700 ^oC MoS_2 pins the gold's work function strongly to low energy values, whereas platinum remains relatively unaffected. Additionally, the measured change in the gold's work function when in contact with the 700 ^oC MoS_2 showed good agreement with the extracted SBH change found from

modeling the symmetric device behavior. XPS measurements confirm the increased covalency between gold and low-quality MoS_2 and show minimal covalent interaction between both MoS_2 films and the platinum metal.

This work demonstrated the relevance of MoS_2 material quality on Fermi level pinning. Using cross-point device architecture, the relationship between the macroscopic material quality and the strength of Fermi level pinning was demonstrated, and various characterization techniques were used to investigate the physical mechanisms that lead to the increased pinning strength. These experiments shed light on the impact of material quality on a large scale in purely vertical heterostructure device performance and provide insight on material requirements for successful heterostructure device construction and operation.

CHAPTER 9. SUMMARY AND FUTURE WORK

9.1 Summary

2D materials are of interest for a variety of next generation electronic device architectures. The various architectures can be utilized for numerous applications, including flexible electronics, high performance digital electronics, memory select devices, and a variety of sensing applications. In particular, 2D heterostructure architectures are of significant interest due to the lack of out-of-plane bonds that these material exhibit, enabling arbitrary stacking arrangement of these films. However, to successfully incorporate 2D materials into BEOL CMOS processes, a process for synthesizing these materials at low temperatures is a critical requirement. Additionally, the ability to synthesize TMD films onto arbitrary substrates is required to enable layer-by-layer fabrication of heterostructures, eliminating the effect of transfer steps that contaminate the interfaces between each layer. However, low temperature synthesis restrictions will likely yield defective material; consequently, understanding the effects of defects and lower film quality on resulting device performance is critical for TMD implementation in various device applications.

As such, this work involved the development of a low-temperature synthesis technique for MoS_2. By using a H_2S plasma, the temperature required for the thin film sulfurization reaction of molybdenum initial films is significantly reduced, where synthesis is successfully achieved on SiO_2 substrates at temperatures as low as 400 ^oC. Utilizing an MBE chamber that houses both molybdenum and sulfur precursors *in situ*, a fundamental

investigation of the thin film reaction process was also performed. MoO_3 was found to be more reactive with H_2S than metallic Mo initial films, consistent with thermodynamic calculations found in literature. However, metallic Mo initial films were found to yield higher quality resulting MoS_2. In addition, synthesis via cyclic layer-by-layer growth enables strong thickness control and high uniformity across large scale. However, the in-plane conductivity of the film is dominated by variable range hopping, which was confirmed to be due to the nanocrystallinity of the film.

The low-temperature synthesis was then ported to gold substrates. Interestingly, metallic molybdenum initial films yield minimal conversion when using gold substrates. Conversely, oxidizing each deposition to MoO_3 yields nearly stoichiometric MoS_2. A strong substrate dependence implies increased import of thermodynamics of the sulfurization reaction, in order to aid the sulfurization of molybdenum and quench the gold/sulfur interaction. The resulting MoS_2 films synthesized on gold are lower in quality than corollary films synthesized on SiO_2, most likely due to the required oxidization step, although successful low temperature synthesis on gold substrates was nevertheless achieved.

With synthesis on gold substrates achieved, direct layer-by-layer heterostructure fabrication is possible. Metal/MoS_2/metal heterostructures yield ohmic behavior, indicating that the low film quality strongly influences device performance and influences device operation predicated on injection at the metal/semiconductor interface. However, these metal/MoS_2/metal heterostructures do exhibit switching behavior, yielding a switching window comparable with memristive MoS_2 devices found in literature. Introducing a tunneling barrier to the heterostructure forces tunneling from one MoS_2

electrode to an opposite MoS_2 film. Although the device is symmetric in nature, no evidence of NDR is observed, again likely attributed to the low film quality increasing scattering and eliminating momentum conservative tunneling. Nevertheless, both heterostructures indicate that the poor in-plane conduction can be circumvented by intelligent device architecture design.

Two different heterostructure architectures were exposed to ionizing radiation to induce defects into the structure. These defects were then correlated to changes in resulting device behavior. Passivated graphene FETs were exposed to increasing doses of X-ray irradiation, which resulting in doping and device degradation. $1/f$ noise measurements were used to ascertain the defect energies that arose as a result of irradiation. Correlating DFT calculations to device characteristics yield that hydrogen impurities and oxygen complexes at the graphene/insulator layer contribute to doping and scattering, shifting the threshold voltage and decreasing mobility. This degradation can be reversed by high temperature anneals, indicating that no permanent damage is done to the film. Nevertheless, these results clearly indicate that any disorder at the 2D/insulator interface strongly impacts device performance.

In contrast, the MoS_2/high-k dielectric/MoS_2 tunnel junctions exhibited X-ray irradiation resistance. High energy proton irradiation was therefore used to induce defects in the heterostructure. Two high-k dielectric interlayers were investigated, Al_2O_3 and HfO_2, due to their differing work functions and oxidation states. When exposed to increasing fluences of protons, the Al_2O_3 interlayer devices exhibited a shift in FN threshold voltage, whereas the HfO_2 devices did not. DFT calculations revealed that passivated oxygen vacancies in Al_2O_3 introduce defect sites that lie close in energy space to the MoS_2

conduction band, leading to variable range hopping across the interlayer; neither passivated or depassivated oxygen vacancies contribute relevant defect energies in HfO_2, corroborating the lack of radiation response. As such, selectively choosing complementary materials is crucial for negating potential defect effects in these heterostructure devices.

The low temperature MoS_2 synthesis technique discussed in CHAPTER 4 was ported to WS_2 synthesis, permitting WS_2 synthesis at 400 ^oC. As such, MoS_2/WS_2 heterostructures were directly synthesized onto SiO_2 substrates; the synthesis order and resulting heterostructure orientation did not noticeably effect film quality. In the heterostructures consisting of 3-layer MoS_2 and 3-layer WS_2, interlayer interactions were found to modify each material's electronic structure. Despite the structure consisting of two 3-layer films, the two materials' electronic structure shifts and behaves as if each material was ~5 layers. This interaction is likely due to the similarities between the MoS_2 and WS_2 crystal structures. XPS depth profiling reveal that the sputter-based synthesis introduces transition metal intermixing, which reduces the order of the MoS_2/WS_2 interface. Purely vertical MoS_2/WS_2 heterostructures do not exhibit rectification, and also result in symmetric *I-V* characteristics in both negative and positive bias regimes. Strong Fermi level pinning effects result in direct electron injection into the MoS_2 conduction band, which also aligns with the opposite gold contact's work function, yielding symmetric tunneling behavior across the WS_2 layers.

The MoS_2/metal interface was also explored to understand the effect of wafer-scale material quality on resulting Fermi level pinning strength. Purely vertical symmetric and asymmetric MoS_2 heterostructures were fabricated form high and low quality MoS_2 films to explore the gold/MoS_2 and platinum/MoS_2 interfaces. Device behavior was modelled to

obtain the effective barrier height of each interface, which was verified using XPS and UPS physical characterization. Notably, an inherent amount of pinning was found to be present for all four interfaces, indicating an inherent amount of defect-independent pinning, likely due to MIGS. However, gold was found to covalently interact with defective MoS_2, resulting in strong pinning effects that reduce the effective barrier height. Because platinum does not exhibit a stronger covalent interaction with defective MoS_2, it is less susceptible to pinning effects.

9.2 Future Work

This thesis laid the groundwork for integrating 2D vertical heterostructures into existing BEOL processes by the realization of a large-area, uniform synthesis process that can be performed at low temperatures. In addition, the influence of both as-synthesized and radiation-induced defects on device performance were explored, revealing that the low temperature synthesized materials introduce significant defect-related layer-layer interactions, degrading device performance. As such, a significant amount of optimization in synthesis and fabrication of these heterostructures that must be performed.

Although low temperature synthesis was successfully achieved, the resulting material quality significantly hindered device performance. Specifically, the in-lane conduction through the films is dominated by variable range hopping. As such, any device architecture that requires in-plane conduction will likely be dominated by this hopping conduction as opposed to the desired operational principle. Additionally, achieving device applications that require specific performance metrics such as steep slope operation and

NDR will require higher quality synthesized films. Therefore, improving synthesis to yield higher quality films is important. This can be achieved by further balancing the H_2S plasma soak step, namely optimizing the plasma power and soak duration used. In addition, further exploring the cyclic nature of the synthesis may yield higher quality grains, where sub-monolayer cycles may promote grain growth and shift the synthesis from a nucleation dominated process.

As a part of synthesis optimization, further substrates should be explored for the low temperature synthesis process. While SiO_2, high-k dielectrics, and gold substrates were explored, the effect of synthesis on additional substrates should be investigated. Other metal (e.g. titanium, platinum, copper, etc.) and insulating (e.g. sapphire, other amorphous oxides, etc.) should be explored in higher detail. Specifically, the influences on substrate on resulting crystallinity of the TMD films should be explored, in order to determine the extent of epitaxy that dictates the low temperature synthesis process.

Once synthesis is further optimized, heterostructures that involve lateral transport can also be explored. By including lateral transport, the individual 2D layers can be electrostatically doped via application of a gate bias, enabling more fine control on resulting device performance. However, the photolithographic techniques required to fabricate heterostructures with lateral conduction would require careful consideration in order to limit the overlap between the two 2D electrodes. As such, transfer techniques may be required initially to explore more complex heterostructures, meaning the cleaning process of transferred 2D layers must be optimized and carefully performed.

In conjunction with synthesis optimization, the development of selenide TMDs such as $MoSe_2$ and WSe_2 is crucial for realizing more complex heterostructure stacks. In particular, the chalcogen intermixing in dissimilar chalcogen layers during synthesis can be mitigated by synthesizing the layers at low temperatures. As such, fabricating sulfide/selenide heterostructures enables a broad range of hypotheses to investigate. The synthesis of selenides can be achieved using similar plasma-assisted techniques, although more conventional MBE techniques for selenides have been demonstrated at relatively low temperatures in the literature. As such, an e-beam evaporator was ported to the MBE system in order to enable future experiments on slower synthesis of TMD films, in particular selenides. By thermally effusion selenium at a high flux and co-depositing a low-flux of transition metal via e-beam evaporation, individual grains of selenide TMDs can be obtained. This opens possibilities for combining plasma-assisted techniques with e-beam techniques, which can be used to explore the efficacy of a joint synthesis method. This technique also appears to be crucial for synthesizing TMD/TMD heterostructures with atomically sharp interfaces, as sputter-based synthesis techniques appear to introduce transition metal intermixing that inhibits the formation of well-defined heterostructure interfaces.

When more sophisticated heterostructures are realized, further radiation hardness studies would be valuable to ascertain the sensitivity of the devices. As the predominant radiation effects observed in this thesis pertained to the interface between the 2D material and surrounding insulator, it is possible that with higher quality initial materials defects may be introduced into the 2D film itself. Therefore, investigating what additional steps

need to be taken to insure radiation resistance is important to utilize these materials in radiation heavy environments.

Last, further exploring pinning effects at the TMD/metal interface would be valuable to explore the limitation of the low temperature synthesized material. The results discussed in this work demonstrate that defect effects significantly modify the interlayer interactions between TMDs and adjacent materials, which in turn alter device characteristics. As the pinning effects explored in this work only involved high temperature synthesized films, performing an explicit Fermi level pinning study on materials synthesized at 400 ^{o}C would yield valuable information on the saturation of pinning effects with respect to material quality. In addition, exploring different metals with low work functions may yield information on how to obtain an ohmic contact to TMDs. However, because low work function metals commonly oxidize rapidly in air, a sophisticated vacuum system with *in situ* characterization methods would likely be required.

APPENDIX A. EXPERIMENTAL BACKROUND

This chapter outlines the experimental systems used for material synthesis and characterization of the 2D films used in this work. The first section of this chapter describes the tube furnaces and MBE tools used for graphene and TMD synthesis techniques. The second section of this chapter overviews the equipment used for physical and electrical characterization of the 2D films and devices.

A.1 Synthesis Systems

A.1.1 Molecular Beam Epitaxy

An MBE tool was used for the low-temperature and heterostructure TMD syntheses. The base pressure of the system is on the order of 10^{-9}. Up to eight molecular sources can be utilized in the system, allowing for various 2D layers to be synthesized in conjunction with one another. Isolation of the different sources is achieved using a wagon wheel cooled using chilled water at a temperature of 8 ^{o}C. Each molecular beam has a shutter which can be used to interrupt the flow of individual sources during growth while maintaining the source's run state. In this work, the MBE utilizes two sputter guns for Mo and W sputtering, a gas injector for argon flow during sputter processes, and a direct plasma source used for H_2S plasma exposure. A schematic of the system is shown in Figure A.1. The sample is mounted on a rotating assembly which has an ion gauge mounted opposite the sample. This gauge enables flux measurements of precursor flows when compared to a

background ion gauge mounted at the rear of the chamber (not shown). Also not shown is a liquid nitrogen cryo shroud, which is used to freeze out atmospheric species and further reduce chamber pressure.

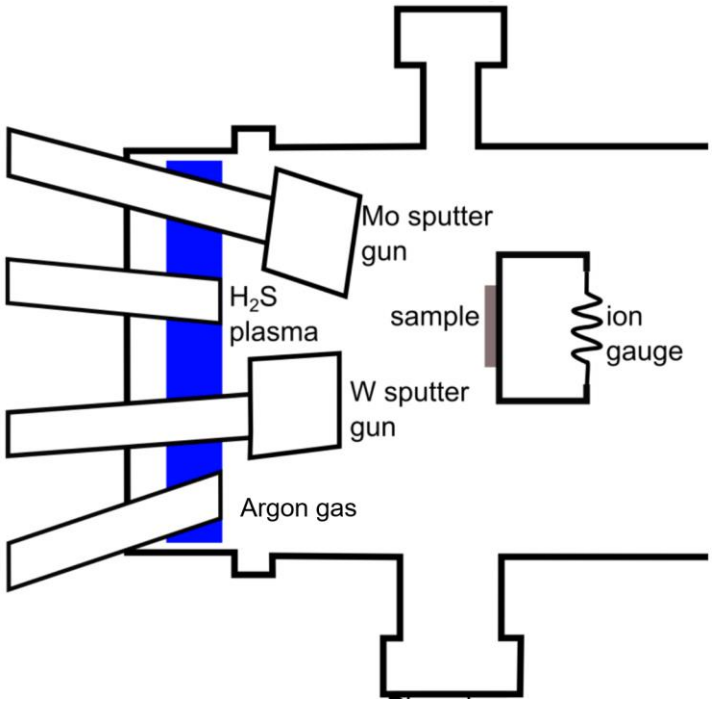

Figure A.1. Schematic of the MBE system used for low-temperature TMD synthesis. Reprinted with permission from Campbell, P.; Perini, C.; Chiu, J.; Gupta, A.; Ray, H. S.; Chen, H.; Wenzel, K.; Snyder, E.; Wagner, B. K.; Ready, J.; Vogel, E. M., Plasma-Assisted Synthesis of MoS_2. *2D Materials* 2018, *5* (1), 015005-2.

To perform synthesis, the sample is mounted to a transfer arm located in the load lock of the system. The load lock is evacuated, and the sample is transferred and mounted to the rotating assembly in the chamber. Sample temperature is raised using a Veeco VA-2-SSH substrate heater to the desired synthesis temperature. Samples were exposed to an H_2S plasma to clean the surface of residues, unless otherwise stated. When synthesis is completed, the sample is cooled in vacuum until 200 ^oC, where it is moved to the load lock

and cooled to room temperature under nitrogen flow, at which point the sample is removed from the load lock.

Of note, an e-beam evaporator was installed into a vacant precursor port to enable future investigation of slower synthesis processes. In particular, slowing synthesis by e-beam evaporating the transition metal in a chalcogen rich environment, as opposed to sputtering and subsequent soaking, has been demonstrated in literature to yield individual high quality TMD flakes[77]. A rod of source metal was loaded into the precursor port, which is thermally heated via electron emission from a nearby filament. A low flux of evaporated metal would be delivered in conjunction with a relatively high chalcogen flux from a thermal effusion cell. However, as the melting temperature of tungsten and molybdenum is rather high, successful evaporation of the transition metal has been a challenging process, and therefore no relevant data from e-beam synthesis was included in this thesis.

A.1.1 High Temperature Tube Furnaces

Two furnaces were utilized for synthesis of 2D materials in this work. The first system is a CVD Equipment (Central Islip, NY) tube furnace used for experiments involving sulfurization of metallic films. The sample to be sulfurized is placed on a graphite stage close to the contact point of a thermocouple, used to monitor stage temperature. The chamber is heated by infrared bulbs, which reaches a maximum temperature of 950 ^{o}C. Gas sources for argon, hydrogen, and methane are plumbed to the system, with mass flow controllers in-line to provide variable flow rate control of each gas source. Sulfur is provided as a powder, where a quartz crucible filled with 50 mg of S powder (Sigma-

Aldrich) and placed directly onto the stage. Once the sample is loaded into the chamber, the chamber was evacuated to a base pressure of 10^{-6} Torr and then backfilled with argon to 5 Torr. The chamber is then sealed, and the temperature is increased to the desired synthesis temperature and held for 1 hour. After synthesis, the chamber is cooled to room temperature under argon flow, after which the sulfurized sample is removed from the furnace.

The second tube furnace system used in this work is a CVD FirstNano EasyTube 3000 advanced CVD system, which was used for graphene synthesis. Graphene was synthesized on 25 μm thick 99.98% copper foils (Alfa Aesar), which was placed in glacial acetic acid for one minute and rinsed with deionized water prior to being loaded into the Furnace's load lock. Once the foil is loaded into the load lock, the load lock was evacuated to 20 mTorr then backfilled with argon. The copper foil was then loaded into the quartz chamber, which is evacuated to 10^{-6} Torr prior to starting the synthesis process. After base pressure is reached, the chamber is heated using infrared bulbs to 1000 ^{o}C under constant argon/hydrogen flow of 200/15 sccm to a pressure of 250 mTorr. The foil is held at 1000 ^{o}C in the argon/hydrogen flow for 10 minutes to anneal the foil. After annealing, the argon flow is turned off and methane is introduced into the chamber at 45 sccm while maintaining a chamber pressure of 250 mTorr. This environment is held for 6 hours to allow the graphene film to nucleate and coalesce into a uniform film. After synthesis, the furnace was cooled to room temperature under argon flow, after which the foil is moved from the furnace to the load lock, which is then vented to atmosphere with argon.

A.2 Characterization Techniques

A.2.1 Physical Characterization Methods

Raman measurements were performed using a Renishaw InVia microRaman system with a 488 nm Ar+ laser with a 0.25 m focal length spectrometer. Raman and photoluminescence (PL) measurements were performed through a 50x objective in the 180 back-scattered configuration, 3000 grooves/mm^{-1} for the 488 nm line. Spectra were captured using a front side illuminated CCD camera with a spectral resolution less than 1 cm^{-1}/pixel. Spectra intensities were normalized to the Si-Si phonon mode at 520 cm^{-1}. Spectral analysis was performed manually.

Photoluminescence measurements were performed using the same Renishaw InVia microRaman system. The 50x objection in the 180 back-scattered configuration was used, with a grating of 1200 grooves/mm^{-1} for the 532 nm line.

X-ray photoelectron spectroscopy was performed using a Thermo Scientific K-alpha XPS system. This system has a monochromated aluminum Kα X-ray source and a hemispherical analyzer. Measurements were performed using constant analyzer energy mode with 50 eV pass energy and 0.1 eV step size and a 400 μm spot size. Analysis was performed using XPSPeak analysis software.

UPS was performed using a Kratos Axis Ultra DLD XPS/UPS system using a He II source lamp. A pass energy of 10 eV was used in the constant analyzer energy mode, with a 50 μm spot size and a 0.05 eV step size. A sample bias of -8.79 V was applied to

keep the Fermi energy at 0 eV. At least 10 spectra were measured for each sample, and the calculated work functions were averaged and statistically plotted.

Atomic force microscopy was performed with a Veeco Dimension 3100 scanning probe microscope. AppNano SPM silicon cantilevers coated with Al on the reflex side with a pyramidal silicon tip of 1-2 nm radius and a spring constant of 37 N/m were used for imaging. All topographic images were acquired in tapping mode with a tip velocity less than 6 μm/s. AFM scan data was analyzed using Gwyddion analysis software. RMS roughness values were calculated from the entire scan area unless otherwise noted.

STEM imaging was performed using a Hitachi 2700 aberration corrected STEM using an 80 kV accelerating voltage at 10 μA of current.

A.2.2 Electrical Characterization Methods

Electrical measurements were conducted using a Keithley 4200-SCS semiconductor parameter analyzer. A lakeshore TTPX cryogenic probe station was used for all vacuum and temperature-dependent measurements. Liquid nitrogen was used to cool the probe station to temperatures down to 77 K, and a Lakeshore 336 temperature controller was used to regulate the measurement temperature. Electrical measurements were also conducted using a Cascade summit 12000 semi-automatic probe station. Measurements performed in the Cascade probe station were conducted under a constant flow of nitrogen at room temperature and ambient pressure. Measurements conducted in vacuum were annealed at 80 ^{o}C for 12 hours prior to the measurement to remove residual contaminants and adsorbates from the environment.

The electrical properties of the graphene films discussed in CHAPTER 3 were extracted using a constant mobility model developed by Kim et al[203]. The resistance of the graphene at a fixed drain bias is measured as a function of gate voltage, and can be modeled as

$$R_{tot} = R_{con} + \frac{N_{sq}}{e\mu\sqrt{n_0^2 + n_{ind}^2}} \quad \textbf{A.1}$$

where R_{tot} is the total resistant, R_{con} is the contact resistance, N_{sq} is the number of squares, n_o is the intrinsic carrier concentration, n_{ind} is the induced carrier concentration from the applied gate bias, and μ is the mobility. The induced carrier concentration can be determined from device parameters[203]. The total resistance is then modelled as functions of R_{con}, n_o, μ, and the Dirac point of the graphene transistor. A least squares approach is used to minimize the error between the measured behavior and modeled resistance, yielding the graphene film's mobility.

Device modeling of the FN plot behavior discussed in CHAPTER 8 was performed using literature values for electron effective mass and Schottky barrier width[275, 291]. A fixed offset was applied to the FN and TE calculations to account for the device area, and the offset was held constant for all modeled junctions, with only the effective barrier height being allowed to change. Other potential explanations for the offset include experimental error such as transfer residues. These experimental errors would be consistent across all samples and measurements, which may explain the fixed offset applied to all modeled curves.

CHAPTER 10. REFERENCES

1. Cheng, R.; Jiang, S.; Chen, Y.; Liu, Y.; Weiss, N.; Cheng, H. C.; Wu, H.; Huang, Y.; Duan, X. F., Few-layer molybdenum disulfide transistors and circuits for high-speed flexible electronics. *Nature Communications* **2014,** *5*.

2. Akinwande, D.; Petrone, N.; Hone, J., Two-dimensional flexible nanoelectronics. *Nature Communications* **2014,** *5*, 5678.

3. Chang, H.-Y.; Yang, S.; Lee, J.; Tao, L.; Hwang, W.-S.; Jena, D.; Lu, N.; Akinwande, D., High-Performance, Highly Bendable MoS2 Transistors with High-K Dielectrics for Flexible Low-Power Systems. *ACS Nano* **2013,** *7* (6), 5446-5452.

4. Kim, S. J.; Choi, K.; Lee, B.; Kim, Y.; Hong, B. H., Materials for Flexible, Stretchable Electronics: Graphene and 2D Materials. *Annu Rev Mater Res* **2015,** *45*, 63-84.

5. Pu, J.; Yomogida, Y.; Liu, K. K.; Li, L. J.; Iwasa, Y.; Takenobu, T., Highly Flexible MoS2 Thin-Film Transistors with Ion Gel Dielectrics. *Nano Lett.* **2012,** *12* (8), 4013-4017.

6. Kim, B. J.; Jang, H.; Lee, S. K.; Hong, B. H.; Ahn, J. H.; Cho, J. H., High-Performance Flexible Graphene Field Effect Transistors with Ion Gel Gate Dielectrics. *Nano Lett.* **2010,** *10* (9), 3464-3466.

7. Massicotte, M.; Schmidt, P.; Vialla, F.; Schadler, K. G.; Reserbat-Plantey, A.; Watanabe, K.; Taniguchi, T.; Tielrooij, K. J.; Koppens, F. H. L., Picosecond photoresponse in van der Waals heterostructures. *Nature Nanotechnology* **2016,** *11* (1), 42-46.

8. Wang, Q. H.; Kalantar-Zadeh, K.; Kis, A.; Coleman, J. N.; Strano, M. S., Electronics and optoelectronics of two-dimensional transition metal dichalcogenides. *Nature Nanotechnology* **2012,** *7* (11), 699-712.

9. Zhang, W.; Chuu, C.-P.; Huang, J.-K.; Chen, C.-H.; Tsai, M.-L.; Chang, Y.-H.; Liang, C.-T.; Chen, Y.-Z.; Chueh, Y.-L.; He, J.-H.; Chou, M.-Y.; Li, L.-J., Ultrahigh-Gain Photodetectors Based on Atomically Thin Graphene-MoS2 Heterostructures. *Scientific Reports* **2014,** *4*.

10. Zhou, X.; Zhou, N.; Li, C.; Song, H. Y.; Zhang, Q.; Hu, X. Z.; Gan, L.; Li, H. Q.; Lu, J. T.; Luo, J.; Xiong, J.; Zhai, T. Y., Vertical heterostructures based on SnSe2/MoS2 for high performance photodetectors. *2d Materials* **2017,** *4* (2), 025048.

11. Konstantatos, G.; Badioli, M.; Gaudreau, L.; Osmond, J.; Bernechea, M.; de Arquer, F. P. G.; Gatti, F.; Koppens, F. H. L., Hybrid graphene-quantum dot phototransistors with ultrahigh gain. *Nature Nanotechnology* **2012,** *7* (6), 363-368.

12. Jeong, H.; Bang, S.; Oh, H. M.; Jeong, H. J.; An, S. J.; Han, G. H.; Kim, H.; Kim, K. K.; Park, J. C.; Lee, Y. H.; Lerondel, G.; Jeong, M. S., Semiconductor-Insulator-Semiconductor Diode Consisting of Monolayer MoS2, h-BN, and GaN Heterostructure. *ACS Nano* **2015,** *9* (10), 10032-10038.

13. Hong Qiao, J. Y., Broadband Photodetector Based on Graphene-Bi2Te3 Heterostructure. *ACS Nano* **2015,** *9* (2).

14. Xia, F.; Mueller, T.; Lin, Y.-m.; Valdes-Garcia, A.; Avouris, P., Ultrafast graphene photodetector. *Nature Nanotechnology* **2009,** *4* (12), 839-843.

15. Tsai, M.-Y.; Tarasov, A.; Hesabi, Z. R.; Taghinejad, H.; Campbell, P. M.; Joiner, C. A.; Adibi, A.; Vogel, E. M., Flexible MoS2 Field-Effect Transistors for Gate-Tunable Piezoresistive Strain Sensors. *ACS Appl. Mater. Interfaces* **2015,** *7* (23), 12850-12855.

16. He, Q.; Zeng, Z.; Yin, Z.; Li, H.; Wu, S.; Huang, X.; Zhang, H., Fabrication of Flexible MoS2 Thin-Film Transistor Arrays for Practical Gas-Sensing Applications. *Small* **2012,** *8* (19), 2994-2999.

17. Liu, B.; Chen, L.; Liu, G.; Abbas, A. N.; Fathi, M.; Zhou, C., High-Performance Chemical Sensing Using Schottky-Contacted Chemical Vapor Deposition Grown Monolayer MoS2 Transistors. *ACS Nano* **2014,** *8* (5), 5304-5314.

18. Huang, B.; Li, Z.; Liu, Z.; Zhou, G.; Hao, S.; Wu, J.; Gu, B.-L.; Duan, W., Adsorption of gas molecules on graphene nanoribbons and its implication for nano-scale molecule sensor. *arXiv:0803.1516 [cond-mat]* **2008**.

19. Geim, A. K.; Grigorieva, I. V., Van der Waals heterostructures. *Nature* **2013,** *499* (7459), 419-425.

20. Novoselov, K. S.; Jiang, D.; Schedin, F.; Booth, T. J.; Khotkevich, V. V.; Morozov, S. V.; Geim, A. K., Two-dimensional atomic crystals. *Proc Natl Acad Sci U S A* **2005,** *102* (30), 10451-10453.

21. Zhang, F.; Zhu, Y. Q.; Appenzeller, J., Novel Two-Terminal Vertical Transition Metal Dichalcogenide Based Memory Selectors. *Ieee Device Res Conf* **2017**.

22. Campbell, P. M.; Smith, J. K.; Ready, W. J.; Vogel, E. M., Material Constraints and Scaling of 2-D Vertical Heterostructure Interlayer Tunnel Field-Effect Transistors. *Ieee T Electron Dev* **2017,** *64* (6), 2714-2720.

23. Sarkar, D.; Xie, X.; Liu, W.; Cao, W.; Kang, J.; Gong, Y.; Kraemer, S.; Ajayan, P. M.; Banerjee, K., A subthermionic tunnel field-effect transistor with an atomically thin channel. *Nature* **2015,** *526* (7571), 91-95.

24. Yan, X.; Liu, C.; Li, C.; Bao, W.; Ding, S.; Zhang, D. W.; Zhou, P., Tunable SnSe2/WSe2 Heterostructure Tunneling Field Effect Transistor. *Small*, n/a-n/a.

25. Campbell, P. M.; Tarasov, A.; Joiner, C. A.; Ready, W. J.; Vogel, E. M., Enhanced Resonant Tunneling in Symmetric 2D Semiconductor Vertical Heterostructure Transistors. *ACS Nano* **2015,** *9* (5), 5000-5008.

26. Britnell, L.; Gorbachev, R. V.; Geim, A. K.; Ponomarenko, L. A.; Mishchenko, A.; Greenaway, M. T.; Fromhold, T. M.; Novoselov, K. S.; Eaves, L., Resonant tunnelling and negative differential conductance in graphene transistors. *Nature Communications* **2013,** *4*, 1794.

27. Burg, G. W.; Prasad, N.; Fallahazad, B.; Valsaraj, A.; Kim, K.; Taniguchi, T.; Watanabe, K.; Wang, Q.; Kim, M. J.; Register, L. F.; Tutuc, E., Coherent Interlayer Tunneling and Negative Differential Resistance with High Current Density in Double Bilayer Graphene–WSe2 Heterostructures. *Nano Lett.* **2017,** *17* (6), 3919-3925.

28. Roy, T.; Tosun, M.; Hettick, M.; Ahn, G. H.; Hu, C. C.; Javey, A., 2D-2D tunneling field-effect transistors using WSe2/SnSe2 heterostructures. *Applied Physics Letters* **2016,** *108* (8), 083111.

29. Clauss, F. J., *Solid Lubricants and Self-Lubricating Solids*. Academic Press: 111 Fifth Avenue, New York, New York 10003, 1972.

30. Tatar, R. C.; Rabii, S., Electronic-Properties of Graphite - a Unified Theoretical-Study. *Phys. Rev. B* **1982,** *25* (6), 4126-4141.

31. Spain, I. L.; Ubbelohde, A. R.; Young, D. A., Electronic Properties of Well Oriented Graphite. *Philos T R Soc S-A* **1967,** *262* (1128), 345-+.

32. Conan, A.; Bonnet, A.; Amrouche, A.; Spiesser, M., Semiconducting Properties and Band-Structure of Mote2 Single-Crystals. *J Phys-Paris* **1984,** *45* (3), 459-465.

33. Upadhyayula, L. C.; Loferski, J. J.; Wold, A.; Giriat, W.; Kershaw, R., Semiconducting Properties of Single Crystals of N and P-Type Tungsten Diselenide (Wse2). *Journal of Applied Physics* **1968,** *39* (10), 4736-+.

34. Boehm, H. P.; Setton, R.; Stumpp, E., Nomenclature and Terminology of Graphite-Intercalation Compounds. *Carbon* **1986,** *24* (2), 241-245.

35. Wallace, P. R., The Band Theory of Graphite. *Phys. Rev.* **1947,** *71* (9), 622-634.

36. Novoselov, K. S.; Geim, A. K.; Morozov, S. V.; Jiang, D.; Zhang, Y.; Dubonos, S. V.; Grigorieva, I. V.; Firsov, A. A., Electric Field Effect in Atomically Thin Carbon Films. *Science* **2004,** *306* (5696), 666-669.

37. Kang, S.; Fallahazad, B.; Lee, K.; Movva, H.; Kim, K.; Corbet, C. M.; Taniguchi, T.; Watanabe, K.; Colombo, L.; Register, L. F.; Tutuc, E.; Banerjee, S. K., Bilayer Graphene-Hexagonal Boron Nitride Heterostructure Negative Differential Resistance Interlayer Tunnel FET. *IEEE Electron Device Letters* **2015,** *36* (4), 405-407.

38. Radisavljevic, B.; Radenovic, A.; Brivio, J.; Giacometti, V.; Kis, A., Single-layer MoS2 transistors. *Nature Nanotechnology* **2011,** *6* (3), 147-150.

39. Novoselov, K. S.; Mishchenko, A.; Carvalho, A.; Neto, A. H. C., 2D materials and van der Waals heterostructures. *Science* **2016,** *353* (6298).

40. Duerloo, K. A. N.; Li, Y.; Reed, E. J., Structural phase transitions in two-dimensional Mo- and W-dichalcogenide monolayers. *Nature Communications* **2014,** *5*.

41. Brown, B. E., Crystal Structures of Wte2 and High-Temperature Mote2. *Acta Crystallogr* **1966,** *20*, 268-&.

42. Riflikova, M.; Martonak, R.; Tosatti, E., Pressure-induced gap closing and metallization of MoSe2 and MoTe2. *Phys. Rev. B* **2014,** *90* (3).

43. Kolobov, A. V.; Fons, P.; Tominaga, J., Electronic excitation-induced semiconductor-to-metal transition in monolayer MoTe2. *Phys. Rev. B* **2016,** *94* (9).

44. Gabuda, S. P.; Kozlova, S. G.; Ryzhikov, M. R.; Fedorov, V. E., Transition from 2-D Semiconductor to 1-D Metal State and Electron Density Distribution in Nanolayered MoX2 (X = S, Se, Te). *J Phys Chem C* **2012,** *116* (38), 20651-20655.

45. Ma, Y. G.; Liu, B. L.; Zhang, A. Y.; Chen, L.; Fathi, M.; Shen, C. F.; Abbas, A. N.; Ge, M. Y.; Mecklenburg, M.; Zhou, C. W., Reversible Semiconducting-to-Metallic Phase Transition in Chemical Vapor Deposition Grown Mono layer WSe2 and Applications for Devices. *ACS Nano* **2015,** *9* (7), 7383-7391.

46. Kuc, A.; Zibouche, N.; Heine, T., Influence of quantum confinement on the electronic structure of the transition metal sulfide TS2. *Phys. Rev. B* **2011,** *83* (24).

47. Han, S. W.; Kwon, H.; Kim, S. K.; Ryu, S.; Yun, W. S.; Kim, D. H.; Hwang, J. H.; Kang, J. S.; Baik, J.; Shin, H. J.; Hong, S. C., Band-gap transition induced by interlayer van der Waals interaction in MoS2. *Phys. Rev. B* **2011,** *84* (4).

48. Eda, G.; Yamaguchi, H.; Voiry, D.; Fujita, T.; Chen, M.; Chhowalla, M., Photoluminescence from Chemically Exfoliated MoS2. *Nano Lett.* **2011,** *11* (12), 5111-5116.

49. Zeng, H. L.; Liu, G. B.; Dai, J. F.; Yan, Y. J.; Zhu, B. R.; He, R. C.; Xie, L.; Xu, S. J.; Chen, X. H.; Yao, W.; Cui, X. D., Optical signature of symmetry variations and spin-valley coupling in atomically thin tungsten dichalcogenides. *Scientific Reports* **2013,** *3*.

50. Cooper, D. R.; D'Anjou, B.; Ghattamaneni, N.; Harack, B.; Hilke, M.; Horth, A.; Majlis, N.; Massicotte, M.; Vandsburger, L.; Whiteway, E.; Yu, V., Experimental Review of Graphene. *International Scholarly Research Notices* **2012,** *2012*, e501686.

51. Katsnelson, M. I., Graphene: carbon in two dimensions. *Materials Today* **2007,** *10* (1–2), 20-27.

52. Mak, K. F.; Shan, J.; Heinz, T. F., Electronic Structure of Few-Layer Graphene: Experimental Demonstration of Strong Dependence on Stacking Sequence. *Phys. Rev. Lett.* **2010,** *104* (17).

53. Novoselov, K. S.; Geim, A. K.; Morozov, S. V.; Jiang, D.; Katsnelson, M. I.; Grigorieva, I. V.; Dubonos, S. V.; Firsov, A. A., Two-dimensional gas of massless Dirac fermions in graphene. *Nature* **2005,** *438* (7065), 197-200.

54. Geim, A. K., Graphene: Status and Prospects. *Science* **2009,** *324* (5934), 1530-1534.

55. Du, X.; Skachko, I.; Barker, A.; Andrei, E. Y., Approaching ballistic transport in suspended graphene. *Nature Nanotechnology* **2008,** *3* (8), 491-495.

56. Li, X.; Cai, W.; An, J.; Kim, S.; Nah, J.; Yang, D.; Piner, R.; Velamakanni, A.; Jung, I.; Tutuc, E.; Banerjee, S. K.; Colombo, L.; Ruoff, R. S., Large-Area Synthesis of High-Quality and Uniform Graphene Films on Copper Foils. *Science* **2009,** *324* (5932), 1312-1314.

57. Chen, K.; Wan, X.; Wen, J.; Xie, W.; Kang, Z.; Zeng, X.; Chen, H.; Xu, J.-B., Electronic Properties of MoS2–WS2 Heterostructures Synthesized with Two-Step Lateral Epitaxial Strategy. *ACS Nano* **2015,** *9* (10), 9868-9876.

58. Gong, Y.; Lin, Z.; Ye, G.; Shi, G.; Feng, S.; Lei, Y.; Elías, A. L.; Perea-Lopez, N.; Vajtai, R.; Terrones, H.; Liu, Z.; Terrones, M.; Ajayan, P. M., Tellurium-Assisted Low-Temperature Synthesis of MoS2 and WS2 Monolayers. *ACS Nano* **2015,** *9* (12), 11658-11666.

59. Kumar, V. K.; Dhar, S.; Choudhury, T. H.; Shivashankar, S. A.; Raghavan, S., A predictive approach to CVD of crystalline layers of TMDs: the case of MoS2. *Nanoscale* **2015,** *7* (17), 7802-7810.

60. Dumcenco, D.; Ovchinnikov, D.; Sanchez, O. L.; Gillet, P.; Alexander, D. T. L.; Sorin, L.; Radenovic, A.; Kis, A., Large-area MoS2 grown using H2S as the sulphur source. *2D Materials* **2015,** *2* (4), 044005.

61. Chen, K.; Wan, X.; Wen, J. X.; Xie, W. G.; Kang, Z. W.; Zeng, X. L.; Chen, H. J.; Xu, J. B., Electronic Properties of MoS2-WS2 Heterostructures Synthesized with Two-Step Lateral Epitaxial Strategy. *ACS Nano* **2015,** *9* (10), 9868-9876.

62. Hu, S.; Wang, X.; Meng, L.; Yan, X., Controlled synthesis and mechanism of large-area WS2 flakes by low-pressure chemical vapor deposition. *J Mater Sci* **2017,** *52* (12), 7215-7223.

63. Kang, K.; Xie, S. E.; Huang, L. J.; Han, Y. M.; Huang, P. Y.; Mak, K. F.; Kim, C. J.; Muller, D.; Park, J., High-mobility three-atom-thick semiconducting films with wafer-scale homogeneity. *Nature* **2015,** *520* (7549), 656-660.

64. Eichfeld, S. M.; Hossain, L.; Lin, Y. C.; Piasecki, A. F.; Kupp, B.; Birdwell, A. G.; Burke, R. A.; Lu, N.; Peng, X.; Li, J.; Azcatl, A.; McDonnell, S.; Wallace, R. M.; Kim, M. J.; Mayer, T. S.; Redwing, J. M.; Robinson, J. A., Highly Scalable, Atomically Thin WSe2 Grown via Metal-Organic Chemical Vapor Deposition. *ACS Nano* **2015,** *9* (2), 2080-2087.

65. Boscher, N. D.; Carmalt, C. J.; Parkin, I. P., Atmospheric pressure chemical vapor deposition of WSe(2) thin films on glass - highly hydrophobic sticky surfaces. *J Mater Chem* **2006,** *16* (1), 122-127.

66. Li, M. Y.; Shi, Y. M.; Cheng, C. C.; Lu, L. S.; Lin, Y. C.; Tang, H. L.; Tsai, M. L.; Chu, C. W.; Wei, K. H.; He, J. H.; Chang, W. H.; Suenaga, K.; Li, L. J., Epitaxial growth of a monolayer WSe2-MoS2 lateral p-n junction with an atomically sharp interface. *Science* **2015,** *349* (6247), 524-528.

67. Gong, Y.; Lin, J.; Wang, X.; Shi, G.; Lei, S.; Lin, Z.; Zou, X.; Ye, G.; Vajtai, R.; Yakobson, B. I.; Terrones, H.; Terrones, M.; Tay, B. K.; Lou, J.; Pantelides, S. T.; Liu, Z.; Zhou, W.; Ajayan, P. M., Vertical and in-plane heterostructures from WS2/MoS2 monolayers. *Nat Mater* **2014,** *13* (12), 1135-1142.

68. Tarasov, A.; Campbell, P. M.; Tsai, M.-Y.; Hesabi, Z. R.; Feirer, J.; Graham, S.; Ready, W. J.; Vogel, E. M., Highly Uniform Trilayer Molybdenum Disulfide for Wafer-Scale Device Fabrication. *Adv. Funct. Mater.* **2014,** *24* (40), 6389-6400.

69. Heyne, M. H.; Chiappe, D.; Meersschaut, J.; Nuytten, T.; Conard, T.; Bender, H.; Huyghebaert, C.; Radu, I. P.; Caymax, M.; de Marneffe, J. F.; Neyts, E. C.; De Gendt, S., Multilayer MoS2 growth by metal and metal oxide sulfurization. *J. Mater. Chem. C* **2016,** *4* (6), 1295-1304.

70. Jung, Y.; Shen, J.; Liu, Y.; Woods, J. M.; Sun, Y.; Cha, J. J., Metal Seed Layer Thickness-Induced Transition From Vertical to Horizontal Growth of MoS2 and WS2. *Nano Lett.* **2014,** *14* (12), 6842-6849.

71. Kong, D.; Wang, H.; Cha, J. J.; Pasta, M.; Koski, K. J.; Yao, J.; Cui, Y., Synthesis of MoS2 and MoSe2 Films with Vertically Aligned Layers. *Nano Lett.* **2013,** *13* (3), 1341-1347.

72. Choudhary, N.; Park, J.; Hwang, J. Y.; Chung, H.-S.; Dumas, K. H.; Khondaker, S. I.; Choi, W.; Jung, Y., Centimeter Scale Patterned Growth of Vertically Stacked Few Layer Only 2D MoS2/WS2 van der Waals Heterostructure. *Scientific Reports* **2016,** *6*, srep25456.

73. Woods, J. M.; Jung, Y.; Xie, Y.; Liu, W.; Liu, Y.; Wang, H.; Cha, J. J., One-Step Synthesis of MoS2/WS2 Layered Heterostructures and Catalytic Activity of Defective Transition Metal Dichalcogenide Films. *ACS Nano* **2016,** *10* (2), 2004-2009.

74. Fu, D.; Zhao, X.; Zhang, Y.-Y.; Li, L.; Xu, H.; Jang, A. R.; Yoon, S. I.; Song, P.; Poh, S. M.; Ren, T.; Ding, Z.; Fu, W.; Shin, T. J.; Shin, H. S.; Pantelides, S. T.; Zhou, W.; Loh, K. P., Molecular Beam Epitaxy of Highly Crystalline Monolayer Molybdenum Disulfide on Hexagonal Boron Nitride. *J. Am. Chem. Soc.* **2017,** *139* (27), 9392-9400.

75. Zhan, L.; Wan, W.; Zhu, Z.; Shih, T.-M.; Cai, W., MoS2 materials synthesized on SiO2/Si substrates via MBE. *J. Phys.: Conf. Ser.* **2017,** *864* (1), 012037.

76. Miwa, J. A.; Dendzik, M.; Grønborg, S. S.; Bianchi, M.; Lauritsen, J. V.; Hofmann, P.; Ulstrup, S., Van der Waals Epitaxy of Two-Dimensional MoS2–Graphene Heterostructures in Ultrahigh Vacuum. *ACS Nano* **2015,** *9* (6), 6502-6510.

77. Yue, R.; Nie, Y.; Walsh, L. A.; Addou, R.; Liang, C.; Lu, N.; Barton, A. T.; Zhu, H.; Che, Z.; Barrera, D.; Cheng, L.; Cha, P.-R.; Chabal, Y. J.; Hsu, J. W. P.; Kim, J.; Kim, M. J.; Colombo, L.; Wallace, R. M.; Cho, K.; Hinkle, C. L., Nucleation and growth of WSe2 : enabling large grain transition metal dichalcogenides. *2D Materials* **2017,** *4* (4), 045019.

78. Diaz, H. C.; Chaghi, R.; Ma, Y. J.; Batzill, M., Molecular beam epitaxy of the van der Waals heterostructure MoTe2 on MoS2: phase, thermal, and chemical stability. *2d Materials* **2015,** *2* (4).

79. Roy, A.; Movva, H. C. P.; Satpati, B.; Kim, K.; Dey, R.; Rai, A.; Pramanik, T.; Guchhait, S.; Tutuc, E.; Banerjee, S. K., Structural and Electrical Properties of MoTe2 and MoSe2 Grown by Molecular Beam Epitaxy. *ACS Appl. Mater. Interfaces* **2016,** *8* (11), 7396-7402.

80. Tan, L. K.; Liu, B.; Teng, J. H.; Guo, S.; Low, H. Y.; Loh, K. P., Atomic layer deposition of a MoS2 film. *Nanoscale* **2014,** *6* (18), 10584-10588.

81. Pyeon, J. J.; Kim, S. H.; Jeong, D. S.; Baek, S.-H.; Kang, C.-Y.; Kim, J.-S.; Kim, S. K., Wafer-scale growth of MoS2 thin films by atomic layer deposition. *Nanoscale* **2016,** *8* (20), 10792-10798.

82. Ahn, C.; Lee, J.; Kim, H.-U.; Bark, H.; Jeon, M.; Ryu, G. H.; Lee, Z.; Yeom, G. Y.; Kim, K.; Jung, J.; Kim, Y.; Lee, C.; Kim, T., Low-Temperature Synthesis of Large-Scale Molybdenum Disulfide Thin Films Directly on a Plastic Substrate Using Plasma-Enhanced Chemical Vapor Deposition. *Adv. Mater.* **2015,** *27* (35), 5223-5229.

83. Colombo, L.; Li, X.; Han, B.; Magnuson, C.; Cai, W.; Zhu, Y.; Ruoff, R. S., Growth Kinetics and Defects of CVD Graphene on Cu. *ECS Trans.* **2010,** *28* (5), 109-114.

84. Charrier, A.; Coati, A.; Argunova, T.; Thibaudau, F.; Garreau, Y.; Pinchaux, R.; Forbeaux, I.; Debever, J. M.; Sauvage-Simkin, M.; Themlin, J. M., Solid-state decomposition of silicon carbide for growing ultra-thin heteroepitaxial graphite films. *Journal of Applied Physics* **2002,** *92* (5), 2479-2484.

85. Stankovich, S.; Dikin, D. A.; Piner, R. D.; Kohlhaas, K. A.; Kleinhammes, A.; Jia, Y.; Wu, Y.; Nguyen, S. T.; Ruoff, R. S., Synthesis of graphene-based nanosheets via chemical reduction of exfoliated graphite oxide. *Carbon* **2007,** *45* (7), 1558-1565.

86. Mattevi, C.; Kim, H.; Chhowalla, M., A review of chemical vapour deposition of graphene on copper. **2011,** *21* (10), 3324-3334.

87. Choi, W.; Lahiri, I.; Seelaboyina, R.; Kang, Y. S., Synthesis of Graphene and Its Applications: A Review. *Critical Reviews in Solid State and Materials Sciences* **2010,** *35* (1), 52-71.

88. Bhaviripudi, S.; Jia, X.; Dresselhaus, M. S.; Kong, J., Role of Kinetic Factors in Chemical Vapor Deposition Synthesis of Uniform Large Area Graphene Using Copper Catalyst. *Nano Lett.* **2010,** *10* (10), 4128-4133.

89. Kim, H.; Mattevi, C.; Calvo, M. R.; Oberg, J. C.; Artiglia, L.; Agnoli, S.; Hirjibehedin, C. F.; Chhowalla, M.; Saiz, E., Activation Energy Paths for Graphene Nucleation and Growth on Cu. *ACS Nano* **2012,** *6* (4), 3614-3623.

90. Loginova, E.; Bartelt, N. C.; Feibelman, P. J.; McCarty, K. F., Factors influencing graphene growth on metal surfaces. *New J. Phys.* **2009,** *11* (6), 063046.

91. Vlassiouk, I.; Smirnov, S.; Regmi, M.; Surwade, S. P.; Srivastava, N.; Feenstra, R.; Eres, G.; Parish, C.; Lavrik, N.; Datskos, P.; Dai, S.; Fulvio, P., Graphene Nucleation Density on Copper: Fundamental Role of Background Pressure. *J. Phys. Chem. C* **2013,** *117* (37), 18919-18926.

92. Kc, S.; Longo, R. C.; Addou, R.; Wallace, R. M.; Cho, K., Impact of intrinsic atomic defects on the electronic structure of MoS 2 monolayers. *Nanotechnology* **2014,** *25* (37), 375703.

93. Zhou, W.; Zou, X.; Najmaei, S.; Liu, Z.; Shi, Y.; Kong, J.; Lou, J.; Ajayan, P. M.; Yakobson, B. I.; Idrobo, J.-C., Intrinsic Structural Defects in Monolayer Molybdenum Disulfide. *Nano Lett.* **2013,** *13* (6), 2615-2622.

94. Azizi, A.; Zou, X. L.; Ercius, P.; Zhang, Z. H.; Elias, A. L.; Perea-Lopez, N.; Stone, G.; Terrones, M.; Yakobson, B. I.; Alem, N., Dislocation motion and grain boundary migration in two-dimensional tungsten disulphide. *Nature Communications* **2014,** *5*.

95. Sangwan, V. K.; Jariwala, D.; Kim, I. S.; Chen, K.-S.; Marks, T. J.; Lauhon, L. J.; Hersam, M. C., Gate-tunable memristive phenomena mediated by grain boundaries in single-layer MoS2. *Nature Nanotechnology* **2015,** *10* (5), 403.

96. Gao, N.; Guo, Y.; Zhou, S.; Bai, Y. Z.; Zhao, J. J., Structures and Magnetic Properties of MoS2 Grain Boundaries with Antisite Defects. *J Phys Chem C* **2017,** *121* (22), 12261-12269.

97. Li, G. Q.; Zhang, D.; Qiao, Q.; Yu, Y. F.; Peterson, D.; Zafar, A.; Kumar, R.; Curtarolo, S.; Hunte, F.; Shannon, S.; Zhu, Y. M.; Yang, W. T.; Cao, L. Y., All The Catalytic Active Sites of MoS2 for Hydrogen Evolution. *J. Am. Chem. Soc.* **2016,** *138* (51), 16632-16638.

98. Tsen, A. W.; Brown, L.; Levendorf, M. P.; Ghahari, F.; Huang, P. Y.; Havener, R. W.; Ruiz-Vargas, C. S.; Muller, D. A.; Kim, P.; Park, J., Tailoring Electrical Transport

Across Grain Boundaries in Polycrystalline Graphene. *Science* **2012,** *336* (6085), 1143-1146.

99. Fei, Z.; Rodin, A. S.; Gannett, W.; Dai, S.; Regan, W.; Wagner, M.; Liu, M. K.; McLeod, A. S.; Dominguez, G.; Thiemens, M.; Neto, A. H. C.; Keilmann, F.; Zettl, A.; Hillenbrand, R.; Fogler, M. M.; Basov, D. N., Electronic and plasmonic phenomena at graphene grain boundaries. *Nature Nanotechnology* **2013,** *8* (11), 821-825.

100. Li, X.; Magnuson, C. W.; Venugopal, A.; Tromp, R. M.; Hannon, J. B.; Vogel, E. M.; Colombo, L.; Ruoff, R. S., Large-area graphene single crystals grown by low-pressure chemical vapor deposition of methane on copper. *J. Am. Chem. Soc.* **2011,** *133* (9), 2816-2819.

101. Huang, P. Y.; Ruiz-Vargas, C. S.; van der Zande, A. M.; Whitney, W. S.; Levendorf, M. P.; Kevek, J. W.; Garg, S.; Alden, J. S.; Hustedt, C. J.; Zhu, Y.; Park, J.; McEuen, P. L.; Muller, D. A., Grains and grain boundaries in single-layer graphene atomic patchwork quilts. *Nature* **2011,** *469* (7330), 389-+.

102. Kotakoski, J.; Krasheninnikov, A. V.; Kaiser, U.; Meyer, J. C., From Point Defects in Graphene to Two-Dimensional Amorphous Carbon. *Phys. Rev. Lett.* **2011,** *106* (10).

103. Frey, G. L.; Tenne, R.; Matthews, M. J.; Dresselhaus, M. S.; Dresselhaus, G., Raman and resonance Raman investigation of MoS2 nanoparticles. *Phys. Rev. B* **1999,** *60* (4), 2883-2892.

104. Ferrari, A. C.; Basko, D. M., Raman spectroscopy as a versatile tool for studying the properties of graphene. *Nature Nanotechnology* **2013,** *8* (4), 235-246.

105. Ferrari, A. C., Raman spectroscopy of graphene and graphite: Disorder, electron–phonon coupling, doping and nonadiabatic effects. *Solid State Communications* **2007,** *143* (1–2), 47-57.

106. Kim, K.; Coh, S.; Tan, L. Z.; Regan, W.; Yuk, J. M.; Chatterjee, E.; Crommie, M. F.; Cohen, M. L.; Louie, S. G.; Zettl, A., Raman Spectroscopy Study of Rotated Double-Layer Graphene: Misorientation-Angle Dependence of Electronic Structure. *Phys. Rev. Lett.* **2012,** *108* (24), 246103.

107. Hwang, J.-Y.; Kuo, C.-C.; Chen, L.-C.; Chen, K.-H., Correlating defect density with carrier mobility in large-scaled graphene films: Raman spectral signatures for the estimation of defect density. *Nanotechnology* **2010,** *21* (46), 465705.

108. Yoon, C.; Cho, G.; Kim, S., Electrical Characteristics of GaAs Nanowire-Based MESFETs on Flexible Plastics. *Ieee T Electron Dev* **2011,** *58* (4), 1096-1101.

109. Wang, C. A.; Chien, J. C.; Fang, H.; Takei, K.; Nah, J.; Plis, E.; Krishna, S.; Niknejad, A. M.; Javey, A., Self-Aligned, Extremely High Frequency III-V Metal-Oxide-Semiconductor Field-Effect Transistors on Rigid and Flexible Substrates. *Nano Lett.* **2012,** *12* (8), 4140-4145.

110. Zhou, H.; Seo, J. H.; Paskiewicz, D. M.; Zhu, Y.; Celler, G. K.; Voyles, P. M.; Zhou, W. D.; Lagally, M. G.; Ma, Z. Q., Fast flexible electronics with strained silicon nanomembranes. *Scientific Reports* **2013,** *3*.

111. Katz, H. E.; Lovinger, A. J.; Johnson, J.; Kloc, C.; Siegrist, T.; Li, W.; Lin, Y. Y.; Dodabalapur, A., A soluble and air-stable organic semiconductor with high electron mobility. *Nature* **2000,** *404* (6777), 478-481.

112. Phan, H. D.; Kim, Y.; Lee, J.; Liu, R.; Choi, Y.; Cho, J. H.; Lee, C., Ultraclean and Direct Transfer of a Wafer-Scale MoS2 Thin Film onto a Plastic Substrate. *Adv. Mater.* **2017,** *29* (7).

113. Wang, H. M.; Wu, Y. H.; Cong, C. X.; Shang, J. Z.; Yu, T., Hysteresis of Electronic Transport in Graphene Transistors. *ACS Nano* **2010,** *4* (12), 7221-7228.

114. Liao, Z.-M.; Han, B.-H.; Zhou, Y.-B.; Yu, D.-P., Hysteresis reversion in graphene field-effect transistors. *The Journal of Chemical Physics* **2010,** *133* (4), 044703.

115. Late, D. J.; Liu, B.; Matte, H. S. S. R.; Dravid, V. P.; Rao, C. N. R., Hysteresis in Single-Layer MoS2 Field Effect Transistors. *ACS Nano* **2012,** *6* (6), 5635-5641.

116. Late, D. J.; Huang, Y. K.; Liu, B.; Acharya, J.; Shirodkar, S. N.; Luo, J. J.; Yan, A. M.; Charles, D.; Waghmare, U. V.; Dravid, V. P.; Rao, C. N. R., Sensing Behavior of Atomically Thin-Layered MoS2 Transistors. *ACS Nano* **2013,** *7* (6), 4879-4891.

117. Samnakay, R.; Jiang, C.; Rumyantsev, S. L.; Shur, M. S.; Balandin, A. A., Selective chemical vapor sensing with few-layer MoS2 thin-film transistors: Comparison with graphene devices. *Applied Physics Letters* **2015,** *106* (2).

118. Tarasov, A.; Zhang, S.; Tsai, M.-Y.; Campbell, P. M.; Graham, S.; Barlow, S.; Marder, S. R.; Vogel, E. M., Controlled Doping of Large-Area Trilayer MoS2 with Molecular Reductants and Oxidants. *Adv. Mater.* **2015,** *27* (7), 1175-1181.

119. Conley, H. J.; Wang, B.; Ziegler, J. I.; Haglund, R. F.; Pantelides, S. T.; Bolotin, K. I., Bandgap Engineering of Strained Monolayer and Bilayer MoS2. *Nano Lett.* **2013,** *13* (8), 3626-3630.

120. Yang, L.; Cui, X.; Zhang, J.; Wang, K.; Shen, M.; Zeng, S.; Dayeh, S. A.; Feng, L.; Xiang, B., Lattice strain effects on the optical properties of MoS2 nanosheets. *Scientific Reports* **2014,** *4*, 5649.

121. He, Y.; Yang, Y.; Zhang, Z.; Gong, Y.; Zhou, W.; Hu, Z.; Ye, G.; Zhang, X.; Bianco, E.; Lei, S.; Jin, Z.; Zou, X.; Yang, Y.; Zhang, Y.; Xie, E.; Lou, J.; Yakobson, B.; Vajtai, R.; Li, B.; Ajayan, P., Strain-Induced Electronic Structure Changes in Stacked van der Waals Heterostructures. *Nano Lett.* **2016,** *16* (5), 3314-3320.

122. Park, M.; Park, Y. J.; Chen, X.; Park, Y. K.; Kim, M. S.; Ahn, J. H., MoS2-Based Tactile Sensor for Electronic Skin Applications. *Adv. Mater.* **2016,** *28* (13), 2556-+.

123. Wang, Y.; Wang, L.; Yang, T. T.; Li, X.; Zang, X. B.; Zhu, M.; Wang, K. L.; Wu, D. H.; Zhu, H. W., Wearable and Highly Sensitive Graphene Strain Sensors for Human Motion Monitoring. *Adv. Funct. Mater.* **2014,** *24* (29), 4666-4670.

124. Tian, H.; Shu, Y.; Cui, Y. L.; Mi, W. T.; Yang, Y.; Xie, D.; Ren, T. L., Scalable fabrication of high-performance and flexible graphene strain sensors. *Nanoscale* **2014,** *6* (2), 699-705.

125. Splendiani, A.; Sun, L.; Zhang, Y.; Li, T.; Kim, J.; Chim, C.-Y.; Galli, G.; Wang, F., Emerging Photoluminescence in Monolayer MoS2. *Nano Lett.* **2010,** *10* (4), 1271-1275.

126. Photoluminescence properties and exciton dynamics in monolayer WSe2. *Applied Physics Letters* **2014,** *105* (10), 101901.

127. Tsai, M. L.; Su, S. H.; Chang, J. K.; Tsai, D. S.; Chen, C. H.; Wu, C. I.; Li, L. J.; Chen, L. J.; He, J. H., Monolayer MoS2 Heterojunction Solar Cells. *ACS Nano* **2014,** *8* (8), 8317-8322.

128. Miao, X. C.; Tongay, S.; Petterson, M. K.; Berke, K.; Rinzler, A. G.; Appleton, B. R.; Hebard, A. F., High Efficiency Graphene Solar Cells by Chemical Doping. *Nano Lett.* **2012,** *12* (6), 2745-2750.

129. Fontana, M.; Deppe, T.; Boyd, A. K.; Rinzan, M.; Liu, A. Y.; Paranjape, M.; Barbara, P., Electron-hole transport and photovoltaic effect in gated MoS2 Schottky junctions. *Scientific Reports* **2013,** *3*.

130. Luo, X.; Zhai, X.; Wang, L. L.; Lin, Q., Enhanced dual-band absorption of molybdenum disulfide using a plasmonic perfect absorber. *Opt Express* **2018,** *26* (9), 11658-11666.

131. Britnell, L.; Ribeiro, R. M.; Eckmann, A.; Jalil, R.; Belle, B. D.; Mishchenko, A.; Kim, Y. J.; Gorbachev, R. V.; Georgiou, T.; Morozov, S. V.; Grigorenko, A. N.; Geim, A. K.; Casiraghi, C.; Castro Neto, A. H.; Novoselov, K. S., Strong Light-Matter Interactions in Heterostructures of Atomically Thin Films. *Science* **2013,** *340* (6138), 1311-1314.

132. Lin, J. D.; Li, H.; Zhang, H.; Chen, W., Plasmonic enhancement of photocurrent in MoS2 field-effect-transistor. *Applied Physics Letters* **2013,** *102* (20).

133. Ross, J. S.; Klement, P.; Jones, A. M.; Ghimire, N. J.; Yan, J. Q.; Mandrus, D. G.; Taniguchi, T.; Watanabe, K.; Kitamura, K.; Yao, W.; Cobden, D. H.; Xu, X. D., Electrically tunable excitonic light-emitting diodes based on monolayer WSe2 p-n junctions. *Nature Nanotechnology* **2014,** *9* (4), 268-272.

134. Zhang, Y. J.; Oka, T.; Suzuki, R.; Ye, J. T.; Iwasa, Y., Electrically Switchable Chiral Light-Emitting Transistor. *Science* **2014,** *344* (6185), 725-728.

135. Withers, F.; Del Pozo-Zamudio, O.; Mishchenko, A.; Rooney, A. P.; Gholinia, A.; Watanabe, K.; Taniguchi, T.; Haigh, S. J.; Geim, A. K.; Tartakovskii, A. I.; Novoselov, K.

S., Light-emitting diodes by band-structure engineering in van der Waals heterostructures. *Nat Mater* **2015,** *14* (3), 301-306.

136. Palacios-Berraquero, C.; Barbone, M.; Kara, D. M.; Chen, X. L.; Goykhman, I.; Yoon, D.; Ott, A. K.; Beitner, J.; Watanabe, K.; Taniguchi, T.; Ferrari, A. C.; Atature, M., Atomically thin quantum light-emitting diodes. *Nature Communications* **2016,** *7*.

137. Baugher, B. W. H.; Churchill, H. O. H.; Yang, Y. F.; Jarillo-Herrero, P., Optoelectronic devices based on electrically tunable p-n diodes in a monolayer dichalcogenide. *Nature Nanotechnology* **2014,** *9* (4), 262-267.

138. Mueller, T.; Pospischil, A.; Furchi, M. M. In *2D materials and heterostructures for applications in optoelectronics*, 2015; 2015; pp 946713-946713-6.

139. Liu, C.-H.; Chang, Y.-C.; Norris, T. B.; Zhong, Z., Graphene photodetectors with ultra-broadband and high responsivity at room temperature. *Nature Nanotechnology* **2014,** *9* (4), 273-278.

140. Yin, Z. Y.; Li, H.; Li, H.; Jiang, L.; Shi, Y. M.; Sun, Y. H.; Lu, G.; Zhang, Q.; Chen, X. D.; Zhang, H., Single-Layer MoS2 Phototransistors. *ACS Nano* **2012,** *6* (1), 74-80.

141. Roy, T.; Tosun, M.; Cao, X.; Fang, H.; Lien, D.-H.; Zhao, P.; Chen, Y.-Z.; Chueh, Y.-L.; Guo, J.; Javey, A., Dual-Gated MoS2/WSe2 van der Waals Tunnel Diodes and Transistors. *ACS Nano* **2015,** *9* (2), 2071-2079.

142. Li, M. O.; Esseni, D.; Snider, G.; Jena, D.; Xing, H. G., Single particle transport in two-dimensional heterojunction interlayer tunneling field effect transistor. *Journal of Applied Physics* **2014,** *115* (7), 074508.

143. Chang, L. L.; Esaki, L.; Tsu, R., Resonant Tunneling in Semiconductor Double Barriers. *Applied Physics Letters* **1974,** *24* (12), 593-595.

144. Nourbakhsh, A.; Zubair, A.; Dresselhaus, M. S.; Palacios, T., Transport Properties of a MoS2/WSe2 Heterojunction Transistor and Its Potential for Application. *Nano Lett.* **2016,** *16* (2), 1359-1366.

145. Yan, R. S.; Fathipour, S.; Han, Y. M.; Song, B.; Xiao, S. D.; Li, M. D.; Ma, N.; Protasenko, V.; Muller, D. A.; Jena, D.; Xing, H. G., Esaki Diodes in van der Waals Heterojunctions with Broken-Gap Energy Band Alignment. *Nano Lett.* **2015,** *15* (9), 5791-5798.

146. Zhao, P.; Feenstra, R. M.; Gu, G.; Jena, D., SymFET: A Proposed Symmetric Graphene Tunneling Field-Effect Transistor. *Ieee T Electron Dev* **2013,** *60* (3), 951-957.

147. Britnell, L.; Gorbachev, R. V.; Jalil, R.; Belle, B. D.; Schedin, F.; Mishchenko, A.; Georgiou, T.; Katsnelson, M. I.; Eaves, L.; Morozov, S. V.; Peres, N. M. R.; Leist, J.;

Geim, A. K.; Novoselov, K. S.; Ponomarenko, L. A., Field-Effect Tunneling Transistor Based on Vertical Graphene Heterostructures. *Science* **2012,** *335* (6071), 947-950.

148. Roy, T.; Liu, L.; de la Barrera, S.; Chakrabarti, B.; Hesabi, Z. R.; Joiner, C. A.; Feenstra, R. M.; Gu, G.; Vogel, E. M., Tunneling characteristics in chemical vapor deposited graphene–hexagonal boron nitride–graphene junctions. *Applied Physics Letters* **2014,** *104* (12), 123506.

149. Lin, Y.-C.; Ghosh, R. K.; Addou, R.; Lu, N.; Eichfeld, S. M.; Zhu, H.; Li, M.-Y.; Peng, X.; Kim, M. J.; Li, L.-J.; Wallace, R. M.; Datta, S.; Robinson, J. A., Atomically Thin Resonant Tunnel Diodes built from Synthetic van der Waals Heterostructures. *Nature Communications* **2015,** *6*, 7311.

150. Zhou, R.; Ostwal, V.; Appenzeller, J., Vertical versus Lateral Two-Dimensional Heterostructures: On the Topic of Atomically Abrupt p/n-Junctions. *Nano Lett.* **2017,** *17* (8), 4787–4792.

151. Roy, T.; Hesabi, Z. R.; Joiner, C. A.; Fujimoto, A.; Vogel, E. M., Barrier engineering for double layer CVD graphene tunnel FETs. *Microelectronic Engineering* **2013,** *109*, 117-119.

152. Kawahara, A.; Azuma, R.; Ikeda, Y.; Kawai, K.; Katoh, Y.; Hayakawa, Y.; Tsuji, K.; Yoneda, S.; Himeno, A.; Shimakawa, K.; Takagi, T.; Mikawa, T.; Aono, K., An 8 Mb Multi-Layered Cross-Point ReRAM Macro With 443 MB/s Write Throughput. *Ieee J Solid-St Circ* **2013,** *48* (1), 178-185.

153. Burr, G. W.; Shenoy, R. S.; Virwani, K.; Narayanan, P.; Padilla, A.; Kurdi, B.; Hwang, H., Access devices for 3D crosspoint memory. *Journal of Vacuum Science & Technology B* **2014,** *32* (4), 040802.

154. Houssa, M.; Dimoulas, A.; Alessandro, M., *2D Materials for Nanoelectronics*. CRC Press: 2016; p 467.

155. Govoreanu, B.; Zhang, L. Q.; Jurczak, M., Selectors for High Density Crosspoint Memory Arrays: Design Considerations, Device Implementations and Some Challenges Ahead. *2015 International Conference on IC Design & Technology (ICICDT)* **2015**.

156. Song, S. M.; Park, J. K.; Sul, O. J.; Cho, B. J., Determination of work function of graphene under a metal electrode and its role in contact resistance. *Nano Lett.* **2012,** *12* (8), 3887-3892.

157. Smyth, C. M.; Addou, R.; McDonnell, S.; Hinkle, C. L.; Wallace, R. M., Contact Metal–MoS2 Interfacial Reactions and Potential Implications on MoS2-Based Device Performance. *J. Phys. Chem. C* **2016,** *120* (27), 14719-14729.

158. Gong, C.; Colombo, L.; Wallace, R. M.; Cho, K., The Unusual Mechanism of Partial Fermi Level Pinning at Metal–MoS2 Interfaces. *Nano Lett.* **2014,** *14* (4), 1714-1720.

159. Kang, J. H.; Liu, W.; Sarkar, D.; Jena, D.; Banerjee, K., Computational Study of Metal Contacts to Monolayer Transition-Metal Dichalcogenide Semiconductors. *Phys Rev X* **2014,** *4* (3), 031005.

160. Kim, C.; Moon, I.; Lee, D.; Choi, M. S.; Ahmed, F.; Nam, S.; Cho, Y.; Shin, H.-J.; Park, S.; Yoo, W. J., Fermi Level Pinning at Electrical Metal Contacts of Monolayer Molybdenum Dichalcogenides. *ACS Nano* **2017,** *11* (2), 1588-1596.

161. Guo, Y.; Liu, D.; Robertson, J., Chalcogen vacancies in monolayer transition metal dichalcogenides and Fermi level pinning at contacts. *Applied Physics Letters* **2015,** *106* (17), 173106.

162. Bampoulis, P.; van Bremen, R.; Yao, Q.; Poelsema, B.; Zandvliet, H. J. W.; Sotthewes, K., Defect Dominated Charge Transport and Fermi Level Pinning in MoS2/Metal Contacts. *ACS Appl. Mater. Interfaces* **2017,** *9* (22), 19278-19286.

163. Zhou, P.; Song, X.; Yan, X.; Liu, C.; Chen, L.; Sun, Q.; Zhang, D. W., Controlling the work function of molybdenum disulfide by in situ metal deposition. *Nanotechnology* **2016,** *27* (34), 344002.

164. Zhong, H. X.; Quhe, R. G.; Wang, Y. Y.; Ni, Z. Y.; Ye, M.; Song, Z. G.; Pan, Y. Y.; Yang, J. B.; Yang, L.; Lei, M.; Shi, J. J.; Lu, J., Interfacial Properties of Monolayer and Bilayer MoS2 Contacts with Metals: Beyond the Energy Band Calculations. *Scientific Reports* **2016,** *6*.

165. Wang, Y. Y.; Yang, R. X.; Quhe, R.; Zhong, H. X.; Cong, L. X.; Ye, M.; Ni, Z. Y.; Song, Z. G.; Yang, J. B.; Shi, J. J.; Li, J.; Lu, J., Does p-type ohmic contact exist in WSe2-metal interfaces? *Nanoscale* **2016,** *8* (2), 1179-1191.

166. Pan, Y. Y.; Li, S. B.; Ye, M.; Quhe, R. G.; Song, Z. G.; Wang, Y. Y.; Zheng, J. X.; Pan, F.; Guo, W. L.; Yang, J. B.; Lu, J., Interfacial Properties of Monolayer MoSe2-Metal Contacts. *J Phys Chem C* **2016,** *120* (24), 13063-13070.

167. Hughes, R. C., Charge-Carrier Transport Phenomena in Amorphous SiO2: Direct Measurement of the Drift Mobility and Lifetime. *Phys. Rev. Lett.* **1973,** *30* (26), 1333-1336.

168. Schwank, J. R.; Shaneyfelt, M. R.; Fleetwood, D. M.; Felix, J. A.; Dodd, P. E.; Paillet, P.; Ferlet-Cavrois, V., Radiation Effects in MOS Oxides. *IEEE Transactions on Nuclear Science* **2008,** *55* (4), 1833-1853.

169. Oldham, T. R.; McLean, F. B., Total ionizing dose effects in MOS oxides and devices. *IEEE Transactions on Nuclear Science* **2003,** *50* (3), 483-499.

170. Parkin, W. M.; Balan, A.; Liang, L.; Das, P. M.; Lamparski, M.; Naylor, C. H.; Rodríguez-Manzo, J. A.; Johnson, A. T. C.; Meunier, V.; Drndić, M., Raman Shifts in Electron-Irradiated Monolayer MoS2. *ACS Nano* **2016,** *10* (4), 4134-4142.

171. Kim, T.-Y.; Cho, K.; Park, W.; Park, J.; Song, Y.; Hong, S.; Hong, W.-K.; Lee, T., Irradiation Effects of High-Energy Proton Beams on MoS2 Field Effect Transistors. *ACS Nano* **2014,** *8* (3), 2774-2781.

172. Rai, A.; Thoutam, L.; Zhang, W.; Kovi, K.; Banerjee, S.; Das, S. In *Effects of High-Energy X-Ray Radiation on MoS2 FETs*, APS Meeting Abstracts, 2016; 2016.

173. Algara-Siller, G.; Kurasch, S.; Sedighi, M.; Lehtinen, O.; Kaiser, U., The pristine atomic structure of MoS2 monolayer protected from electron radiation damage by graphene. *Applied Physics Letters* **2013,** *103* (20), 203107.

174. Zan, R.; Ramasse, Q. M.; Jalil, R.; Georgiou, T.; Bangert, U.; Novoselov, K. S., Control of Radiation Damage in MoS2 by Graphene Encapsulation. *ACS Nano* **2013,** *7* (11), 10167-10174.

175. Stanford, M. G.; Pudasaini, P. R.; Belianinov, A.; Cross, N.; Noh, J. H.; Koehler, M. R.; Mandrus, D. G.; Duscher, G.; Rondinone, A. J.; Ivanov, I. N.; Ward, T. Z.; Rack, P. D., Focused helium-ion beam irradiation effects on electrical transport properties of few-layer WSe2: enabling nanoscale direct write homo-junctions. *Scientific Reports* **2016,** *6*, 27276.

176. Tongay, S.; Suh, J.; Ataca, C.; Fan, W.; Luce, A.; Kang, J. S.; Liu, J.; Ko, C.; Raghunathanan, R.; Zhou, J.; Ogletree, F.; Li, J.; Grossman, J. C.; Wu, J., Defects activated photoluminescence in two-dimensional semiconductors: interplay between bound, charged, and free excitons. *Scientific Reports* **2013,** *3*.

177. Inoue, A.; Komori, T.; Shudo, K.-i., Atomic-scale structures and electronic states of defects on Ar+-ion irradiated MoS2. *Journal of Electron Spectroscopy and Related Phenomena* **2013,** *189, Supplement*, 11-18.

178. Komsa, H.-P.; Kotakoski, J.; Kurasch, S.; Lehtinen, O.; Kaiser, U.; Krasheninnikov, A. V., Two-Dimensional Transition Metal Dichalcogenides under Electron Irradiation: Defect Production and Doping. *Phys. Rev. Lett.* **2012,** *109* (3), 035503.

179. Meyer, J. C.; Eder, F.; Kurasch, S.; Skakalova, V.; Kotakoski, J.; Park, H. J.; Roth, S.; Chuvilin, A.; Eyhusen, S.; Benner, G.; Krasheninnikov, A. V.; Kaiser, U., Accurate Measurement of Electron Beam Induced Displacement Cross Sections for Single-Layer Graphene. *Phys. Rev. Lett.* **2012,** *108* (19), 196102.

180. Krivanek, O. L.; Dellby, N.; Murfitt, M. F.; Chisholm, M. F.; Pennycook, T. J.; Suenaga, K.; Nicolosi, V., Gentle STEM: ADF imaging and EELS at low primary energies. *Ultramicroscopy* **2010,** *110* (8), 935-945.

181. Chiritescu, C.; Cahill, D. G.; Nguyen, N.; Johnson, D.; Bodapati, A.; Keblinski, P.; Zschack, P., Ultralow Thermal Conductivity in Disordered, Layered WSe2 Crystals. *Science* **2007,** *315* (5810), 351-353.

182. Jung, C.; Kim, S. M.; Moon, H.; Han, G.; Kwon, J.; Hong, Y. K.; Omkaram, I.; Yoon, Y.; Kim, S.; Park, J., Highly Crystalline CVD-grown Multilayer MoSe2 Thin Film Transistor for Fast Photodetector. *Scientific Reports* **2015,** *5*, 15313.

183. Francis, S. A.; Petrosky, J. C.; McClory, J. W.; Cress, C. D., Effects of Proton and X-ray Irradiation on Graphene Field-Effect Transistors with Thin Gate Dielectrics. *IEEE Transactions on Nuclear Science* **2014,** *61* (6), 3010-3017.

184. Puzyrev, Y. S.; Wang, B.; Zhang, E. X.; Zhang, C. X.; Newaz, A. K. M.; Bolotin, K. I.; Fleetwood, D. M.; Schrimpf, R. D.; Pantelides, S. T., Surface Reactions and Defect Formation in Irradiated Graphene Devices. *IEEE Transactions on Nuclear Science* **2012,** *59* (6), 3039-3044.

185. Hicks, J.; Arora, R.; Kenyon, E.; Chakraborty, P. S.; Tinkey, H.; Hankinson, J.; Berger, C.; Heer, W. A. d.; Conrad, E. H.; Cressler, J. D., X-ray radiation effects in multilayer epitaxial graphene. *Applied Physics Letters* **2011,** *99* (23), 232102.

186. Zhang, E. X.; Newaz, A. K. M.; Wang, B.; Bhandaru, S.; Zhang, C. X.; Fleetwood, D. M.; Bolotin, K. I.; Pantelides, S. T.; Alles, M. L.; Schrimpf, R. D.; Weiss, S. M.; Reed, R. A.; Weller, R. A., Low-Energy X-ray and Ozone-Exposure Induced Defect Formation in Graphene Materials and Devices. *IEEE Transactions on Nuclear Science* **2011,** *58* (6), 2961-2967.

187. Zhang, E. X.; Newaz, A. K. M.; Wang, B.; Zhang, C. X.; Fleetwood, D. M.; Bolotin, K. I.; Schrimpf, R. D.; Pantelides, S. T.; Alles, M. L., Ozone-exposure and annealing effects on graphene-on-SiO2 transistors. *Applied Physics Letters* **2012,** *101* (12), 121601.

188. Zhang, C. X.; Wang, B.; Duan, G. X.; Zhang, E. X.; Fleetwood, D. M.; Alles, M. L.; Schrimpf, R. D.; Rooney, A. P.; Khestanova, E.; Auton, G.; Gorbachev, R. V.; Haigh, S. J.; Pantelides, S. T., Total Ionizing Dose Effects on hBN Encapsulated Graphene Devices. *IEEE Transactions on Nuclear Science* **2014,** *61* (6), 2868-2873.

189. Teweldebrhan, D.; Balandin, A. A., Modification of graphene properties due to electron-beam irradiation. *Applied Physics Letters* **2009,** *94* (1), 013101.

190. Childres, I.; Jalilian, R.; Foxe, M.; Chernyshov, A.; Rohkinson, L.; Jovanovic, I.; Chen, Y. P. In *Effect of Energetic Electron Irradiation on Graphene*, INTERNATIONAL CONFERENCE ON APPLICATIONS OF NUCLEAR TECHNIQUES, 2009/12/02/; AIP Publishing: 2009; pp 140-144.

191. Krasheninnikov, A. V.; Nordlund, K., Ion and electron irradiation-induced effects in nanostructured materials. *Journal of Applied Physics* **2010,** *107* (7), 071301.

192. Tapasztó, L.; Dobrik, G.; Nemes-Incze, P.; Vertesy, G.; Lambin, P.; Biró, L. P., Tuning the electronic structure of graphene by ion irradiation. *Phys. Rev. B* **2008,** *78* (23), 233407.

193. Chen, J.-H.; Cullen, W. G.; Jang, C.; Fuhrer, M. S.; Williams, E. D., Defect Scattering in Graphene. *Phys. Rev. Lett.* **2009,** *102* (23), 236805.

194. Her, M.; Beams, R.; Novotny, L., Graphene transfer with reduced residue. *Phys Lett A* **2013,** *377* (21-22), 1455-1458.

195. Kim, D. C.; Jeon, D. Y.; Chung, H. J.; Woo, Y.; Shin, J. K.; Seo, S., The structural and electrical evolution of graphene by oxygen plasma-induced disorder. *Nanotechnology* **2009,** *20* (37).

196. Childres, I.; Jauregui, L. A.; Tian, J.; Chen, Y. P., Effect of oxygen plasma etching on graphene studied using Raman spectroscopy and electronic transport measurements. *New J. Phys.* **2011,** *13* (2), 025008.

197. Moser, J.; Barreiro, A.; Bachtold, A., Current-induced cleaning of graphene. *Applied Physics Letters* **2007,** *91* (16).

198. Cheng, Z. G.; Zhou, Q. Y.; Wang, C. X.; Li, Q. A.; Wang, C.; Fang, Y., Toward Intrinsic Graphene Surfaces: A Systematic Study on Thermal Annealing and Wet-Chemical Treatment of SiO2-Supported Graphene Devices. *Nano Lett.* **2011,** *11* (2), 767-771.

199. Joiner, C. A.; Campbell, P. M.; Tarasov, A. A.; Beatty, B. R.; Perini, C. J.; Tsai, M.-Y.; Ready, W. J.; Vogel, E. M., Graphene-Molybdenum Disulfide-Graphene Tunneling Junctions with Large-Area Synthesized Materials. *ACS Appl. Mater. Interfaces* **2016,** *8* (13), 8702-8709.

200. Xu, K.; Cao, P. G.; Heath, J. R., Graphene Visualizes the First Water Adlayers on Mica at Ambient Conditions. *Science* **2010,** *329* (5996), 1188-1191.

201. Joiner, C. A.; Roy, T.; Hesabi, Z. R.; Chakrabarti, B.; Vogel, E. M., Cleaning graphene with a titanium sacrificial layer. *Applied Physics Letters* **2014,** *104* (22), 223109.

202. Pirkle, A.; Chan, J.; Venugopal, A.; Hinojos, D.; Magnuson, C. W.; McDonnell, S.; Colombo, L.; Vogel, E. M.; Ruoff, R. S.; Wallace, R. M., The effect of chemical residues on the physical and electrical properties of chemical vapor deposited graphene transferred to SiO2. *Applied Physics Letters* **2011,** *99* (12), 122108.

203. Kim, S.; Nah, J.; Jo, I.; Shahrjerdi, D.; Colombo, L.; Yao, Z.; Tutuc, E.; Banerjee, S. K., Realization of a high mobility dual-gated graphene field-effect transistor with Al2O3 dielectric. *Applied Physics Letters* **2009,** *94* (6), 062107.

204. Venugopal, A.; Chan, J.; Li, X. S.; Magnuson, C. W.; Kirk, W. P.; Colombo, L.; Ruoff, R. S.; Vogel, E. M., Effective mobility of single-layer graphene transistors as a function of channel dimensions. *Journal of Applied Physics* **2011,** *109* (10).

205. Li, S. L.; Wakabayashi, K.; Xu, Y.; Nakaharai, S.; Komatsu, K.; Li, W. W.; Lin, Y. F.; Aparecido-Ferreira, A.; Tsukagoshi, K., Thickness-Dependent Interfacial Coulomb

Scattering in Atomically Thin Field-Effect Transistors. *Nano Lett.* **2013,** *13* (8), 3546-3552.

206. Yang, R.; Zheng, X. Q.; Wang, Z. H.; Miller, C. J.; Feng, P. X. L., Multilayer MoS2 transistors enabled by a facile dry-transfer technique and thermal annealing. *Journal of Vacuum Science & Technology B* **2014,** *32* (6).

207. Ye, G.; Gong, Y.; Lin, J.; Li, B.; He, Y.; Pantelides, S. T.; Zhou, W.; Vajtai, R.; Ajayan, P. M., Defects Engineered Monolayer MoS2 for Improved Hydrogen Evolution Reaction. *Nano Lett.* **2016,** *16* (2), 1097-1103.

208. Lee, Y.-H.; Zhang, X.-Q.; Zhang, W.; Chang, M.-T.; Lin, C.-T.; Chang, K.-D.; Yu, Y.-C.; Wang, J. T.-W.; Chang, C.-S.; Li, L.-J.; Lin, T.-W., Synthesis of Large-Area MoS2 Atomic Layers with Chemical Vapor Deposition. *Adv. Mater.* **2012,** *24* (17), 2320-2325.

209. Campbell, P. M.; Tarasov, A.; Joiner, C. A.; Tsai, M.-Y.; Pavlidis, G.; Graham, S.; Ready, W. J.; Vogel, E. M., Field-effect transistors based on wafer-scale, highly uniform few-layer p-type WSe2. **2016,** *8* (4), 2268-2276.

210. Kim, Y.; Bark, H.; Ryu, G. H.; Lee, Z.; Lee, C., Wafer-scale monolayer MoS_2 grown by chemical vapor deposition using a reaction of MoO_3 and H_2S. *J. Phys.: Condens. Matter* **2016,** *28* (18), 184002.

211. Lee, Y.; Lee, J.; Bark, H.; Oh, I.-K.; Ryu, G. H.; Lee, Z.; Kim, H.; Cho, J. H.; Ahn, J.-H.; Lee, C., Synthesis of wafer-scale uniform molybdenum disulfide films with control over the layer number using a gas phase sulfur precursor. *Nanoscale* **2014,** *6* (5), 2821-2826.

212. Sørensen, S. G.; Füchtbauer, H. G.; Tuxen, A. K.; Walton, A. S.; Lauritsen, J. V., Structure and Electronic Properties of In Situ Synthesized Single-Layer MoS2 on a Gold Surface. *ACS Nano* **2014,** *8* (7), 6788-6796.

213. Kang, N.; Paudel, H. P.; Leuenberger, M. N.; Tetard, L.; Khondaker, S. I., Photoluminescence Quenching in Single-Layer MoS2 via Oxygen Plasma Treatment. *J. Phys. Chem. C* **2014,** *118* (36), 21258-21263.

214. Ramakrishna Matte, H. S. S.; Gomathi, A.; Manna, A. K.; Late, D. J.; Datta, R.; Pati, S. K.; Rao, C. N. R., MoS2 and WS2 Analogues of Graphene. *Angewandte Chemie International Edition* **2010,** *49* (24), 4059-4062.

215. Li, H.; Zhang, Q.; Yap, C. C. R.; Tay, B. K.; Edwin, T. H. T.; Olivier, A.; Baillargeat, D., From Bulk to Monolayer MoS2: Evolution of Raman Scattering. *Adv. Funct. Mater.* **2012,** *22* (7), 1385-1390.

216. Wagner, C. D., Sensitivity factors for XPS analysis of surface atoms. *Journal of Electron Spectroscopy and Related Phenomena* **1983,** *32* (2), 99-102.

217. Kim, I. S.; Sangwan, V. K.; Jariwala, D.; Wood, J. D.; Park, S.; Chen, K.-S.; Shi, F.; Ruiz-Zepeda, F.; Ponce, A.; Jose-Yacaman, M.; Dravid, V. P.; Marks, T. J.; Hersam, M. C.; Lauhon, L. J., Influence of Stoichiometry on the Optical and Electrical Properties of Chemical Vapor Deposition Derived MoS2. *ACS Nano* **2014,** *8* (10), 10551-10558.

218. Sen, H. S.; Sahin, H.; Peeters, F. M.; Durgun, E., Monolayers of MoS2 as an oxidation protective nanocoating material. *Journal of Applied Physics* **2014,** *116* (8), 083508.

219. Ghatak, S.; Pal, A. N.; Ghosh, A., Nature of Electronic States in Atomically Thin MoS2 Field-Effect Transistors. *ACS Nano* **2011,** *5* (10), 7707-7712.

220. Park, T.-E.; Suh, J.; Seo, D.; Park, J.; Lin, D.-Y.; Huang, Y.-S.; Choi, H.-J.; Wu, J.; Jang, C.; Chang, J., Hopping conduction in p-type MoS2 near the critical regime of the metal-insulator transition. *Applied Physics Letters* **2015,** *107* (22), 223107.

221. Qiu, H.; Xu, T.; Wang, Z.; Ren, W.; Nan, H.; Ni, Z.; Chen, Q.; Yuan, S.; Miao, F.; Song, F.; Long, G.; Shi, Y.; Sun, L.; Wang, J.; Wang, X., Hopping transport through defect-induced localized states in molybdenum disulphide. *Nature Communications* **2013,** *4*, 2642.

222. Utama, M. I. B.; Lu, X.; Zhan, D.; Ha, S. T.; Yuan, Y.; Shen, Z.; Xiong, Q., Etching-free patterning method for electrical characterization of atomically thin MoSe2 films grown by chemical vapor deposition. *Nanoscale* **2014,** *6* (21), 12376-12382.

223. Fritzsche, H., Electronic Processes in Non-Crystalline Materials. N. F. Mott and E. A. Davis. Oxford University Press, New York, 1971. xiv, 438 pp., illus. $24. International Series of Monographs on Physics. *Science* **1972,** *176* (4039), 1117-1117.

224. Van Keuls, F. W.; Hu, X. L.; Jiang, H. W.; Dahm, A. J., Screening of the Coulomb interaction in two-dimensional variable-range hopping. *Phys. Rev. B* **1997,** *56* (3), 1161-1169.

225. Hsieh, K.; Kochat, V.; Zhang, X.; Gong, Y.; Tiwary, C. S.; Ajayan, P. M.; Ghosh, A., Effect of Carrier Localization on Electrical Transport and Noise at Individual Grain Boundaries in Monolayer MoS2. *Nano Lett.* **2017,** *17* (9), 5452-5457.

226. Bertrand, P. A., Surface-phonon dispersion of MoS2. *Phys. Rev. B* **1991,** *44* (11), 5745-5749.

227. Lei, Y.; Pakhira, S.; Fujisawa, K.; Wang, X.; Iyiola, O. O.; Perea López, N.; Laura Elías, A.; Pulickal Rajukumar, L.; Zhou, C.; Kabius, B.; Alem, N.; Endo, M.; Lv, R.; Mendoza-Cortes, J. L.; Terrones, M., Low-temperature Synthesis of Heterostructures of Transition Metal Dichalcogenide Alloys (WxMo1–xS2) and Graphene with Superior Catalytic Performance for Hydrogen Evolution. *ACS Nano* **2017,** *11* (5), 5103-5112.

228. Lukowski, M. A.; Daniel, A. S.; Meng, F.; Forticaux, A.; Li, L.; Jin, S., Enhanced Hydrogen Evolution Catalysis from Chemically Exfoliated Metallic MoS2 Nanosheets. *J. Am. Chem. Soc.* **2013,** *135* (28), 10274-10277.

229. Campbell, P. M. Synthesis Of Large-Area Two-Dimensional Materials For Vertical Heterostructures. Georgia Institute of Technology, 2017.

230. Pensa, E.; Cortes, E.; Corthey, G.; Carro, P.; Vericat, C.; Fonticelli, M. H.; Benitez, G.; Rubert, A. A.; Salvarezza, R. C., The Chemistry of the Sulfur-Gold Interface: In Search of a Unified Model. *Acc. Chem. Res.* **2012,** *45* (8), 1183-1192.

231. Zhu, Y. Q.; Zhou, R. P.; Zhang, F.; Appenzeller, J., Vertical charge transport through transition metal dichalcogenides - a quantitative analysis. *Nanoscale* **2017,** *9* (48), 19108-19113.

232. Qian, K.; Tay, R. Y.; Nguyen, V. C.; Wang, J. X.; Cai, G. F.; Chen, T. P.; Teo, E. H. T.; Lee, P. S., Hexagonal Boron Nitride Thin Film for Flexible Resistive Memory Applications. *Adv. Funct. Mater.* **2016,** *26* (13), 2176-2184.

233. Kim, K.-j.; Choi, J.; Lee, H.; Lee, H.-K.; Kang, T.-H.; Han, Y.-H.; Lee, B.-C.; Kim, S.; Kim, B., Effects of 1 MeV Electron Beam Irradiation on Multilayer Graphene Grown on 6H-SiC(0001). *J. Phys. Chem. C* **2008,** *112* (34), 13062-13064.

234. Ando, T., Screening effect and impurity scattering in monolayer graphene. *J Phys Soc Jpn* **2006,** *75* (7).

235. Castro Neto, A. H.; Guinea, F.; Peres, N. M. R.; Novoselov, K. S.; Geim, A. K., The electronic properties of graphene. *Rev. Mod. Phys.* **2009,** *81* (1), 109-162.

236. Fleetwood, D. M., 1/f Noise and Defects in Microelectronic Materials and Devices. *Ieee Transactions on Nuclear Science* **2015,** *62* (4), 1462-1486.

237. Dutta, P.; Horn, P. M., Low-Frequency Fluctuations in Solids - 1-F Noise. *Rev. Mod. Phys.* **1981,** *53* (3), 497-516.

238. Hong, X.; Zou, K.; Zhu, J., Quantum scattering time and its implications on scattering sources in graphene. *Phys. Rev. B* **2009,** *80* (24).

239. Cress, C. D.; McMorrow, J. J.; Robinson, J. T.; Landi, B. J.; Hubbard, S. M.; Messenger, S. R., Radiation Effects in Carbon Nanoelectronics. *Electronics-Switz* **2012,** *1* (1), 23-31.

240. Schwank, J. R.; Shaneyfelt, M. R.; Dasgupta, A.; Francis, S. A.; Zhou, X. J.; Fleetwood, D. M.; Schrimpf, R. D.; Pantelides, S. T.; Felix, J. A.; Dodd, P. E.; Ferlet-Cavrois, V.; Paillet, P.; Dalton, S. M.; Swanson, S. E.; Hash, G. L.; Thornberg, S. M.; Hochrein, J. M.; Lum, G. K., Effects of Moisture and Hydrogen Exposure on Radiation-Induced MOS Device Degradation and Its Implications for Long-Term Aging. *Ieee Transactions on Nuclear Science* **2008,** *55* (6), 3206-3215.

241. Fleetwood, D. M., Effects of hydrogen transport and reactions on microelectronics radiation response and reliability. *Microelectron Reliab* **2002,** *42* (4-5), 523-541.

242. Zhang, C. X.; Zhang, E. X.; Fleetwood, D. M.; Alles, M. L.; Schrimpf, R. D.; Song, E. B.; Kim, S. M.; Galatsis, K.; Wang, K. L. W., Electrical Stress and Total Ionizing Dose Effects on Graphene-Based Non-Volatile Memory Devices. *IEEE Transactions on Nuclear Science* **2012,** *59* (6), 2974-2978.

243. Fleetwood, D. M.; Xiong, H. D.; Lu, Z. Y.; Nicklaw, C. J.; Felix, J. A.; Schrimpf, R. D.; Pantelides, S. T., Unified model of hole trapping, 1/f noise, and thermally stimulated current in MOS devices. *Ieee Transactions on Nuclear Science* **2002,** *49* (6), 2674-2683.

244. Wang, P.; Perini, C.; O'Hara, A.; Tuttle, B. R.; Zhang, E. X.; Gong, H.; Dong, L.; Liang, C.; Jiang, R.; Liao, W.; Fleetwood, D. M.; Schrimpf, R. D.; Vogel, E. M.; Pantelides, S. T., Radiation-Induced Charge Trapping and Low-Frequency Noise of Graphene Transistors. *Ieee Transactions on Nuclear Science* **2018,** *65* (1), 156-163.

245. Digne, M.; Sautet, P.; Raybaud, P.; Euzen, P.; Toulhoat, H., Hydroxyl groups on gamma-alumina surfaces: A DFT study. *J Catal* **2002,** *211* (1), 1-5.

246. Cho, S. B.; Lee, S.; Chung, Y. C., Water Trapping at the Graphene/Al2O3 Interface. *Japanese Journal of Applied Physics* **2013,** *52* (6).

247. Foran, B.; Mann, C.; Peterson, M.; Bushmaker, A.; Wang, B.; Chen, J.; Yang, S.; Cronin, S. B., Effects of Proton Radiation-Induced Defects on Optoelectronic Properties of MoS2. IEEE Transactions on Nuclear Science

2018.

248. Kresse, G.; Furthmuller, J., Efficient iterative schemes for ab initio total-energy calculations using a plane-wave basis set. *Phys. Rev. B* **1996,** *54* (16), 11169-11186.

249. Shen, X.; Puzyrev, Y. S.; Fleetwood, D. M.; Schrimpf, R. D.; Pantelides, S. T., Quantum Mechanical Modeling of Radiation-Induced Defect Dynamics in Electronic Devices. *Ieee Transactions on Nuclear Science* **2015,** *62* (5), 2169-2180.

250. Perdew, J. P.; Burke, K.; Ernzerhof, M., Generalized gradient approximation made simple. *Phys. Rev. Lett.* **1996,** *77* (18), 3865-3868.

251. Grimme, S.; Antony, J.; Ehrlich, S.; Krieg, H., A consistent and accurate ab initio parametrization of density functional dispersion correction (DFT-D) for the 94 elements H-Pu. *J Chem Phys* **2010,** *132* (15).

252. Blochl, P. E., Projector Augmented-Wave Method. *Phys. Rev. B* **1994,** *50* (24), 17953-17979.

253. Fonseca, L. R. C.; Liu, D.; Robertson, J., p-type Fermi level pinning at a Si : Al(2)O(3) model interface. *Applied Physics Letters* **2008,** *93* (12).

254. Liu, D.; Clark, S. J.; Robertson, J., Oxygen vacancy levels and electron transport in Al2O3. *Applied Physics Letters* **2010,** *96* (3).

255. Sohlberg, K.; Pennycook, S. J.; Pantelides, S. T., Hydrogen and the structure of the transition aluminas. *J. Am. Chem. Soc.* **1999,** *121* (33), 7493-7499.

256. Jennison, D. R.; Schultz, P. A.; Sullivan, J. P., Evidence for interstitial hydrogen as the dominant electronic defect in nanometer alumina films. *Phys. Rev. B* **2004,** *69* (4).

257. Choudhary, N.; Park, J.; Hwang, J. Y.; Chung, H.-S.; Dumas, K. H.; Khondaker, S. I.; Choi, W.; Jung, Y., Centimeter Scale Patterned Growth of Vertically Stacked Few Layer Only 2D MoS2/WS2 van der Waals Heterostructure. *Scientific Reports* **2016,** *6*, srep25456.

258. Zhao, W. J.; Ghorannevis, Z.; Amara, K. K.; Pang, J. R.; Toh, M.; Zhang, X.; Kloc, C.; Tan, P. H.; Eda, G., Lattice dynamics in mono- and few-layer sheets of WS2 and WSe2. *Nanoscale* **2013,** *5* (20), 9677-9683.

259. Ye, M.; Winslow, D.; Zhang, D.; Pandey, R.; Yap, Y. K., Recent Advancement on the Optical Properties of Two-Dimensional Molybdenum Disulfide (MoS2) Thin Films. *Photonics* **2015,** *2* (1), 288-307.

260. Fan, X. P.; Zheng, W. H.; Liu, H. J.; Zhuang, X. J.; Fan, P.; Gong, Y. F.; Li, H. L.; Wu, X. P.; Jiang, Y.; Zhu, X. L.; Zhang, Q. L.; Zhou, H.; Hu, W.; Wang, X.; Duan, X. F.; Pan, A. L., Nonlinear photoluminescence in monolayer WS2: parabolic emission and excitation fluence-dependent recombination dynamics. *Nanoscale* **2017,** *9* (21), 7235-7241.

261. Elías, A. L.; Perea-López, N.; Castro-Beltrán, A.; Berkdemir, A.; Lv, R.; Feng, S.; Long, A. D.; Hayashi, T.; Kim, Y. A.; Endo, M.; Gutiérrez, H. R.; Pradhan, N. R.; Balicas, L.; Mallouk, T. E.; López-Urías, F.; Terrones, H.; Terrones, M., Controlled Synthesis and Transfer of Large-Area WS2 Sheets: From Single Layer to Few Layers. *ACS Nano* **2013,** *7* (6), 5235-5242.

262. Carozo, V.; Wang, Y.; Fujisawa, K.; Carvalho, B. R.; McCreary, A.; Feng, S.; Lin, Z.; Zhou, C.; Perea-López, N.; Elías, A. L.; Kabius, B.; Crespi, V. H.; Terrones, M., Optical identification of sulfur vacancies: Bound excitons at the edges of monolayer tungsten disulfide. *Science Advances* **2017,** *3* (4), e1602813.

263. Yuan, J. T.; Najmaei, S.; Zhang, Z. H.; Zhang, J.; Lei, S. D.; Ajayan, P. M.; Yakobson, B. I.; Lou, J., Photoluminescence Quenching and Charge Transfer in Artificial Heterostacks of Monolayer Transition Metal Dichalcogenides and Few-Layer Black Phosphorus. *ACS Nano* **2015,** *9* (1), 555-563.

264. Hong, X. P.; Kim, J.; Shi, S. F.; Zhang, Y.; Jin, C. H.; Sun, Y. H.; Tongay, S.; Wu, J. Q.; Zhang, Y. F.; Wang, F., Ultrafast charge transfer in atomically thin MoS2/WS2 heterostructures. *Nature Nanotechnology* **2014,** *9* (9), 682-686.

265. Son, Y.; Wang, Q. H.; Paulson, J. A.; Shih, C. J.; Rajan, A. G.; Tvrdy, K.; Kim, S.; Alfeeli, B.; Braatz, R. D.; Strano, M. S., Layer Number Dependence of MoS2 Photoconductivity Using Photocurrent Spectral Atomic Force Microscopic Imaging. *ACS Nano* **2015,** *9* (3), 2843-2855.

266. Park, J.; Lee, W.; Choi, T.; Hwang, S. H.; Myoung, J. M.; Jung, J. H.; Kim, S. H.; Kim, H., Layer-modulated synthesis of uniform tungsten disulfide nanosheet using gas-phase precursors. *Nanoscale* **2015,** *7* (4), 1308-1313.

267. Bogaert, K.; Liu, S.; Liu, T.; Guo, N.; Zhang, C.; Gradecak, S.; Garaj, S., Two-Dimensional MoxW1-xS2 Graded Alloys: Growth and Optical Properties. *Scientific Reports* **2018,** *8*.

268. Baker, M. A.; Gilmore, R.; Lenardi, C.; Gissler, W., XPS investigation of preferential sputtering of S from MoS2 and determination of MoSx stoichiometry from Mo and S peak positions. *Appl Surf Sci* **1999,** *150* (1-4), 255-262.

269. Salehi, S.; Saffarzadeh, A., Atomic defect states in monolayers of MoS2 and WS2. *Surf Sci* **2016,** *651*, 215-221.

270. Liu, Y.; Guo, J.; Zhu, E.; Liao, L.; Lee, S.-J.; Ding, M.; Shakir, I.; Gambin, V.; Huang, Y.; Duan, X., Approaching the Schottky–Mott limit in van der Waals metal–semiconductor junctions. *Nature* **2018**, 1.

271. NIST, NIST X-ray Photoelectron Spectroscopy Database, NIST Standard Reference Database Number 20. National Institute of Standards and Technology: Gaithersburg MD, 20899, 2000.

272. Liu, X.; Balla, I.; Bergeron, H.; Hersam, M. C., Point Defects and Grain Boundaries in Rotationally Commensurate MoS2 on Epitaxial Graphene. *J. Phys. Chem. C* **2016,** *120* (37), 20798-20805.

273. Ly, T. H.; Perello, D. J.; Zhao, J.; Deng, Q. M.; Kim, H.; Han, G. H.; Chae, S. H.; Jeong, H. Y.; Lee, Y. H., Misorientation-angle-dependent electrical transport across molybdenum disulfide grain boundaries. *Nature Communications* **2016,** *7*, 10426.

274. Lee, G.-H.; Yu, Y.-J.; Lee, C.; Dean, C.; Shepard, K. L.; Kim, P.; Hone, J., Electron tunneling through atomically flat and ultrathin hexagonal boron nitride. *Applied Physics Letters* **2011,** *99* (24), 243114.

275. Ahmed, F.; Choi, M. S.; Liu, X.; Yoo, W. J., Carrier transport at the metal-MoS2 interface. *Nanoscale* **2015,** *7* (20), 9222-9228.

276. Li, F.; Lu, Z. X.; Lan, Y. W.; Jiao, L. Y.; Xu, M. X.; Zhu, X. Y.; Zhang, X. K.; Wu, H. L.; Qi, J. J., Force and light tuning vertical tunneling current in the atomic layered MoS2. *Nanotechnology* **2018,** *29* (27), 275202.

277. Beebe, J. M.; Kim, B.; Gadzuk, J. W.; Frisbie, C. D.; Kushmerick, J. G., Transition from direct tunneling to field emission in metal-molecule-metal junctions. *Phys. Rev. Lett.* **2006,** *97* (2), 026801.

278. English, C. D.; Shine, G.; Dorgan, V. E.; Saraswat, K. C.; Pop, E., Improved Contacts to MoS2 Transistors by Ultra-High Vacuum Metal Deposition. *Nano Lett.* **2016,** *16* (6), 3824-3830.

279. Chan, J.; Martinez, N. Y.; Fitzgerald, J. J. D.; Walker, A. V.; Chapman, R. A.; Riley, D.; Jain, A.; Hinkle, C. L.; Vogel, E. M., Extraction of correct Schottky barrier height of sulfur implanted NiSi/n-Si junctions: Junction doping rather than barrier height lowering. *Applied Physics Letters* **2011,** *99* (1), 012114.

280. Yoon, M.; Min, S. W.; Dugasani, S. R.; Lee, Y. U.; Oh, M. S.; Anthopoulos, T. D.; Park, S. H.; Im, S., Charge Transport in 2D DNA Tunnel Junction Diodes. *Small* **2017,** *13* (48), 1703006.

281. Lee, S. H.; Choi, M. S.; Lee, J.; Ra, C. H.; Liu, X.; Hwang, E.; Choi, J. H.; Zhong, J.; Chen, W.; Yoo, W. J., High performance vertical tunneling diodes using graphene/hexagonal boron nitride/graphene hetero-structure. *Applied Physics Letters* **2014,** *104* (5), 053103.

282. Koszewski, A.; Souchon, F.; Dieppedale, C.; Bloch, D.; Ouisse, T., Physical model of dielectric charging in MEMS. *J Micromech Microeng* **2013,** *23* (4), 045019.

283. Robinson, J. A.; LaBella, M.; Zhu, M.; Hollander, M.; Kasarda, R.; Hughes, Z.; Trumbull, K.; Cavalero, R.; Snyder, D., Contacting graphene. *Applied Physics Letters* **2011,** *98* (5), 053103.

284. Bourg, M.-C.; Badia, A.; Lennox, R. B., Gold−Sulfur Bonding in 2D and 3D Self-Assembled Monolayers: XPS Characterization. *J. Phys. Chem. B* **2000,** *104* (28), 6562-6567.

285. Vitale, F.; Vitaliano, R.; Battocchio, C.; Fratoddi, I.; Piscopiello, E.; Tapfer, L.; Russo, M. V., Synthesis and characterization of gold nanoparticles stabilized by palladium(II) phosphine thiol. *J Organomet Chem* **2008,** *693* (6), 1043-1048.

286. Gronbeck, H.; Curioni, A.; Andreoni, W., Thiols and disulfides on the Au(111) surface: The headgroup-gold interaction. *J. Am. Chem. Soc.* **2000,** *122* (16), 3839-3842.

287. Dubois, L. H.; Nuzzo, R. G., Synthesis, Structure, and Properties of Model Organic-Surfaces. *Annu Rev Phys Chem* **1992,** *43*, 437-463.

288. Tao, Y. T.; Wu, C. C.; Eu, J. Y.; Lin, W. L.; Wu, K. C.; Chen, C. H., Structure evolution of aromatic-derivatized thiol monolayers on evaporated gold. *Langmuir* **1997,** *13* (15), 4018-4023.

289. Franz, A. W.; Stoycheva, S.; Himmelhaus, M.; Muller, T. J. J., Synthesis, electronic properties and self-assembly on Au{111} of thiolated (oligo)phenothiazines. *Beilstein J Org Chem* **2010,** *6*.

290. Petrovykh, D. Y.; Kimura-Suda, H.; Opdahl, A.; Richter, L. J.; Tarlov, M. J.; Whitman, L. J., Alkanethiols on platinum: Multicomponent self-assembled monolayers. *Langmuir* **2006,** *22* (6), 2578-2587.

291. Zhu, Y.; Zhou, R.; Zhang, F.; Appenzeller, J., Vertical charge transport through transition metal dichalcogenides – a quantitative analysis. *Nanoscale* **2017,** *9* (48), 19108-19113.